# Search for dark matter in events containing jets and missing transverse momentum using ratio measurements

Valentinos Christodoulou
University College London

December 7, 2017

# Declaration

I, Valentinos Christodoulou confirm that the work presented in this thesis is my own. Where information has been derived from other sources, I confirm that this has been indicated in the thesis.

Valentinos Christodoulou

# Abstract

This thesis presents a measurement of missing transverse momentum in association with jets at $\sqrt{s} = 13$ TeV with 3.2 fb$^{-1}$ of proton-proton collisions at the LHC, collected in 2015 using the ATLAS detector. In the Standard Model of particle physics, this is the experimental signature of $Z$ boson production in association with jets, where the $Z$ boson decays to neutrinos, however it could also be the signature of dark matter production in association with jets. A ratio can be formed using events containing oppositely charged same-flavour lepton pairs in association with jets, consistent with the decay of a $Z/\gamma^*$ boson. Detector inefficiencies can be accounted for by defining a correction factor and applying it to the ratio in order to recover the lost events. The detector-corrected ratio is measured differentially with respect to four variables in two jet phase spaces. The measured ratios are consistent with the Standard Model prediction and the data are used to place limits on the production of dark matter in proton-proton collisions at the LHC on three models, an effective field theory model, a simplified model with an axial-vector mediator, and the production of an invisibly decaying Higgs boson.

In addition, the ATLAS trigger system has been upgraded for the 2015 data taking and a new jet reconstruction algorithm has been developed for the updated jet trigger software. Diagnostic algorithms have been developed to test the new software and its validation has been automated using a new jet trigger validation package. The new jet triggers perform as expected and their performance has been evaluated using the full 2015 dataset.

# Acknowledgements

I would like to start by thanking my supervisors, Andy Pilkington and Emily Nurse, for their guidance and support throughout my PhD. I'm grateful to Andy for choosing technical projects with software development components, which I enjoyed very much. I would also like to thank Christian Gütschow for showing me how the ATLAS software works and answering all of my questions, especially the ones about the simulation. I have greatly benefited from Peter Sherwood who taught me how the jet trigger menu works and encouraged me to use advanced C++ features in my software packages. Finally, I would like to thank my family, especially my parents, for their support during my studies.

# Preface

The work presented in this thesis was performed as part of the ATLAS Collaboration with the contributions of the author detailed as follows.

The technical work performed in Chapter 4 within the jet trigger group was part of the ATLAS authorship qualification task. The author was responsible for the development of a new jet trigger reconstruction software package for LHC Run-2. Diagnostic algorithms and a new validation package used to automate the validation of the new jet trigger software were also developed by the author. In addition, the author calculated the efficiencies for all standard jet triggers in the menu using the full 2015 data, and also efficiencies using combinations of central and forward single-jet triggers for the di-jet $\eta$-intercalibration group.

The dark matter search using ratio measurements presented in Chapter 5 was performed in an analysis team with contributions from several institutes across the world. The author was responsible for the numerator of the ratio (measurement of the events containing missing transverse momentum produced in association with jets), including event selection, electron and tau efficiencies, background estimation and systematic uncertainties, with the exception of the small multi-jet background and the theory scale variation systematics. The software framework used for the full analysis chain was also developed by the author. In addition, the author has contributed to the official derivation framework used by dark matter analyses at ATLAS.

# Contents

# List of figures

# List of tables

# Chapter 1.

# Introduction

The nature of dark matter (DM) is one of the biggest mysteries in modern physics. DM was first observed in the 1930s using clusters of galaxies [1, 2], more specifically the rotational velocity of stars and gas as a function of their distance from the galactic centre. The observed rotational velocity did not decrease by $\sqrt{1/r}$ as expected when moving away from the centre of the galaxy, indicating the existence of some other type of non-luminous matter. The results from the Planck experiment [3] indicate that the total mass-energy of the universe contains 4.9% ordinary matter, 26.8% dark matter and 68.3% dark energy. The only known interaction of DM is with gravity, which is how it has been observed and studied so far using astrophysical experiments [4]. The existence of DM means the Standard Model of particle physics is incomplete and will have to be extended if DM interacts with ordinary matter.

The baseline of searching for DM in particle physics experiments is the assumption that DM interacts with ordinary matter via a weakly interacting force. DM particles could be a type of weakly interacting massive particles (WIMPs). There are three classes of DM searches, direct detection, indirect detection and collider searches. Direct detection experiments search for low-energy recoils of matter particles in the detector that occur due to interactions with DM particles passing through the detector. These types of experiments are typically located deep underground to reduce backgrounds from cosmic rays. One example is the Large Underground Xenon (LUX) experiment [5] utilizing a 370 kg liquid xenon time projection chamber located 1500 m underground. Indirect detection experiments are looking for products of the annihilation of DM in space, typically outside the solar system. These types of experiments are typically located at the South Pole or in space, such as the Alpha Magnetic Spectrometer (AMS) [6] on the International Space Station. Finally, collider experiments are looking for the production of DM in high energy particle collisions. Collisions between ordinary particles could produce DM via direct pair-production or decays involving new particles that decay to DM, as long as sufficient energy is available. The Large Hadron Collider (LHC) [7], the world's largest and most powerful particle accelerator,

is currently colliding protons at a centre of mass energy of $\sqrt{s} = 13$ TeV. Any DM particles produced at the LHC will be very challenging to detect since they do not deposit any energy or leave tracks in the detectors.

The purpose of this thesis is to present an ATLAS measurement that introduced a new observable to search for DM at the LHC. The thesis begins with an overview of the theoretical framework of particle physics, the evidence and possible models for DM, and the physics of hadron-hadron collisions. A brief description of the ATLAS detector [8] and object reconstruction is then given in Chapter 3. Chapter 4 presents updates to the ATLAS jet trigger system for Run-2, as well as the validation and performance evaluation of the new trigger system. Chapter 5 describes the measurement of observables sensitive to dark matter in events with jets and missing transverse momentum. Finally, Chapter 6 summarises the results and conclusions from the work outlined in this thesis.

# Chapter 2.

# Theoretical Framework

## 2.1. The Standard Model of particle physics

The Standard Model (SM) of particle physics describes the fundamental particles and their interactions, via the strong, weak and electromagnetic (EM) forces. In this model, all matter is made up of two types of particles, fermions and bosons. Fermions are the fundamental building blocks of matter and are governed by Fermi-Dirac statistics, have half-integer spin, and obey the Pauli exclusion principle. Bosons are the mediators of the forces that control the interactions, follow Bose-Einstein statistics, and have integer spin. The particles of the SM and their properties are summarized in Figure 2.1.

Fermions are divided into two groups, quarks and leptons, each further divided into three generations. The first generation makes up common matter, while going up to the second and third generations the fermion mass increases, leaving other quantum properties unchanged. There are six quarks and six leptons, each having an antiparticle with identical mass but opposite electric charge. The leptons are split into two additional categories, charged leptons and neutrinos, with the charged leptons carrying a unit electric charge and neutrinos being electrically neutral. Neutrinos are assumed to be massless in the SM and interact only via the weak interaction. Charged leptons have non-zero mass and interact via the EM and weak interactions. Quarks have fractional electric charge and interact via the strong interaction as well as the weak and EM interactions. The heaviest particle in the SM is the top quark with a mass of $173.1 \pm 0.6$ GeV [9].

Bosons are divided into groups depending on the force they mediate. The photon is the mediator of the EM interaction, couples to electrically charged particles, is massless, electrically neutral, and has a unit spin. The gluon is the mediator of the strong force, couples to quarks, is massless, has unit spin, and comes in eight variations. The $W^{\pm}$ and $Z$ bosons are the mediators of the weak interaction with unit spin and couple to all fermions. The $W^{\pm}$ bosons carry a unit electric charge and have a mass of $80.385 \pm 0.015$ GeV [9].
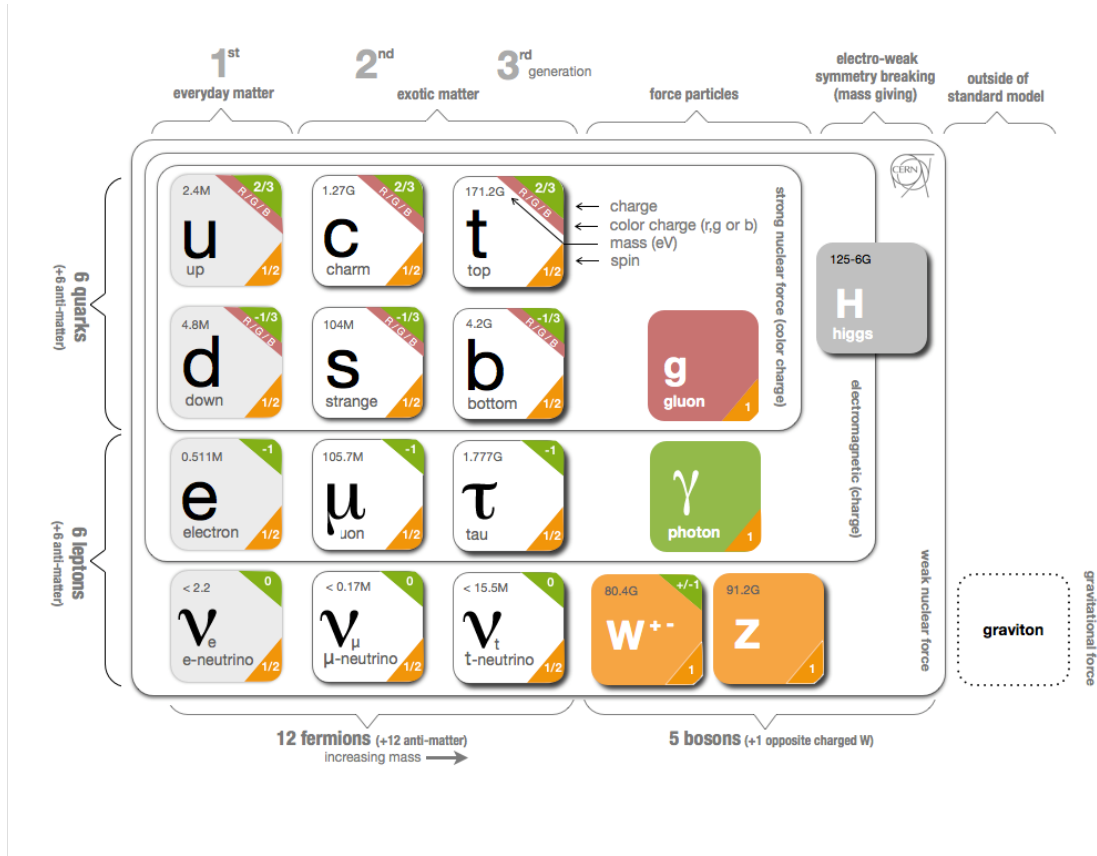
**Figure 2.1.** Overview of the Standard Model and the properties of each particle [10].

The $Z$ boson is electrically neutral with a mass of $91.1876 \pm 0.0021$ GeV [9]. The final boson in the SM is the recently discovered Higgs boson [11, 12], which is electrically neutral, has a mass of $125.09 \pm 0.24$ GeV [9], and is a scalar particle.

The SM interactions are defined by the $\mathrm{SU}(3)_\mathrm{c} \times \mathrm{SU}(2)_\mathrm{L} \times \mathrm{U}(1)_\mathrm{Y}$ gauge symmetry group. The $\mathrm{SU}(3)_\mathrm{c}$ symmetry group corresponds to the strong interaction with eight generators which are the eight gluons. Strong interactions are described by quantum chromodynamics (QCD) [13] in which the colour charge, carried by quarks and gluons, is analogous to the electric charge in quantum electrodynamics (QED). QCD is a non-Abelian gauge theory describing the interactions between quarks and gluons. At high energies the strong coupling constant, $\alpha_\mathrm{s}$, is small, making perturbation theory a good approximation (asymptotic freedom), and large at low energies, confining quarks in colour neutral composite objects (confinement).

The $\mathrm{SU}(2)_\mathrm{L} \times \mathrm{U}(1)_\mathrm{Y}$ symmetry group corresponds to the electroweak interaction [14–16], with the resulting combinations of the four generators representing the $W^\pm$ and $Z$ bosons as well as the photon. Left-handed fermions exist as doublets under $\mathrm{SU}(2)_\mathrm{L}$, while the

right-handed fermions are singlets. The quark weak eigenstates are different from the mass eigenstates and are related via the Cabbibo-Kobayashi-Maskawa (CKM) matrix [17, 18]. Neutrinos are left-handed, while anti-neutrinos are right-handed.

Local gauge symmetries require the generators to be massless but the $W^{\pm}$ and $Z$ bosons are massive. The electroweak symmetry is spontaneously broken through the Brout-Englert-Higgs mechanism [19–24] in which the scalar Higgs field manifests itself as the Higgs boson, giving mass to the weak bosons and the charged fermions.

An interesting SM process related to the work presented in this thesis is the branching ratio of the $Z$ boson to lepton pairs. Unlike the branching ratio of the $W^{\pm}$ boson to a pair of charged leptons and neutrinos, with equal probability of 1/9 for each lepton flavour, the branching ratio of the $Z$ boson to the sum of all neutrino final states is $(20.00 \pm 0.06)\%$, compared to only $(3.3658 \pm 0.0023)\%$ for each charged lepton flavour [9]. The branching ratio depends on the vector and axial-vector couplings of the $Z$ boson which are $c_V = I_3 - Q sin^2 \theta_W$ and $c_A = I_3$, respectively, where $I_3$ is the third component of the weak isospin of the fermion, $Q$ is the electric charge of the fermion, and $\theta_W$ is the weak mixing angle. The couplings are different for neutrinos and charged leptons due to the weak isospin being different for left-handed and right-handed fermions and also the fact that neutrinos are electrically neutral, while charged leptons carry a unit electric charge.

The SM is a very successful predictive model but also has some limitations [25]. The observation of neutrino oscillations [26–28] means that neutrinos have flavour and mass eigenstates, implying that they must have some finite mass. The matter-antimatter asymmetry in the universe is not explained by the SM alone. The CKM matrix provides terms for charge parity (CP) violation [29, 30] that can account for some of the asymmetry, but cannot account for all of it. It is not known why there is no CP violation in strong interactions. The discovery of the Higgs boson has completed the SM, but it is unknown why its mass is at the level of 125 GeV, many orders of magnitudes smaller than the Planck scale. Furthermore, the SM does not provide a quantum description of gravity, does not provide a candidate for the dark matter in the universe, and does not explain the nature of dark energy.

## 2.2. Dark matter

### 2.2.1. Evidence for dark matter

Evidence for the existence of DM comes from many independent astrophysical observations. The oldest observation of DM comes velocity dispersion measurements of galaxies in

the Coma cluster which required about 400 times more mass than what was visually observable [1]. In addition, galaxy rotation curves, the rotational velocity of stars and gas as a function of their distance from the galactic centre, provided compelling evidence for DM. The observed rotational velocity did not decrease by $\sqrt{1/r}$ as expected when moving away from the centre of the galaxy, indicating the existence of some other type of non-luminous matter.

Gravitational lensing experiments [31] have also made observations which cannot be accounted for by the visible matter alone. Gravitational lensing is the bending of light travelling between a distant light source and an observer due to a large mass along its path. This can lead to multiple images, or distortions that can be used to constrain the mass of the lensing structure. A notable example is the Bullet Cluster, one of the most energetic clusters of galaxies in the universe, containing two galaxies in the process of colliding. Detailed studies using gravitational lensing suggest the presence of additional non-interacting invisible matter.

The Cosmic Microwave Background (CMB) provides compelling evidence for the existence of DM. The CMB is the thermal radiation left over from the time of recombination, approximately $380\,000$ years after the Big Bang, with a current temperature of approximately 2.7 K. The CMB is very close to a perfect black body, but contains anisotropies that can be decomposed into a power spectrum, whose peaks constrain cosmological parameters such as the density of baryonic matter and the density of DM in the universe. The anisotropies in the CMB are caused by baryonic acoustic oscillations (BAO), regular, periodic fluctuations in the density of the baryonic matter. The early universe consisted of a hot, dense plasma of DM, baryons, and photons. Overdense regions gravitationally attracted matter towards them, while the heat from baryon-photon interactions created an outward pressure, resulting in oscillations. DM only interacts gravitationally and stayed at the centre while photons and baryons moved outwards together until they decoupled, allowing the photons to stream away. This led to cooler regions where photons streamed away and hotter regions where matter contracted, resulting in anisotropies in the CMB.

Big Bang Nucleosynthesis (BBN) is the production of light elements, heaver than hydrogen, roughly 10 seconds to 20 minutes after the Big Bang. Protons and neutrons fused to produce deuterium, an isotope of hydrogen. Helium and a small amount of tritium, another isotope of hydrogen, were then produced by the fusion of deuterium with protons and other deuterium nuclei. The process continued until the production of lithium-7. BBN models assume that most of the universe is composed of baryonic matter, however, the calculated concentration of deuterium in the universe is too high to be consistent with these models, since it should have turned into helium-4. Only BBN models that include DM and a smaller baryon density predict the right amount of deuterium concentration.

The most popular model for the universe is the $\Lambda$CDM model, also known as the standard model of cosmology, a theory in which the universe contains a non-zero cosmological constant, $\Lambda$, and considers DM to be a cold (non-relativistic and heavy) particle. DM could also be hot (ultra-relativistic, and extremely light) or warm (somewhere between cold and hot). Computer simulations are used to simulate the structure formation in the early universe assuming either cold, hot or warm DM. Only cold DM produces a universe similar to what is observed today, while the high velocity of warmer DM does not allow substructure formation. The $\Lambda$CDM model provides a reasonable account of the large-scale structure in the distribution of galaxies, the CMB, the abundances of the light elements produced in BBN, and the accelerating expansion of the universe.

### 2.2.2. Models for dark matter interactions with the Standard Model particles

The particle physics nature of DM is unknown and a variety of different approaches are typically considered for modelling DM interactions with the SM. There are two conflicting requirements, generality and plausibility. Generality requires making as few assumptions as possible on new DM particles. Plausibility requires models to be in agreement with principles of the SM, such as lepton and baryon number conservation, or to have perturbative ultraviolet (UV) completion. The two approaches can also be characterised as bottom-up, adding the minimum amount of new particles to the SM, such as Effective Field Theory (EFT), or top-down, starting from fully developed UV-complete theories and examining candidates for DM candidates, such as supersymmetry (SUSY).

Three models with DM couplings to different SM particles are discussed in this Section. EFT models with DM coulings to weak bosons, simplified models with DM couplings to quarks, and the Higgs portal as a way of DM coupling to the Higgs boson.

**Effective Field Theory models**

EFT approaches make the most minimal assumptions possible, that the DM particle is the only new particle beyond the SM (BSM) kinematically accessible at the LHC. EFTs describe the interactions between DM and SM using contact operators of mass dimension larger than four. Each operator is characterized by two parameters, the EFT scale, $\Lambda$, and the mass of the DM particle. The shape of all kinematic distributions is independent of the EFT scale. EFTs are very appealing since they are model-independent, but they are sometimes disfavoured for LHC searches because they violate perturbative unitarity and make unphysical predictions at large momentum transfers [32].

An example EFT model assumes that DM interacts only with weak bosons, and vector boson fusion (VBF) topologies are the optimal way to probe such interactions at the LHC [33, 34]. The DM particle, $\chi$, is a Dirac or Majorana fermion, and the operators are of dimension d $\leq$ 7, coupling to the SM vector bosons ($V = Z$, $W^{\pm}$, $\gamma$) with either three ($V\chi\chi$) or four ($VV\chi\chi$) point couplings. The dimension-five operators, D5a-b, could result from exchanges mediated by new heavy scalar or pseudoscalar bosons. The dimension-six operators, D6a-b, could arise via the exchange of new neutral vector bosons. The dimension-seven operators, D7a-d, typically arise from one-loop diagrams, such as the $\chi_1^0 \chi_1^0 \rightarrow \gamma\gamma$ process in SUSY [35]. Table 2.1 shows the ten operators in this model with their contact interaction Lagrangians and EFT scale.

| Name | Operator | Dimension | EFT scale [GeV] |
|------|----------|-----------|-----------------|
| D5a | $\mathcal{L} = \frac{1}{\Lambda}\bar{\chi}\chi\left[\frac{Z_\mu Z^\mu}{2} + W_\mu^+ W^{-\mu}\right]$ | 5 | 100 |
| D5b | $\mathcal{L} = \frac{1}{\Lambda}\bar{\chi}\gamma^5\chi\left[\frac{Z_\mu Z^\mu}{2} + W_\mu^+ W^{-\mu}\right]$ | 5 | 100 |
| D5c | $\mathcal{L} = \frac{g}{2\cos\theta_W \Lambda}\bar{\chi}\sigma^{\mu\nu}\chi\left[\delta_\mu Z_\nu - \delta_\nu Z_\mu\right]$ | 5 | 3300 |
| D5d | $\mathcal{L} = \frac{g}{2\cos\theta_W \Lambda}\bar{\chi}\sigma^{\mu\nu}\chi\epsilon^{\mu\nu\sigma\rho}\left[\delta_\rho Z_\sigma - \delta_\sigma Z_\rho\right]$ | 5 | 6600 |
| D6a | $\mathcal{L} = \frac{g}{2\cos\theta_W \Lambda^2}\bar{\chi}\gamma^\mu\delta^\nu\chi\left[\delta_\mu Z_\nu - \delta_\nu Z_\mu\right]$ | 6 | 230 |
| D6b | $\mathcal{L} = \frac{g}{2\cos\theta_W \Lambda^2}\bar{\chi}\gamma_\mu\delta_\nu\chi\epsilon^{\mu\nu\sigma\rho}\left[\delta_\rho Z_\sigma - \delta_\sigma Z_\rho\right]$ | 6 | 330 |
| D7a | $\mathcal{L} = \frac{1}{\Lambda^3}\bar{\chi}\chi W^{i,\mu\nu}W_{\mu\nu}^i$ | 7 | 100 |
| D7b | $\mathcal{L} = \frac{1}{\Lambda^3}\bar{\chi}\gamma^5\chi W^{i,\mu\nu}W_{\mu\nu}^i$ | 7 | 100 |
| D7c | $\mathcal{L} = \frac{1}{\Lambda^3}\bar{\chi}\chi\epsilon^{\mu\nu\sigma\rho}W^{i,\mu\nu}W_{\rho\sigma}^i$ | 7 | 100 |
| D7d | $\mathcal{L} = \frac{1}{\Lambda^3}\bar{\chi}\gamma^5\chi\epsilon^{\mu\nu\sigma\rho}W^{i,\mu\nu}W_{\rho\sigma}^i$ | 7 | 100 |

**Table 2.1.** Effective operators for a DM fermion interacting only with weak bosons, where $\chi$ and $\bar{\chi}$ are Dirac or Majorana fermionic DM particles, $Z$ and $W$ are SM boson operators, and $\Lambda$ is the EFT scale [33, 34].

## Simplified models

Another approach is to use simplified models [36] in which the mediator of the interactions between the SM and DM can be produced at the LHC and has dimension four or less. Simplified models should satisfy the following three requirements to be useful at the LHC. First, the model should contain a stable DM candidate and a mediator to couple the SM with

the dark sector. Second, the Lagrangian should contain all terms that are renormalisable and consistent with Lorentz invariance, the SM gauge symmetries, and DM stability. Third, the interactions between SM particles and DM should not violate the global symmetries of the SM, such as conservation of lepton and baryon number. Simplified models are not model-independent like the EFTs, but they can correctly describe the kinematics of DM production at the LHC using the mediators they contain. They can be used to approximate a large group of models in parameter space, all of which have approximately similar kinematics.

The most popular simplified models for LHC are the s-channel models, which couple the DM, $\chi$, to quarks, $q$. These models are split into two categories depending on the spin of the mediator, spin-1 models and spin-0 models, with vector or axial-vector mediators, and scalar or pseudoscalar mediators respectively. Spin-1 mediators are assumed to couple to all quarks with equal strength, whereas spin-0 mediators are expected to couple most strongly to top quarks. An axial-vector mediator, $V^\mu$, with couplings to quarks, $g_q$, and DM, $g_\chi$, is described by

$$\mathcal{L}_{\text{axial}-\text{vector}} \supset g_q V^\mu \sum_q \bar{q}\gamma_\mu\gamma^5 q + g_\chi V^\mu \bar{\chi}\gamma_\mu\gamma^5\chi \tag{2.1}$$

Similary, a vector mediator, $V^\mu$, is described by

$$\mathcal{L}_{\text{vector}} \supset g_q V^\mu \sum_q \bar{q}\gamma_\mu q + g_\chi V^\mu \bar{\chi}\gamma_\mu\chi \tag{2.2}$$

A scalar mediator, $\phi$, is described by

$$\mathcal{L}_{\text{scalar}} \supset g_q \phi \sum_q \frac{y_q}{\sqrt{2}}\bar{q}q + g_\chi\phi\bar{\chi}\chi \tag{2.3}$$

where $y_q$ is the Yukawa coupling. Similary, a pseudoscalar mediator, $a$, is described by

$$\mathcal{L}_{\text{pseudoscalar}} \supset g_q a \sum_q \frac{y_q}{\sqrt{2}}\bar{q}\gamma^5 q + g_\chi a\bar{\chi}\gamma^5\chi \tag{2.4}$$

It is also possible to have couplings to both quarks and leptons, but those models are slightly more complicated. The ATLAS-CMS Dark Matter Forum [37,38] recommendations set the couplings to $g_q = 0.25$ and $g_\chi = 1$ for spin-1 mediators and $g_q = g_\chi = 1$ for spin-0 mediators.

**Higgs portal**

DM could predominantly couple to SM particles through the SM Higgs boson, referred to as the Higgs portal [39, 40]. There are two popular classes of these kind of models. The first model class assumes the DM particle is a scalar singlet under the SM gauge group, which couples through a quartic interaction with the Higgs boson [41–47]. This scalar Higgs portal model can be described by

$$\mathcal{L}_{\text{scalar}} \supset -\lambda_\chi \chi^4 - \lambda_p \chi^2 |H|^2 \tag{2.5}$$

where $\chi$ is an additional real scalar singlet (the DM candidate), $\lambda_\chi$ is the self-coupling of the scalar $\chi$, $H$ is the SM Higgs doublet, and $\lambda_p$ is the portal coupling. When the mass of the DM particle is less than half the mass of the Higgs boson the interactions contribute to the invisible decay of the Higgs. Otherwise the Higgs boson cannot decay on-shell to a pair of DM particles so the production has to be off-shell, suppressing the production rate. The second model class assumes the DM particle is a fermion singlet under the SM gauge group, which couples to a scalar boson which itself mixes with the Higgs boson [48–50]. This fermion singlet model can be described by

$$\mathcal{L}_{\text{fermion}} \supset -\mu_s s^3 - \lambda_s s^4 - y_\chi \bar{\chi}\chi s - \mu_p s|H|^2 - \lambda_p s^2 |H|^2 \tag{2.6}$$

where $s$ is a real scalar mediator, $y_\chi$ is a Yukawa coupling in the dark sector, and the terms $\mu_p$ and $\lambda_p$ provide the Higgs portal between the dark and the SM sectors. The Higgs and the real scalar fields mix due to the portal coupling, $\mu_p$, giving rise to two physical mass eigenstates, $h_1$ and $h_2$. Similar to the scalar DM model, this model allows invisible Higgs decays if it is kinematically possible. It also gives rise to mono-$Z$, mono-$W$ and mono-$H$ signals since the DM cannot be detected.

### 2.2.3. Searches for dark matter interactions

The three classes of dark matter experiments are direct detection, indirect detection and collider experiments. Collider searches are described in Section 2.3.5. Direct detection experiments search for low-energy recoils of matter particles in the detector that occur due to interactions with DM particles passing through the detector. These experiments use noble gas detectors (ZEPLIN-III [51], XENON100 [52], PandaX [53], LUX [54], DarkSide [55]), bubble chambers (PICO [56]), cryogenic detectors (CRESST-II [57], EDELWEISS-III [58], SuperCDMS [59]), germanium detectors (CoGeNT [60]), or silicon charged-coupled devices (DAMIC [61]). The results of direct detection searches are used to place limits on the WIMP-nucleon cross-section. For spin-independent interactions, neutrons and protons are assumed

to contribute equally to the scattering process. For spin-dependent interactions, only the unpaired nucleons contribute to the scattering, therefore only nuclei with an odd number of protons or neutrons are sensitive to these interactions. The latest exclusion limits from various direct search experiments for spin-independent or spin-dependent WIMP-nucleon cross-section as of summer 2017 are shown in Figure 2.2.
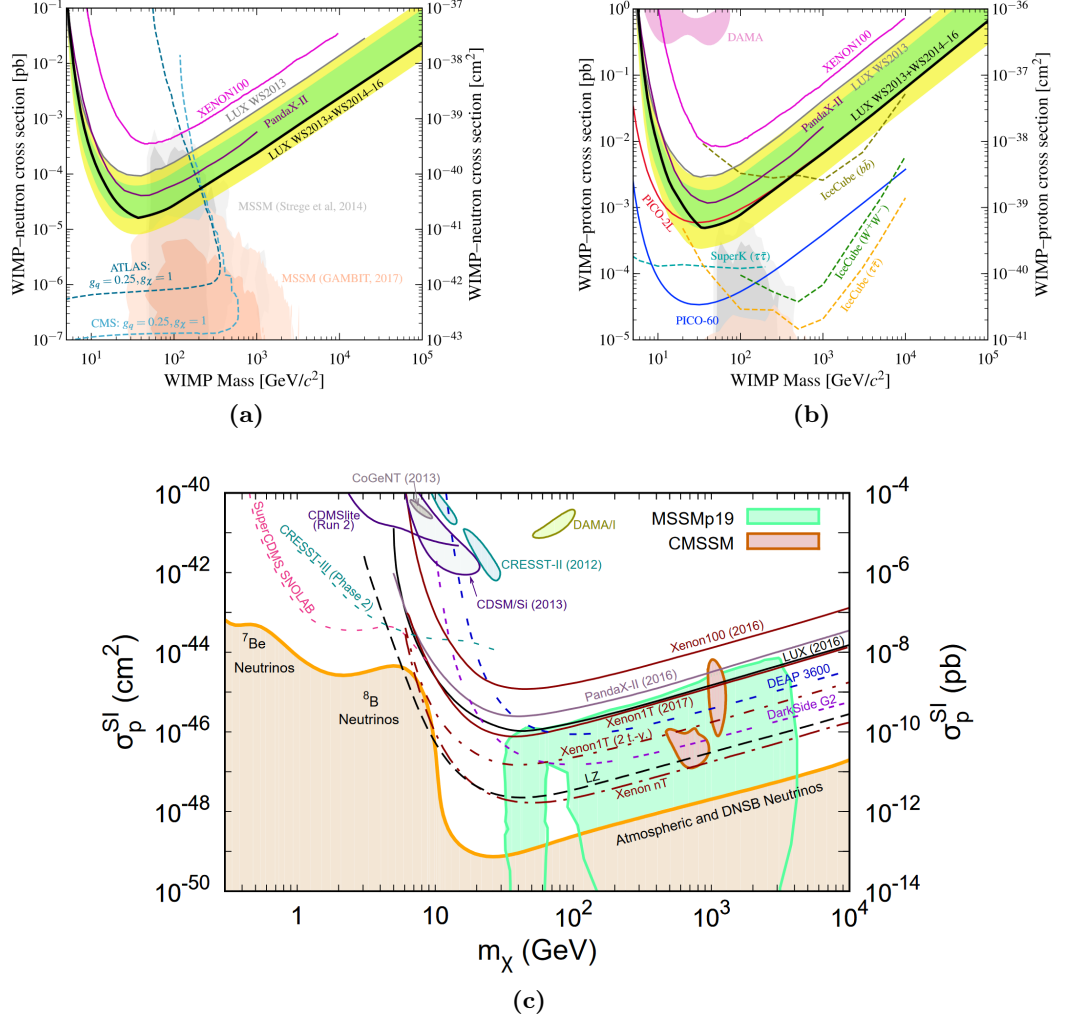


**Figure 2.2.** Exclusion limits from various direct search experiments for (a,b) spin-dependent WIMP-nucleon cross-section [62] assuming (a) pure neutron coupling or (b) pure proton coupling, and (c) spin-independent WIMP-nucleon cross-section [63] as of summer 2017. Current limits for spin-independent WIMP-nucleon cross-section are shown in solid lines, while future projections are shown in dashed lines.

Indirect detection searches are looking for products of the annihilation of DM outside the solar system. These processes can be indirectly detected through an excess of gamma rays or positrons over the expected backgrounds. Indirect detection searches use high-energy neutrino telescopes (IceCube [64], ANTARES [65]), detectors in space (AMS-02 [66], Fermi-

LAT [67]), or neutrino detectors searching for neutrinos produced from WIMP annihilation inside the sun (Super-K [68]). Exclusion limits from various indirect search experiments for spin-independent or spin-dependent WIMP-nucleon cross-section as of summer 2017 are shown in Figure 2.3.
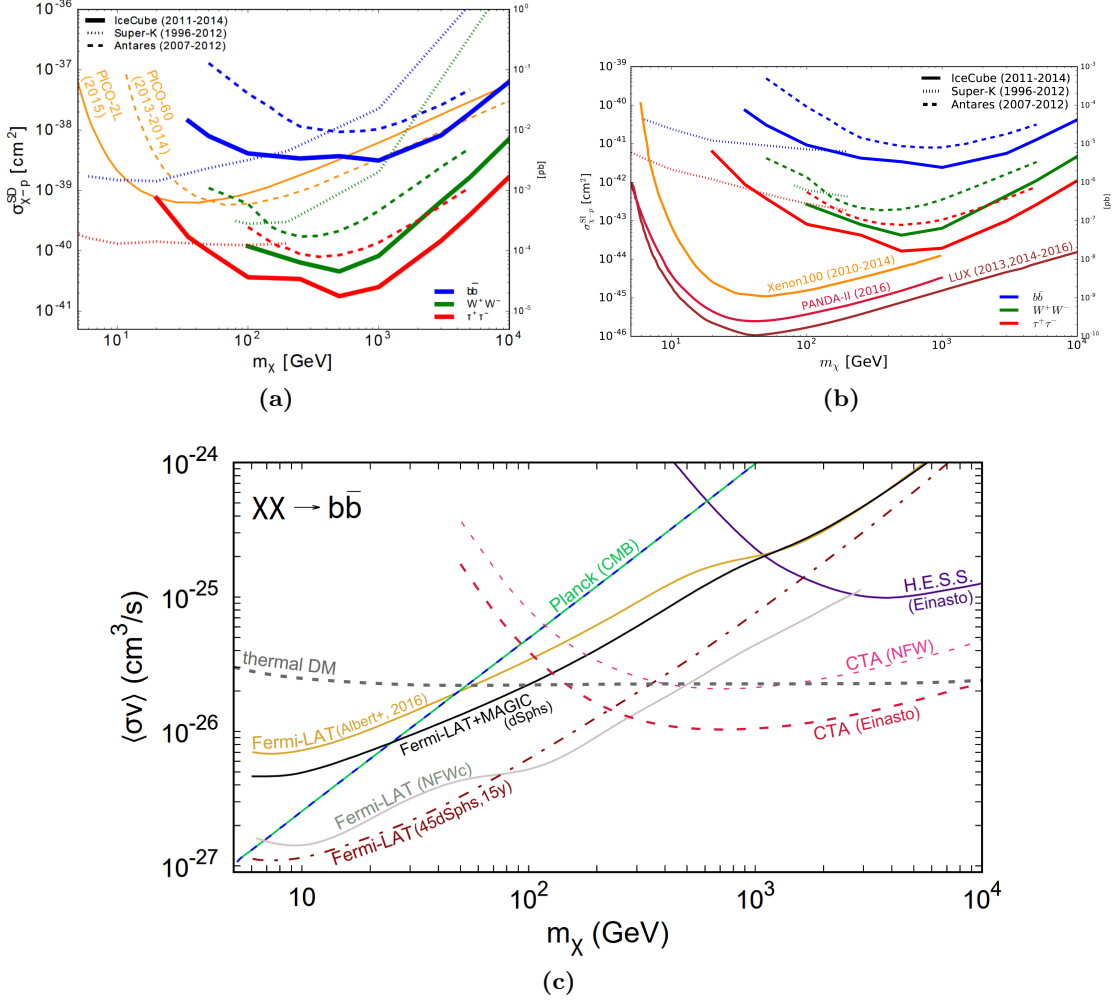


**Figure 2.3.** Exclusion limits for DM annihilation to $b\bar{b}$, $W^+W^-$, and $\tau^+\tau^-$ from various indirect search neutrino telescope experiments (IceCube, Super-K, ANTARES) for (a) spin-dependent WIMP-nucleon cross-section, (b) spin-independent WIMP-nucleon cross-section, including comparisons to direct search experiments [69], and (c) Fermi-LAT [63] for DM annihilation to $b\bar{b}$, as of summer 2017.

## 2.3. Physics of hadron-hadron collisions

### 2.3.1. Cross-section calculation

The colliding protons in hadron-hadron collisions are composed of quarks and gluons, collectively referred to as partons. The probability of a parton carrying momentum fraction, $x$, of the proton momentum is described by the parton distribution function (PDF). The PDFs are not predicted by the SM and are extracted from fits to experimental data, resulting in a variety of available PDF sets [70–72]. The hard process is defined as the process in which heavy objects are created or a large momentum transfer occurs between the colliding partons from each proton.

The cross-section of a process is a measure of the probability of that process to occur. The hadronic cross-section of a process $AB \rightarrow X$ is given by

$$\hat{\sigma}_{AB \rightarrow X} = \int dx_a f_{a/A}(x_a, \mu_F^2) \int dx_b f_{b/B}(x_b, \mu_F^2) \hat{\sigma}_{ab \rightarrow X} \tag{2.7}$$

where $f_{i/j}(x, \mu_F^2)$ ($i = a, b$ and $j = A, B$) are the PDFs for the initial partons $a$ and $b$ from hadrons $A$ and $B$ respectively, describing the long-range interactions, and $\hat{\sigma}_{ab \rightarrow X}$ is the hard process (partonic) cross-section of the short-range interaction. The factorisation scale, $\mu_F$, is a scale that separates long- and short-range interactions. Interactions below the factorisation scale are absorbed into the PDFs [73]. The hard process cross-section is calculated from the matrix element (ME) using perturbation theory, a series expansion of the strong coupling constant, $\alpha_s$. The ME is calculated to some order, such as leading order (LO), next-to-leading order (NLO) or next-to-next-to-leading order (NNLO). Higher-order terms in the ME, above LO, contain virtual corrections (loops) or additional parton emissions radiated by the incoming and outgoing partons in the hard process. Virtual corrections can cause ultraviolet divergences when integrating over the full energy range, which are dealt with using dimensional regularisation in a process referred to as renormalisation [74]. The strong coupling constant is evaluated at the renormalisation scale, $\mu_R$. Example Feynman diagrams for quark-gluon scattering at LO and the Drell-Yan process at NLO with initial state radiation are shown in Figure 2.4.

### 2.3.2. Hadronic final states

The initial partons and possible final state partons can radiate gluons, which are referred to as initial state radiation (ISR) and final state radiation (FSR) respectively. These gluons can radiate other gluons or produce quark-antiquark pairs, resulting in a cascade of additional

(a)                        (b)
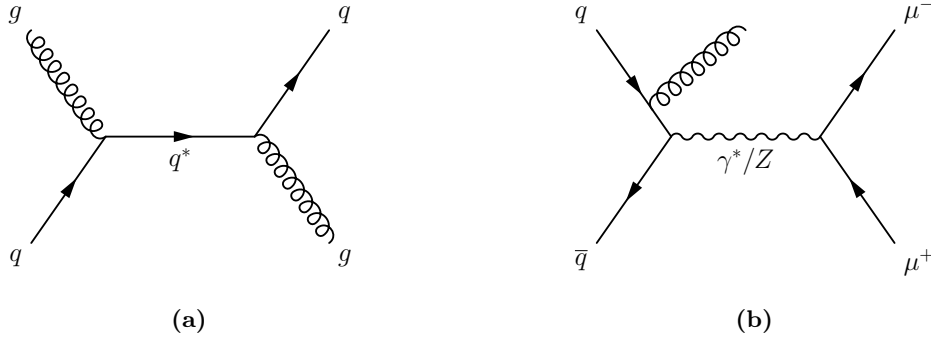
**Figure 2.4.** Feynman diagrams representing (a) quark-gluon scattering and (b) the Drell-Yan process with initial state radiation.

partons. The process evolves in time and decreasing momentum scales until small energy scales (long distances), where $\alpha_s$ becomes large ($\approx \mathcal{O}(1~\text{GeV})$). The coloured partons form colourless hadrons due to confinement in a process referred to as hadronisation, resulting in a final state with collimated streams of hadrons. Hadronisation is not calculable from first principles due to the breakdown of perturbation theory. Phenomenological models are used instead to describe the non-perturbative processes. It is possible that more than one of the incoming partons interact with each other and these additional parton interactions are referred to as multiple parton interactions (MPI), which can produce additional final state partons. The interaction of the proton remnants is referred to as the underlying event (UE).

### 2.3.3. Jet algorithms

Jet algorithms are a way of combining collimated streams of hadrons to closely resemble the partonic scatter. The algorithms should be infra-red and collinear safe, requiring the jet definition to be unchanged with additional soft (low energy) or collinear (small angle) emissions, respectively. There are two classes of jet algorithms, cone algorithms and sequential recombination algorithms. Cone algorithms cluster objects together into cones based on their proximity, producing circular jets. Objects above a certain threshold are selected as seeds for the clustering step. Overlapping cones are typically merged or split depending on the amount of overlap. Cone algorithms are not infra-red and collinear safe, with the exception of the SISCone algorithm [75]. Sequential recombination algorithms repeatedly combine pairs of objects into a single one based on their separation distance. These algorithms are infra-red and collinear safe. The distance between each pair of particles

is given by

$$d_{i,j} = \min(k_{ti}^{2p}, k_{tj}^{2p})\frac{\Delta_{ij}^2}{R^2}, \qquad d_{iB} = k_{ti}^{2p} \qquad (2.8)$$

where $d_{i,j}$ is the distance between objects $i$ and $j$, $k_{ti}$ is the transverse momentum of object $i$, $\Delta_{ij}$ is a measure for the separation of $i$ and $j$, $R$ is the jet-radius parameter of the algorithm, and $d_{iB}$ is the distance between object $i$ and the beam line. The clustering begins by identifying the smallest distances. If $d_{i,j}$ is the smallest then objects $i$ and $j$ are combined, whereas if $d_{iB}$ is the smallest object $i$ is selected as a jet and removed from the list of objects. The distances are recalculated for every object and the procedure is repeated until there are no objects left. The value of the parameter $p$ determines the type of algorithm used. A value of $p = 1$ corresponds to the $k_t$ algorithm [76], $p = 0$ to the Cambridge/Aachen algorithm [77] and $p = $ -1 to the anti-$k_t$ algorithm [78]. The most commonly used jet algorithm is the anti-$k_t$ algorithm which begins clustering using the hardest object. Pairwise clusterings typically contain at least one high-$p_T$ object, that will accumulate all softer objects within a radius, $R$, of its centroid. Figure 2.5 compares jets clustered using four different algorithms. The shapes of the jets formed using the $k_t$ and Cambridge/Aachen algorithms depend on the specific set of soft objects used and change when those are modified. The jets formed using the anti-$k_t$ algorithm have a roughly circular shape of radius $R$.

### 2.3.4. Monte Carlo simulation

High energy proton-proton interactions are modelled using Monte Carlo (MC) event generators. MC event generators are used to generate particle-level predictions of proton-proton collisions [79] in a series of approximations using a variety of tools. The first step is the calculation of the ME for the hard process using perturbation theory to some order. This step is automated for common processes at LO or NLO depending on the generator. The PDF input is usually provided from external libraries.

Parton shower (PS) algorithms are used to probabilistically add additional partons to the final state and evolve them, with potential additional emissions, down to around 1 GeV. Matching procedures, such as the CKKW method [80–82], can be used to merge the ME and PS contributions, removing overlaps between them that typically occur when higher order ME are merged with the PS. MPIs and the UE are also modelled. Non-perturbative models are used to describe the hadronisation of the coloured partons into colourless hadrons. Individual partons do not hadronise independently in these models, instead colour-connected systems of partons hadronise collectively. Two commonly used hadronisation models are
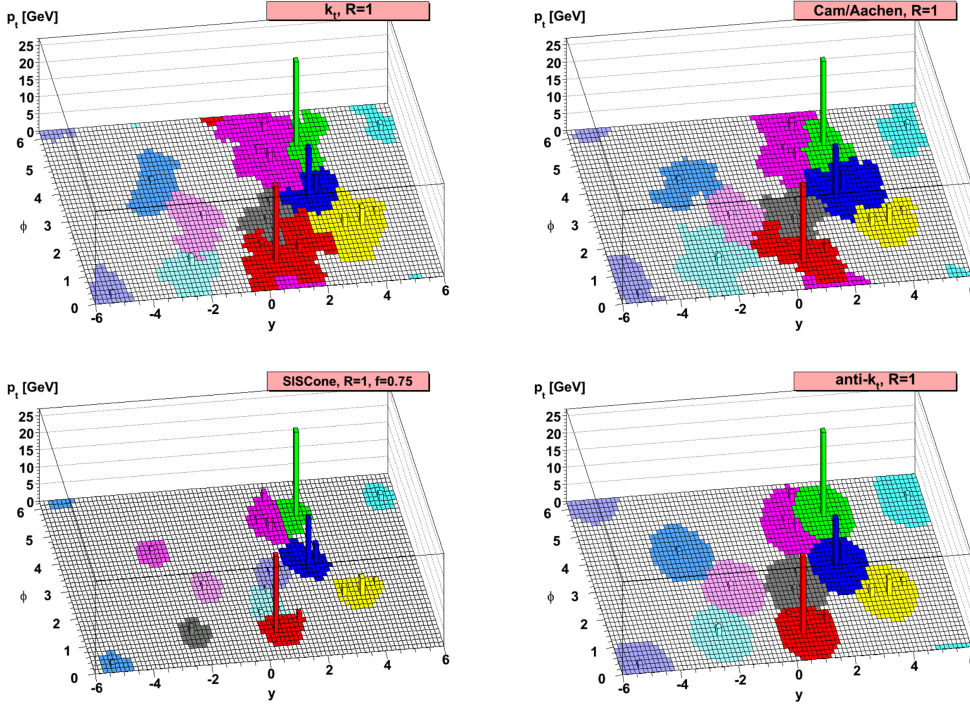
**Figure 2.5.** Parton-level generated event with many random soft objects clustered with four different jet algorithms [78].

the cluster model [83] and the Lund string model [84]. Many of the hadrons produced during hadronisation are excited, requiring dedicated models to simulate their decays into lighter hadrons.

There is a wide range of sophisticated MC generators available. Multi-purpose generators, such as MADGRAPH5_aMC@NLO [85] and SHERPA [86], can calculate a wide range of common MEs at LO and NLO in an automated way. Both generators can also merge multiple MEs with a PS and remove overlaps between them. SHERPA provides its own PS while an external PS program needs to be provided for MADGRAPH5_aMC@NLO. The POWHEG-BOX [87–89] generator can generate MEs up to NLO for specific processes, but needs to be interfaced to another generator for the simulation of the PS, hadronisation and UE, such as the PYTHIA [90–92] or HERWIG [93] families of PS programs.

### 2.3.5. Dark matter searches in hadron-hadron collisions

Collider searches at the LHC [94] look for direct pair-production of DM in association with additional SM particles. The experimental signature of DM at the LHC is missing transverse momentum since it would be invisible to the detectors. Popular DM searches are

concerned with the production of a single SM particle in association with missing transverse momentum, and are referred to as mono-X searches, where the X can be a jet, a vector boson, or a Higgs boson. Mono-jet searches [95, 96] look for DM production in association with at least one energetic jet from initial state radiation. Mono-$V$ searches look for DM produced in association with a vector boson that is radiated off a quark in the initial state. The production cross-section of mono-V events is significantly smaller than that of mono-jet events at the LHC, however the process is much cleaner. Mono-photon [97, 98] and mono-$Z$ searches with the $Z$ boson decaying leptonically [99, 100] have a clean signal with relatively low backgrounds. Mono-$Z$ and mono-$W$ searches in the hadronic final state [101] are similar to mono-jet searches but use a larger jet-radius parameter for the leading jet and require its mass to be consistent with a $W$ or $Z$ boson. Mono-$W$ searches with the $W$ boson decaying leptonically [102, 103] are more challenging because the neutrino adds to the missing transverse momentum and the experimental signature is identical to the leptonic decay of an off-shell $W$ boson. The last of the mono-X searches is the mono-Higgs search, looking for DM produced in association with a SM-like Higgs boson in the $\gamma\gamma$ [104] or $b\bar{b}$ [105, 106] final states. The former has a clean signature while the latter has a large background contamination. If DM couples dominantly to heavy quarks, a promising search is to look for a top quark pair [107, 108] or a single top quark [109] in association with missing transverse momentum. Another promising search is looking for pairs of DM particles produced in invisible Higgs decays [110, 111]. A different type of model-agnostic searches makes use of the large production cross-sections of two-jet (di-jet) events to search for di-jet resonances [112–115] in the invariant mass distribution of the two leading jets. The results from the di-jet resonance searches can be used to set limits on a variety of BSM models, including excited quarks, new heavy vector bosons, or quantum black holes. The latest exclusion limits from the ATLAS [8] and CMS [116] experiments in the DM mass-mediator mass plane for an axial-vector mediator are shown in Figure 2.6.
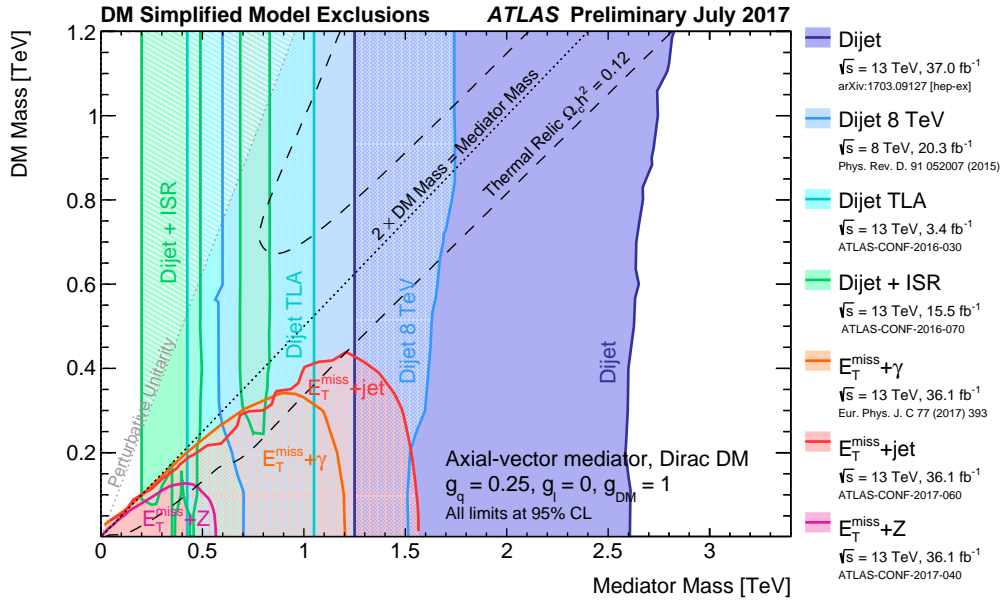
**(a)**
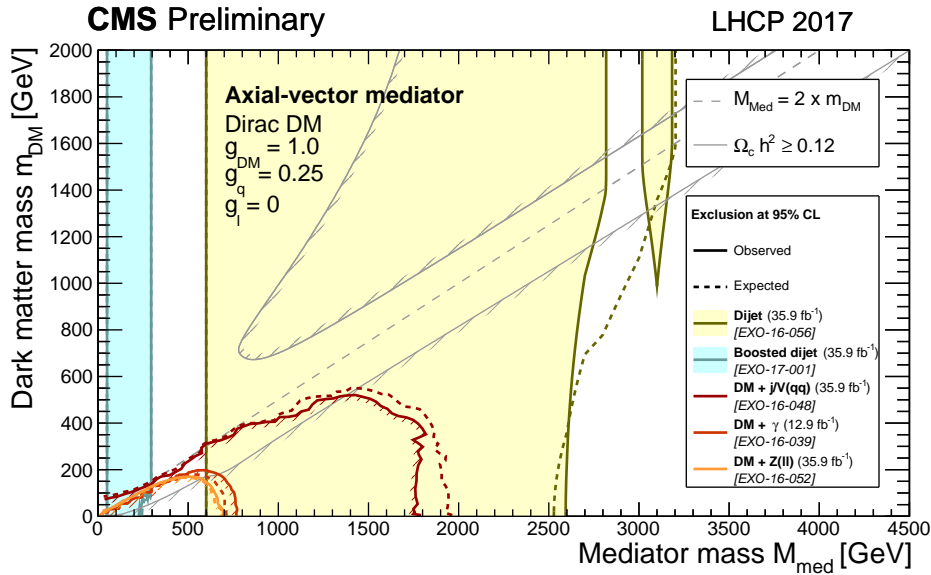


**(b)**

**Figure 2.6.** Exclusion limits with 95% CL in the DM mass-mediator mass plane from the (a) ATLAS [117] and (b) CMS [118] experiments as of summer 2017. The mediator is an axial-vector and couplings are set to $g_q = 0.25$ and $g_\chi = 1$.

# Chapter 3.

# The ATLAS detector and the LHC

## 3.1. The Large Hadron Collider

The LHC is the largest particle accelerator in the world located at the European Organization for Nuclear Research (CERN) near Geneva, Switzerland. It is a circular proton-proton collider with a circumference of 27 km and located in a tunnel approximately 100 m underground. The LHC is designed to collide protons at a centre-of-mass energy of $\sqrt{s} = 14$ TeV and has reached $\sqrt{s} = 13$ TeV in 2015.

The accelerator chain and the four main experiments are shown in Figure 3.1. The proton source is a cylinder of hydrogen gas. An electric field is used to strip electrons from the hydrogen atoms, producing protons. The first accelerator in the chain is LINAC 2, a linear accelerator that accelerates the protons to 50 MeV. The protons are then injected into the Proton Synchrotron Booster (PSB), which accelerates them to 1.4 GeV, followed by the Proton Synchrotron (PS), which increases the energy to 25 GeV. The last accelerator in the chain before the LHC is the Super Proton Synchrotron (SPS) which accelerates the protons to 450 GeV. The protons are then transferred to the two LHC beam pipes, one beam circulating clockwise and the other anti-clockwise, where is takes about 20 min for the protons to reach 6.5 TeV.

In addition to proton-proton collisions, the LHC is also used for lead-lead and proton-lead collisions. Lead ions are produced from vaporised lead. They first enter LINAC 3 and are accelerated in the Low Energy Ion Ring (LEIR), subsequently following the same route as the protons. The LHC supports four main independent experiments, ATLAS (A Toroidal LHC ApparatuS) [8], CMS (Compact Muon Solenoid) [116], LHCb (LHC beauty) [119], and ALICE (A Large Ion Collider Experiment) [120]. ATLAS and CMS are general-purpose detectors investigating a wide range of physics, LHCb specialises in matter-antimatter asymmetry, and ALICE specialises in heavy-ion collisions.
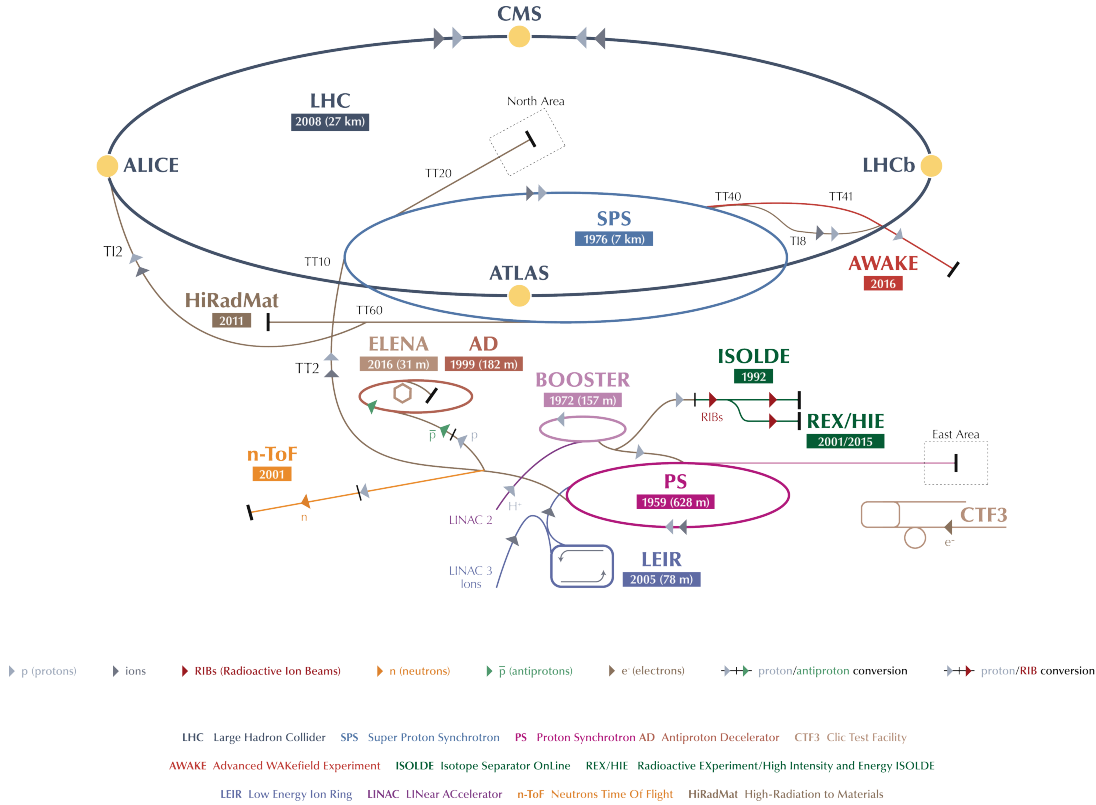
**Figure 3.1.** Overview of the CERN accelerator complex [121].

The accelerated protons are arranged into bunches within each LHC beam. One of the most important parameters of an accelerator is the instantaneous luminosity, $L$, which is a measure of the rate of collisions, given by

$$L = \frac{n_b f_r n_1 n_2}{2\pi \Sigma_x \Sigma_y} \tag{3.1}$$

where $n_b$ is the number of bunch pairs colliding per revolution, $f_r$ is the LHC revolution frequency of 11.245 kHz, $n_1$ and $n_2$ are the number of protons per bunch in each of the two beams, and $\Sigma_x$ and $\Sigma_y$ characterise the horizontal and vertical convolved beam widths. Dedicated beam-separation scans, also known as van der Meer scans [122, 123], are used to measure $\Sigma_x$ and $\Sigma_y$ by separating the beams in steps of a known distance. The integral of the instantaneous luminosity over the data-taking period is known as the total integrated luminosity, and is denoted by $\int L dt$.

The LHC has been operational since 2010 with two runs, referred to as Run-1 and Run-2 in 2010–2012 and 2015–2018, respectively. The long shutdown in 2013–2015 is referred to as LS1. In 2015, the LHC collided protons at a centre-of-mass energy of $\sqrt{s} = 13$ TeV with a peak instantaneous luminosity of $5 \times 10^{33}$ cm$^{-2}$s$^{-1}$, an event rate of up to 40 MHz

and a bunch spacing of 25 ns. The LHC has delivered $4.2\,\text{fb}^{-1}$ to ATLAS in 2015 with an average of 13.7 interactions per bunch crossing (pileup) [124]. ATLAS has recorded $3.9\,\text{fb}^{-1}$ due to the inefficiency of the data acquisition system and the time needed to turn on the high-voltage of certain sub-detectors. The total integrated luminosity recorded by ATLAS that has been certified of having good quality for physics analyses is $3.2\,\text{fb}^{-1}$ with an uncertainty of 2.1%. Figure 3.2 shows the mean number of interactions per bunch crossing and the total integrated luminosity delivered by the LHC, recorded by ATLAS, and certified to be of good quality data in 2015.
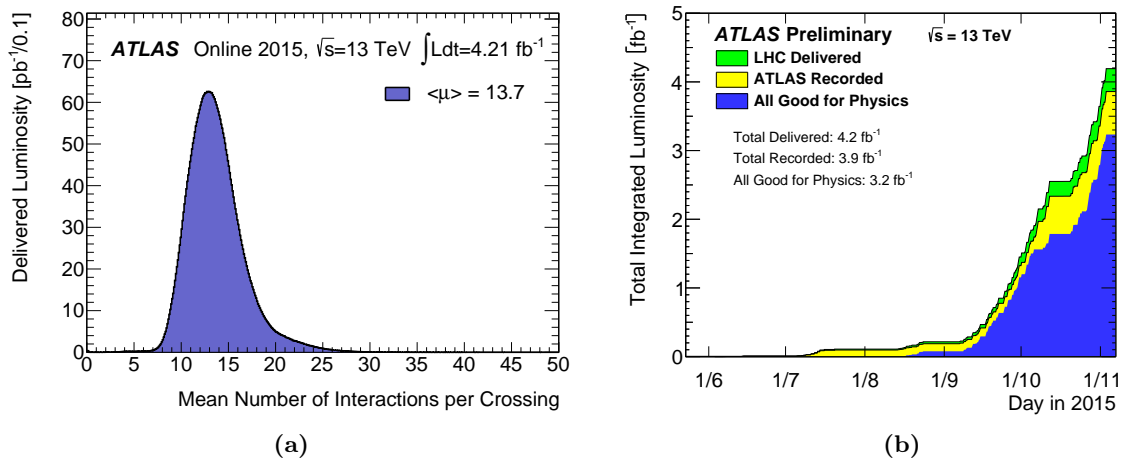


**Figure 3.2.** (a) Mean number of interactions per bunch crossing calculated from the instantaneous per bunch luminosity and (b) total integrated luminosity versus time delivered to ATLAS, recorded by ATLAS, and certified to be of good quality data in 2015 [124].

## 3.2. The ATLAS detector

ATLAS has cylindrical geometry around the beam line and consists of an inner detector, a calorimeter system, a muon spectrometer, a thin superconducting solenoid magnet and three large superconducting toroids. It has a height of 25 m, a length of 44 m and weighs approximately 7000 t as shown in Figure 3.3.

### 3.2.1. ATLAS coordinate system

A right-handed coordinate system is used with its origin at the nominal interaction point at the centre of the detector. The beam direction defines the $z$-axis, the positive $x$-axis is defined as pointing from the interaction point to the centre of the LHC ring, and the positive $y$-axis is defined as pointing away from the centre of earth. The detector is defined
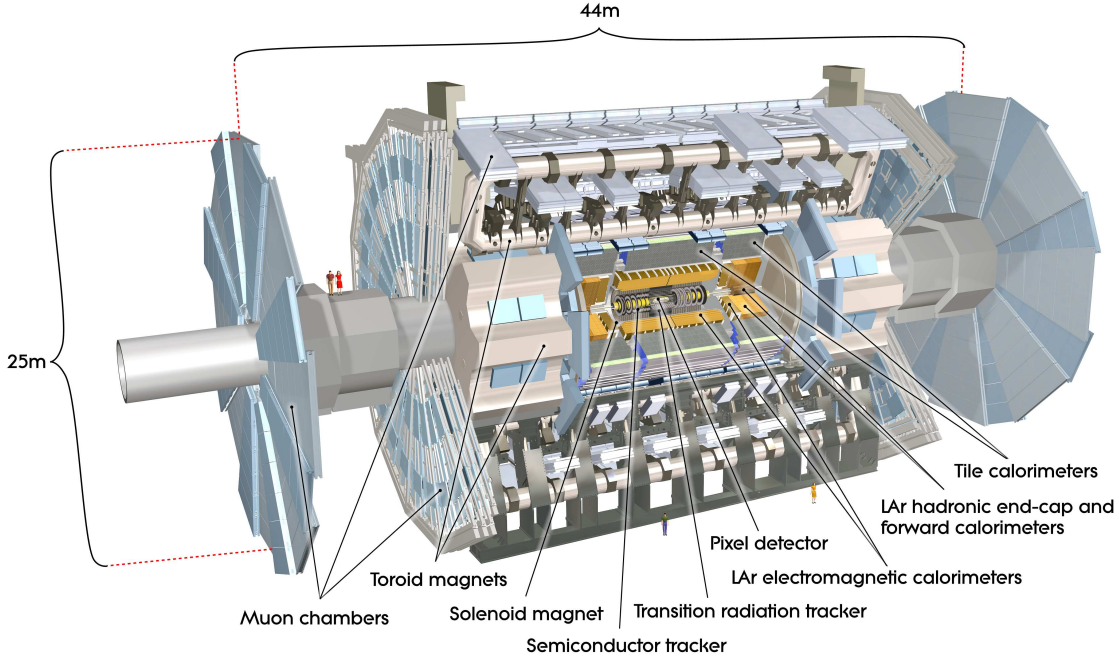
**Figure 3.3.** Cut-away view of the ATLAS detector [8].

to have two sides, A and C, corresponding to positive and negative $z$. The polar angle $\theta$ is the angle from the z-axis and the azimuthal angle $\phi$ is measured in the plane transverse to the beam. The particle energy is denoted by $E$, the particle momentum by $\vec{p} = (p_x, p_y, p_z)$ and the invariant mass by $m$. The rapidity is defined as $y = 1/2 \ln[(E + p_z)/(E - p_z)]$, the pseudorapidity is defined as $\eta = -\ln \tan(\theta/2)$ and the distance $\Delta R$ in $\eta$ - $\phi$ space is defined as $\Delta R = \sqrt{(\Delta \eta^2 + \Delta \phi^2)}$. Transverse quantities are defined in the $x - y$ plane, such as transverse momentum, $p_T$, transverse energy, $E_T = E \sin \theta$, and missing transverse momentum, $p_T^{miss}$ (also commonly referred to as $E_T^{miss}$).

### 3.2.2. The inner detector

The inner detector (ID) is the closest detector to the interaction point and provides precise position and momentum measurements of charged particles with $p_T > 400$ MeV within $|\eta| < 2.5$. It is immersed in a 2 T axial magnetic field generated by a thin superconducting solenoid. The magnetic field bends the tracks of charged particles allowing a momentum measurement from the curvature of the tracks. The ID consists of the silicon pixel detector, the semiconductor tracker (SCT) and the transition radiation tracker (TRT). The

specification momentum resolution of the ID is given by

$$\frac{\sigma_{p_\mathrm{T}}}{p_\mathrm{T}} = a \times p_\mathrm{T} \oplus b \tag{3.2}$$

with $a = 0.05\%$, $b = 1\%$, where the units of $p_\mathrm{T}$ are in GeV.

The pixel detector consists of three barrel layers and six end-cap discs with the highest granularity, providing on average three measurements per charged particle. The pixel detector consists of $1\,744$ sensor modules, each containing $47\,232$ pixel sensors of size $50 \times 400$ µm$^2$. The intrinsic position resolution per layer is 10 µm in the transverse plane ($R$ - $\phi$) and 115 µm in the axial plane ($z$, barrel) or radial plane ($R$, end-caps). A fourth layer, the insertable b-layer (IBL) [125], has been added to the pixel detector, between the inner pixel layer and a new beam pipe, both of which have been installed during LS1, to improve vertex identification and flavour tagging performance. A preliminary estimate of the resolution of the IBL is 10 µm in $R$ - $\phi$ and 66.5 µm in $z$ [126].

The SCT surrounds the pixel detector and contains $15\,912$ silicon microstrip sensors arranged into four barrels and eighteen end-cap discs. The arrangement of the barrels and the end-cap discs ensures that a particle passes through four levels of sensors, generating on average eight SCT hits. The intrinsic resolution per module is 17 µm in $R$ - $\phi$ and 580 µm in $z$ (barrel) or $R$ (end-caps). The silicon tracking detectors (pixel and SCT) cover the region $|\eta| < 2.5$.

The TRT is the largest and outermost component of the ID, a combined transition radiation detector and tracking detector. The TRT is made of polymide straw tubes filled with a Xenon-based gas mixture, typically producing 36 hits per track, up to $|\eta| = 2.0$, with a resolution of 130 µm in $R$ - $\phi$. A charged particle passing through the gas straw tubes ionizes the gas producing ionization electrons used for drift-time measurements. Electrons are typically the only particles light enough to be ultra-relativistic and radiate photons (i.e. produce transition radiation) as they pass through the gas mixture and polymide straws. The number of transition radiation photons can be used to discriminate between electrons and charged hadrons up to approximately 150 GeV.

### 3.2.3. The calorimeter system

The calorimeter system surrounds the ID and covers the range $|\eta| < 4.9$. It measures the energy of photons, electrons and hadrons, and stops them before they reach the muon system. Muons are minimum ionising particles and leave little energy in the calorimeter system. Neutrinos are non-interacting and pass through the entire detector undetected.

The calorimeter system consists of the electromagnetic, hadronic, and forward sampling calorimeters. Sampling calorimeters use alternating layers of absorbing and active material. The absorbing material forces an interaction as particles traverse the calorimeters and the active material measures the energy of the showers. Only a fraction of the particle energy is measured, but the energy of the full shower can be inferred from the observed energy. The specification energy resolutions are given by

$$\frac{\sigma_E}{E} = \frac{a}{\sqrt{E}} \oplus b \qquad (3.3)$$

with $(a, b) = (10\%, 0.7\%)$ for the EM, $(50\%, 3\%)$ for the hadronic and $(100\%, 10\%)$ for the forward calorimeter, where the units of $E$ are in GeV.

The electromagnetic (EM) calorimeter is divided into a barrel part with $|\eta| < 1.475$ and two end-cap components with $1.375 < |\eta| < 3.2$. It is a lead-liquid Argon (LAr) detector that uses an accordion geometry to provide complete azimuthal coverage. The barrel and end-caps comprise three layers with different depths and granularities. The first layer consists of fine cells with size $\Delta\eta \times \Delta\phi = 0.0031 \times 0.098$, the second layer collects most of the energy using cells with size $\Delta\eta \times \Delta\phi = 0.025 \times 0.0245$, and the third layer is coarser consisting of cells with size $\Delta\eta \times \Delta\phi = 0.05 \times 0.0245$. A presampler detector consisting of an active LAr layer is used in the region $|\eta| < 1.8$ to correct for the energy lost by electrons and photons in material before the EM calorimeter.

The hadronic calorimeter consists of a tile barrel calorimeter with two extended barrels and a LAr end-cap calorimeter. The tile calorimeter is a sampling calorimeter that uses scintillator tiles as the active material and steel as the absorber, and is placed directly outside the EM calorimeter envelope. Its barrel covers the region $|\eta| < 1.0$ and its two extended barrels cover the range $0.8 < |\eta| < 1.7$. The tile calorimeter has coarser granularity than the EM calorimeter with cells of size $\Delta\eta \times \Delta\phi = 0.1 \times 0.1$ in the first layers. The hadronic end-cap calorimeter (HEC) is located directly behind the end-cap EM calorimeter. It uses LAr as the active material with copper as the absorber and consists of two independent wheels per end-cap covering the range $1.5 < |\eta| < 3.2$. The size of the cells is $\Delta\eta \times \Delta\phi = 0.1 \times 0.1$ in the region $|\eta| < 2.5$ and $0.2 \times 0.2$ for larger $\eta$ values.

The forward calorimeter (FCal) also uses LAr as the active material and covers the range $3.1 < |\eta| < 4.9$. It consists of three separate layers, the first is an EM calorimeter with copper as the absorber and the remaining two are hadronic calorimeters with tungsten as the absorber.

Figure 3.4 shows particles passing through a transverse slice of the detector. The magnetic field bends the tracks of charged particles whereas neutral particles leave no tracks.
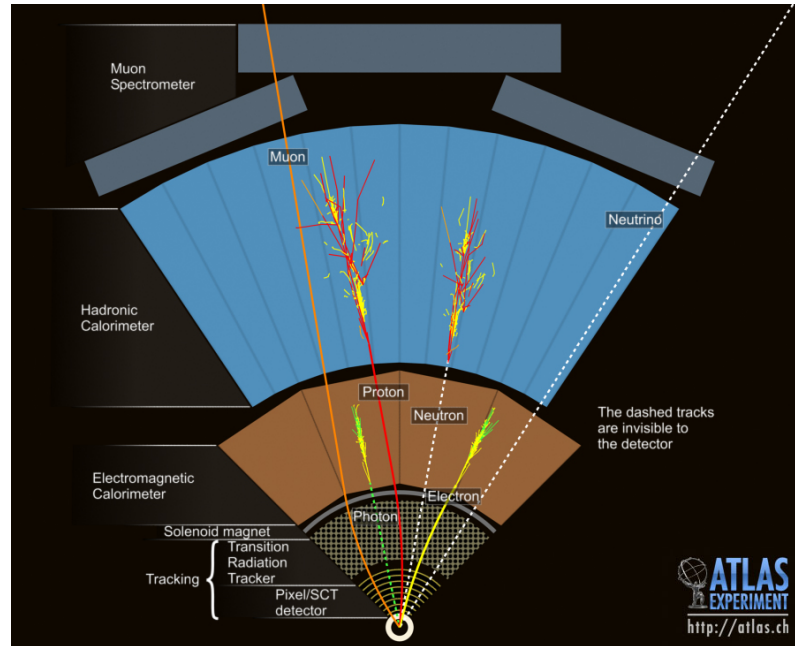
**Figure 3.4.** Schematic of a transverse slice of the detector showing particles passing through [127]. The tracks and patterns of energy deposits allow the identification of the different types of particles produced in the collisions as described in Section 3.3.

Electromagnetic showers from electrons and photons are contained in the EM calorimeter. The average distance of material that must be traversed to reduce the energy of an electron to $1/e$ of the initial value is referred to as the radiation length. The total thickness of the EM calorimeter is more than 22 radiation lengths in the barrel and more than 24 in the end-caps, enough to fully contain EM showers. Hadrons can travel much further in a material before undergoing a hadronic interaction compared to an EM interaction. The average distance travelled by a hadron before undergoing an inelastic collision with the surrounding material is referred to as the interaction length. The thickness of the calorimeter system is about 9.7 interaction lengths in the barrel and 10 in the end-caps, which is adequate to contain most hadron showers. Very energetic hadronic showers can pass through the calorimeter resulting in a loss of a large fraction of the shower energy, reducing the calorimeter response. This is known as punch-through and is most problematic for very high-$p_{\mathrm{T}}$ jets.

### 3.2.4. The muon system

The muon spectrometer (MS) measures muon momentum based on the magnetic deflection of muon paths in a magnetic field. The magnetic field is generated by three large supercon-ducting air-core toroid magnets, one barrel producing a 0.5 T toroidal magnetic field and two

end-caps each producing 1 T magnetic fields. The specification muon momentum resolution is 10% for muon $p_\mathrm{T} = 1$ TeV. The MS consists of a barrel and two end-caps covering the region $|\eta| < 2.7$. Monitored drift tubes (MDTs) provide a precision measurement of the track coordinates in the principal bending direction of the magnetic field over most of the pseudorapidity range, with a position resolution of 35 μm in the axial plane. Cathode strip chambers (CSCs) are multiwire proportional chambers with cathodes segmented into strips with higher granularity. These are used at large pseudorapidities, $2.0 < |\eta| < 2.7$, with a position resolution of 40 μm in the radial plane. The muon trigger system consists of resistive plate chambers in the barrel and thin gap chambers in the end-cap region and covers the range $|\eta| < 2.4$.

### 3.2.5. The trigger system

It is impossible to record all events at such a high event rate of up to 40 MHz. The first constraint is the detector readout capability of up to about 100 kHz to prevent excessive dead time. The second constraint is the offline computing model, limiting the bandwidth and storage, where each recorded event is about 1.5 MB. The ATLAS trigger system is used to select only those events containing objects with high transverse momentum. It has two distinct levels, Level 1 (L1) and the High Level Trigger (HLT).

The L1 trigger performs the initial event selection based on information from the calorimeters and muon spectrometer. It identifies signatures from high-$p_\mathrm{T}$ electrons, photons, jets, muons, hadronically decaying tau leptons, and events with large missing transverse momentum or large total transverse momentum. The L1 trigger reduces the event rate to less than 100 kHz and its decision must reach the front-end electronics within 2.5 μs to enable detector read-out. The regions of the detector where the L1 trigger has identified high-$p_\mathrm{T}$ objects are called regions of interest (RoIs).

The HLT trigger is typically seeded by the L1 RoIs and uses offline analysis procedures on fully reconstructed events to further reduce the event rate to 1 kHz in an average processing time of approximately 235 ms at the highest instantaneous luminosity [128]. The RoI can be used to read out a limited selection of the detector, to reduce the amount of data transferred from the detector readout. Algorithms used for triggers and data acquisition (DAQ) are referred to as online algorithms, whereas algorithms that are used on the recorded data are referred to as offline algorithms. An online algorithm processes its input piece-by-piece in a serial fashion without having the entire input available from the start.

The trigger menu defines the list of all L1 and HLT triggers used for data collection. It is optimised to allow the broadest possible range of physics studies using a variety of different final states constructed from electrons, muons, photons, jets, hadronically decaying tau leptons, or missing transverse momentum. This trigger menu contains "primary triggers" used for physics analyses, "support triggers" used for efficiency measurements or monitoring, and "calibration triggers" used for detector calibration. The total rate available is limited and prescale factors are used to maximising the physics output within the rate and bandwidth constraints. The prescale factors can be applied to L1 and HLT triggers and changed during data taking to either disable certain triggers or limit the number of events accepted by them. The primary triggers are typically unprescaled so all events satisfying those algorithms are recorded, whereas support triggers are prescaled to run at a small constant rate of about 0.5 Hz each.

## 3.3. Object reconstruction and identification

### 3.3.1. Tracks

Charged particles traversing the detector deposit energy in the various detector sensors. Track reconstruction [129] identifies the trajectories of charged particles from the hits in the sensors and determines their origin, direction, and momentum. An inside-out algorithm [130] is used to reconstruct tracks with $p_{\mathrm{T}} > 400$ MeV, starting from three-point hits in the pixel and SCT, and adding hits moving away from the interaction point. Ambiguities in the track candidates are resolved before extending the tracks to the TRT. A back-track algorithm is used to reconstruct particles produced in secondary interactions, starting from segments in the TRT and extending them inwards by adding hits from the SCT and pixel. Intersections of the reconstructed track trajectory with sensors that do not result in a hit are referred to as holes. A hit in the pixel detector shared by more than one track or two shared hits in the same SCT layer are referred to as a shared module. Tracks are typically required to have a very small number of holes and shared modules. A set of *Loose* selection criteria [131] is applied to all reconstructed tracks in the ID. These tracks are used in the reconstruction and identification of other objects.

### 3.3.2. Jets

Jets are the most common high-$p_{\mathrm{T}}$ objects produced in proton-proton interactions and are an important component of a wide range of physics analyses. They are typically reconstructed from calorimeter energy deposits, clustered to form topological clusters (topo-clusters) using

a topological clustering algorithm [132], which groups together neighbouring cells as long as the signal in the cells is significant compared to noise. Topo-clusters are treated as massless particles, are assumed to originate from the centre of the detector, and are calibrated by default at the EM calorimeter energy scale [133–135]. It is also possible to use the local cluster weighting (LCW) calibration method [136] to classify topo-clusters as having either electromagnetic or hadronic origin. Jets are reconstructed from topo-clusters using the anti-$k_t$ jet clustering algorithm with a jet-radius parameter of $R = 0.4$ or $R = 1.0$, with the former used as the default.

The jet energy needs to be corrected for experimental effects, such as calorimeter non-compensation, energy losses due to dead material, leakage at the outer edge of the calorimeters, and pileup. The jet calibration procedure [137] is based on a sequential series of corrections. The first step is the origin correction, which corrects the direction of jets to point back to the primary vertex, defined as the collision vertex with the highest sum of squared transverse momenta of associated inner detector tracks with $p_\mathrm{T} > 400$ MeV. An area-based subtraction process and a residual pileup correction [138, 139] are then applied to mitigate the effect of pileup. The next step is a jet energy scale (JES) correction, which is derived from MC and corrects the jet energy to the particle-level energy scale [140]. Additional corrections known as global sequential corrections (GSC) [141], are applied to reduce the difference in response between quark and gluon initiated jets and also correct for very high-$p_\mathrm{T}$ jets whose energy is not fully contained in the calorimeter. The final step applies a residual in-situ correction [142] to jets reconstructed in data only. This includes the di-jet $\eta$-intercalibration [143], in which jets in the intermediate to forward region (0.8 $< |\eta| < 4.5$), with no tracking information when $|\eta| > 2.5$, are calibrated relative to jets in the central region ($|\eta| < 0.8$), to remove any residual pseudorapidity difference in the jet response after MC calibration.

Jets not originating from the proton-proton interactions, referred to as fake jets, are rejected using jet quality criteria in a procedure known as jet cleaning. Fake jets arise from non-collision backgrounds, which include beam induced backgrounds due to proton losses upstream of the interaction point and cosmic-ray showers produced in the atmosphere overlapping with the collision events. Another source of fake jets is calorimeter noise from large scale coherent noise or isolated pathological cells. Two jet quality criteria are defined, *LooseBad* and *TightBad*, with efficiencies of over 99.5% and 95% respectively for jets with $p_\mathrm{T} > 20$ GeV and increase to 99.9% and 99.5% for jets with $p_\mathrm{T} > 100$ GeV [144]. Pileup jets are rejected by requiring jets with $20 < p_\mathrm{T} < 50$ GeV and $|\eta| < 2.4$ to satisfy the jet-vertex-tagger requirement, JVT $> 0.64$ [145]. The JVT uses a two-dimensional likelihood to determine if jets originate from the primary vertex or pileup, with an average efficiency of 92% for the JVT $> 0.64$ requirement.

### 3.3.3. Electrons

Electrons are reconstructed from energy clusters in the EM calorimeter associated with a track in the ID. Calorimeter cells are clustered using a sliding window algorithm [146] which sums cells within a fixed-size rectangular window. The size of the window is $3 \times 5$ in units of $\Delta\eta \times \Delta\phi = 0.025 \times 0.0245$, corresponding to the granularity of the second layer of the EM calorimeter, and is used to search for seeds with $E_{\mathrm{T}} = 2.5$ GeV. The cluster search has an efficiency of 95% for electrons with $E_{\mathrm{T}} = 7$ GeV and more than 99% for electrons with $E_{\mathrm{T}} > 15$ GeV. Cluster seeds with no associated tracks are considered to originate from photons and are removed. Clusters are re-formed using a window of size $3 \times 7$ in the barrel and $5 \times 5$ in the end-caps of the EM calorimeter. Multivariate analysis (MVA) techniques based on MC simulation of $Z \to e^+e^-$ are used to calibrate the energy of the clusters [147]. The energy of the electron is computed from the calibrated cluster energy and the direction from the associated track. A likelihood-based method using EM shower shape and track quality variables is used to suppress fake electrons, mainly from charged pions and jets. Three electron likelihood identification working points are defined, *Loose*, *Medium* and *Tight*, with efficiencies of 92%, 87% and 78% respectively for electrons with $E_{\mathrm{T}} = 25$ GeV [148]. Electrons are typically required to be isolated from other particles by applying isolation criteria. There are seven isolation working points using either track-based isolation criteria or track-based and calorimeter based isolation criteria, relying on the scalar sum of the $p_{\mathrm{T}}$ of tracks or the sum of the $E_{\mathrm{T}}$ of topo-clusters in a cone around the electron. A commonly used isolation working point is the *LooseTrackOnly* that uses only track-based isolation criteria and has a 99% efficiency [148].

### 3.3.4. Photons

Photons are reconstructed from energy clusters in the EM calorimeter following the same procedure used for electrons. Photons are neutral and leave no tracks in the ID, but they can convert to an electron-positron pair. Electrons can also produce photons via bremsstrahlung. Photons with no associated tracks are referred to as unconverted photons whereas photons associated with a pair of oppositely-charged tracks compatible with electrons are referred to as converted. The properties of the EM showers are used to define a set of *Loose* and *Tight* photon identification working points. The efficiency of the *Tight* working point is around 90% for unconverted photons and 97% for converted photons with $E_{\mathrm{T}} > 100$ GeV [149]. No dedicated photon selection is considered in this thesis; however, the energy deposits of the photons are included in the jet reconstruction and so they are technically treated as jets.

### 3.3.5. Tau leptons

Tau leptons are the only leptons heavy enough to decay into hadrons with a probability of around 65%. Hadronic tau lepton decays are classified into two caterogies, one-prong and three-prong, depending on the number of charged pions produced, with the former being the most common type. Hadronically decaying tau leptons are reconstructed using jets as seeds, which are formed from LCW calibrated topo-clusters using the anti-$k_t$ algorithm with a radius parameter of $R = 0.4$, satisfying $p_T > 10$ GeV and $|\eta| < 2.5$. The energy of tau leptons is calibrated back to the true visible energy using the tau energy scale (TES) calibration. It subtracts energy contributions originating from pileup and applies a response correction to account for decay products not reaching the calorimeter, not depositing enough energy to create topo-clusters, or not detected within $\Delta R < 0.2$ of the tau lepton. The visible momentum of the tau lepton is calculated from the energy assuming zero mass. Boosted decision tree (BDT) algorithms, separately trained for one-prong and three-prong decays, are used to discriminate hadronic tau lepton decays from jets. Three tau lepton identification working points are defined, *Loose*, *Medium* and *Tight*, with efficiencies of 60%, 55% and 45% for one-prong tau leptons and 50%, 40% and 30% for three-prong tau leptons respectively [150]. The BDT algorithms provide insufficient discriminating power between electrons and one-prong tau leptons. One-prong tau leptons matched to an electron with $p_T > 5$ GeV and a large electron likelihood score within $\Delta R < 0.4$ are rejected. This cut has a 95% efficiency for tau leptons passing the *Loose* identification working point.

### 3.3.6. Muons

Muons are reconstructed using a combination of track information from the ID and the MS. There are four muon types depending on which sub-detectors are used for the reconstruction. *Combined* muons are the primary type, formed by combining tracks which have been independently reconstructed in the ID and the MS. *Segment-tagged* muons are typically low-$p_T$ with $|\eta| < 0.1$, formed by a track in the ID that when extrapolated to the MS is associated with at least one track segment in the MDT or CSC. *Calorimeter-tagged* muons have the lowest purity but recover acceptance in the region $|\eta| < 0.1$, formed by a track in the ID matched to a calorimeter energy deposit that is compatible with a minimum ionizing particle. Finally, *Extrapolated* muons extend the acceptance into the region 2.5 $< |\eta| < 2.7$, formed by a track in the MS that is loosely compatible with originating from the interaction point. The muon momentum and resolution in the MC are calibrated using di-muon invariant mass measurements of $Z \to \mu^+\mu^-$ and $J/\psi \to \mu^+\mu^-$, to precisely describe the momentum and resolution in data. Muons are identified using track quality requirements that suppress backgrounds from fake tracks and muons from hadron decays,

mainly pion and kaon decays. Four muon identification working points are defined, *Loose*, *Medium*, *Tight* and *High-$p_T$*, with efficiencies of 98%, 96%, 92% and 80% respectively for muons with $20 < p_T < 100$ GeV [151]. As for electrons, muons are also typically required to be isolated from other particles by applying isolation criteria. The same seven isolation working points used for electrons are also defined for muons, with the *LooseTrackOnly* working point having a 99% efficiency [151].

### 3.3.7. Missing transverse momentum

The missing transverse momentum, $p_T^{miss}$, is defined as the vector momentum imbalance in the transverse plane, obtained from the negative vector sum of the momenta of all visible particles in the event. The $p_T^{miss}$ reconstruction [152] uses tracks from the ID, energy deposits from the calorimeter and muons reconstructed in the MS. Calorimeter energy deposits are associated with a calibrated high-$p_T$ object in a specific order: electrons, photons, hadronically decaying tau leptons, jets and muons. The $p_{x(y)}^{miss}$ components are calculated as follows:

$$p_{x(y)}^{miss} = p_{x(y)}^{miss,e} + p_{x(y)}^{miss,\gamma} + p_{x(y)}^{miss,\tau} + p_{x(y)}^{miss,jets} + p_{x(y)}^{miss,\mu} + p_{x(y)}^{miss,soft} \tag{3.4}$$

where each term is calculated as the negative vectorial sum of the momenta of the calibrated reconstructed objects and $p_T^{miss} = \sqrt{(p_x^{miss})^2 + (p_y^{miss})^2}$. The soft term, $p_{x(y)}^{miss,soft}$, is calculated from ID tracks (track-based soft term) not associated with reconstructed objects. Photons are not considered in this thesis and are treated as jets in the $p_T^{miss}$ calculation.

# Chapter 4.

# Development and performance of jet triggers

Jet triggers are crucial for selecting events with high-$p_T$ jets for detector performance studies and physics measurements. The jet trigger menu consists of single-jet triggers, multi-jet triggers, $H_{\mathrm{T}}$ (scalar sum of jet transverse energies) triggers and analysis-specific triggers. Single-jet triggers select events with at least one jet above a given transverse energy threshold, multi-jet triggers select events with at least $N$ jets above a given transverse energy threshold, and $H_{\mathrm{T}}$ triggers select events with the scalar sum of the transverse energies of all jets in the event, $H_{\mathrm{T}}$, above a given threshold. Single-jet and multi-jet triggers can be used for precision measurements of inclusive jet [153], di-jet [154] and multi-jet topologies [155], or for searches for physics beyond the SM, such as high-mass di-jet resonances [112, 156] or SUSY [157]. Studies for jet calibration, such as the $\eta$-intercalibration, also use single-jet triggers. Analysis specific triggers include combinations of jet triggers and other types of triggers, such as photon or $p_{\mathrm{T}}^{\mathrm{miss}}$ triggers.

The remainder of this Chapter describes the development and performance of jet triggers in 2015. The development of jet triggers for Run-2 data taking is described in Section 4.1. A new jet trigger validation package used to validate the new jet triggers during the development phase, before the data-taking, is described in Section 4.2. Finally, the performance of jet triggers using the full 2015 dataset is shown in Section 4.3.

## 4.1. Development of jet triggers for Run-2

### 4.1.1. The Run-1 trigger system

ATLAS used a three-level trigger system in Run-1, in which the HLT consisted of two distinct levels, Level 2 (L2) and the Event Filter (EF). The L2 trigger was seeded by the L1

RoIs and the EF trigger was seeded by the L2 output and used offline analysis procedures on fully reconstructed events to further reduce the event rate. Jet triggers were seeded by either a special random L1 trigger that randomly accepts events, or an L1 jet trigger [158]. The random trigger was typically used for triggers that select events with offline jet $E_{\mathrm{T}} >$ 45 GeV to avoid inefficiencies introduced by L1 for low-$p_{\mathrm{T}}$ jets.

The L1 jet triggers did not use the full granularity of the calorimeter and their decision was based on the information from analogue sums of calorimeter cells within projective regions, called trigger towers. The size of the trigger towers was approximately $\Delta\eta \times \Delta\phi = 0.1 \times 0.1$ in the central part of the calorimeter, with $|\eta| < 2.5$, and were larger and less regular in the forward region. Electromagnetic and hadronic calorimeters had separate trigger towers and the total number of trigger towers was 7168. Jet candidates were identified using jet elements, which are $2 \times 2$ sums of trigger towers. A sliding window algorithm [146] was used to search for local energy maxima across groups of jet elements and tested these maxima against pre-defined thresholds.

The L2 jet triggers reconstructed jets using a simple cone algorithm seeded by the L1 RoIs. The cone algorithm iterated over cells in a relatively large RoI of size $\Delta\eta \times \Delta\phi = 1.0 \times 1.0$. The EF jets were independent of any jets found by L1 or L2. An unseeded anti-$k_T$ jet algorithm was run over topo-clusters formed from calorimeter cells. These jets, referred to as trigger jets, were different from offline jets resulting in inefficiencies due to online-offline selection criteria. In addition, having two distinct HLT levels increased the network and CPU usage.

### 4.1.2. The updated Run-2 trigger system

The ATLAS trigger system has been updated for Run-2 with L2 and EF merged into the HLT. The jet triggers have been rewritten and the HLT is now using offline jets instead of the trigger jets [159] used in Run-1. The description of the L1 jet triggers for Run-1 in the previous Section is also valid for Run-2. The default jet trigger chain for Run-2 with the sequence of algorithms and the features/collections passed to and from each algorithm is shown in Figure 4.1. A chain is a list of HLT sequences, data structures consisting of an ordered list of algorithms and an L1 seeding trigger. The sequences typically contain a number of feature extraction (FEX) algorithms used to extract features from the data, such as topo-cluster or jet collections, and a hypothesis (Hypo) algorithm that decides if an event passes the chain. Information is passed between trigger algorithms using a token known as the trigger element. The trigger menu creates the chain and configures all the algorithms based on the name of the trigger, which is used to deduce the $E_{\mathrm{T}}$ threshold and $\eta$ range.
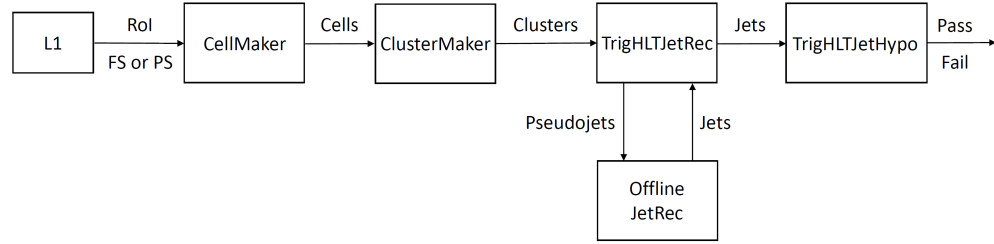
**Figure 4.1.** Jet trigger chain for Run-2 showing the sequence of algorithms and the features/collections passed to and from each algorithm.

If a high-$p_T$ jet is found by the L1 seeding trigger, it creates an RoI and sends that to the HLT. No information is sent to the HLT if no L1 jets pass the L1 trigger thresholds. The CellMaker algorithm takes the L1 RoI as input and creates a collection of the calorimeter cells within the RoI. The ClusterMaker algorithm then takes the cells as input and creates a collection of topo-clusters. The offline jet reconstruction (JetRec) algorithm is used to reconstruct and calibrate both offline and HLT jets. It retrieves a collection of pseudojets from StoreGate [160] and reconstructs the jets from pseudojets. A pseudojet is a FastJet [161] four-vector object created from each calorimeter cluster or other input. Jet triggers use trigger elements to pass information between algorithms and do not use StoreGate, requiring a new algorithm, TrigHLTJetRec, used to retrieve the pseudojets from the trigger element and pass them to the offline JetRec. TrigHLTJetRec uses the topo-clusters and the offline JetRec algorithm to create a jet collection. The reconstructed jets are then passed to the TrigHLTJetHypo algorithm which tests if they pass the predefined $E_T$ thresholds and $\eta$ range of each jet trigger in the menu. The output of TrigHLTJetHypo is a pass or fail decision for each event.

### 4.1.3. The jet trigger reconstruction package

TrigHLTJetRec is a FEX algorithm with one input and one output trigger element. It retrieves a cluster collection from the trigger element and creates a pseudojet from each cluster. Topo-clusters either at EM scale or calibrated using LCW are the default inputs, but it is also possible to create pseudojets from L1 trigger towers or even jets for reclustered jet definitions. A pseudojet collection is passed to the offline JetRec which reconstructs the jets and returns them in a jet collection. TrigHLTJetRec configures the offline JetRec algorithm to use the appropriate settings depending on the input used to make the pseudojets, and also apply the correct HLT jet calibration. TrigHLTJetRec then attaches the jet collection to the output trigger element to be used by other algorithms such as the jet hypothesis testing algorithm, TrigHLTJetHypo.

The HLT jets are independent of any jets found by the L1 triggers. Similar to offline jets, the anti-$k_t$ jet algorithm is run over topo-clusters formed from calorimeter cells to create HLT jets, which are then calibrated. The HLT jet calibration only applies the two most important steps of the offline calibration, the pileup subtraction and the JES correction. The origin and residual corrections and also parts of the GSC require tracking information which is unavailable to the HLT. The HLT jet calibration can be applied in four ways: no jet calibration, pileup subtraction only, JES correction only, or both pileup subtraction and JES corrections (default). The inputs to the jet algorithm can be topo-clusters at the EM scale (default), topo-clusters calibrated using LCW, and L1 trigger towers (L1.5). The jet reconstruction can be run twice to produce reclustered jets [162], in which small-$R$ jets ($R$ = 0.4) are used as input to make large-$R$ jets ($R = 1.0$). Jet triggers apply kinematic cuts on the $E_T$ and $\eta$ range of reconstructed jets. Central jet triggers require jets to be within $|\eta| < 3.2$ and forward jet triggers require jets in the interval $3.2 < |\eta| < 4.9$.

### 4.1.4.  Configuration of jet triggers

The jet trigger menu controls the configuration of all jet trigger chains. The name of each trigger contains information about the different parameters used to define each algorithm and each parameter can be configured from the menu. The naming convention for L1 jet triggers is `L1_[trigger type][threshold]_[η range]`, where the trigger type is 'J' for single-jet triggers or 'XJ' for multi-jet triggers with X being the jet multiplicity, the threshold is given in GeV and the $\eta$ range is $|\eta| < 3.1$ for central L1 jet triggers and $3.1 < |\eta| < 4.9$ for forward L1 jet triggers. The $\eta$ range for central jet L1 triggers is the default value and is not shown in the name. For example, `L1_J15` is a single-jet L1 trigger with an $E_T$ threshold of 15 GeV, `L1_J50_31ETA49` is a single-jet forward L1 trigger with an $E_T$ threshold of 50 GeV, and `L1_3J40` is a multi-jet L1 trigger requiring three central jets to pass the $E_T$ threshold of 40 GeV.

The HLT jet trigger naming convention is more complicated and is summarised by
`HLT_[trigger type][threshold]_[η range]_[jet algorithm]_[constituent type]_[constituent energy scale]_[jet energy scale]_[calorimeter readout]`

The trigger type is typically 'j' for single-jet triggers or 'Xj' for multi-jet triggers where X is the jet multiplicity, but it can also be 'ht' for the specialised $H_T$ triggers. The threshold is given in GeV and the options for the remaining terms are shown in Table 4.1. Jet triggers typically use "full scan" (FS), in which the RoI is defined as the whole calorimeter. It is also possible to use "partial scan" (PS) [163], in which the RoI is only part of the calorimeter. The names of jet triggers only include non-default parameters, for example

HLT_j110 is a single-jet HLT trigger with an $E_T$ threshold of 110 GeV using the default options `0eta320_a4_tc_em_subjes_FS`.

| Parameter | Values | Description | Default |
|---|---|---|---|
| **pseudorapidity ($\eta$) range** | 0eta320 | jets in interval $0 < |\eta| < 3.2$ | Default |
| | 0eta240 | jets in $0 < |\eta| < 2.4$ (inner detector acceptance) | – |
| | 240eta320 | jets in $2.4 < |\eta| < 3.2$ | – |
| | 0eta490 | jets in $0 < |\eta| < 4.9$ (full calorimeter) | – |
| | 320eta490 | jets in $3.2 < |\eta| < 4.9$ (forward jets) | – |
| **jet algorithm** | a4 | anti-$k_t$ with $R = 0.4$ | Default |
| | a10 | anti-$k_t$ with $R = 1.0$ | – |
| | a10r | anti-$k_t$ with $R = 1.0$ using reclustered $R = 0.4$ jets | – |
| **constituent type** | tc | topo-clusters reconstructed from calorimeter cells | Default |
| | TT | L1 TriggerTowers used as jet input in HLT (L1.5) | – |
| **constituent energy scale** | em | no weights applied | Default |
| | lcw | local cluster weighting | – |
| | had | for future use (e.g. calibrated TriggerTower inputs) | – |
| **jet energy scale** | jes | JES calibration factors without pileup subtraction | – |
| | sub | pileup subtraction applied but no JES factors | – |
| | subjes | both pileup subtraction and JES factors | Default |
| | nojcalib | no jet-level calibrations or corrections at all | – |
| **calorimeter readout** | FS | Full Scan, not based on RoIs | Default |
| | PS | Partial Scan using RoIs / super-RoIs | – |

**Table 4.1.** Jet trigger naming convention for Run-2. The default option listed for each parameter applies unless otherwise specified. The default jet triggers in Run-2 are constructed using `a4tcemsubjesFS` jets. For reclustered jet definitions (`a10r`) the default calibration state is used for the input $R = 0.4$ anti-$k_t$ jets. [164]

## 4.1.5. Diagnostic algorithms

Every time a trigger job is run, several monitoring histograms are automatically created and stored in a single output file. However, although these histograms provide useful information such as how many events passed each trigger, they are not appropriate for a full set of diagnostics during the development stage. It is crucial to ensure jet triggers work as intended, otherwise data collected by them cannot be used.

New diagnostic algorithms were developed for each part of the jet trigger chain to easily identify problems in the code during the early stages of development. Five new diagnostic algorithms were created as part of the TrigHLTJetRec package as shown in Figure 4.2. The RoI Diagnostics simply prints information about the L1 RoI. If FS is used, then it prints 'z: 0 +/- 225 eta: 0 +/- 5 phi: 0 +/- 3.14159 RoIid: 0 RoIword: 0 fullscan 1'. The
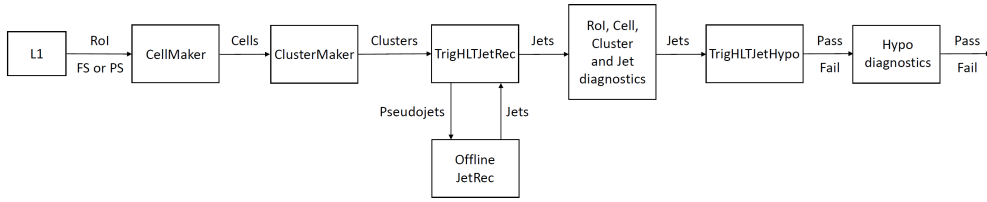
**Figure 4.2.** Jet trigger chain with the diagnostic algorithms. The RoI, Cell, Cluster and Jet
diagnostics have to be executed before the TrigHLTJetHypo, otherwise only events
that pass the chain will be used to fill the histograms.

Cell diagnostics algorithm makes plots of cell attributes, such as number of cells, energy,
$\eta$, and $\phi$. Similarly, the Cluster diagnostics algorithm makes plots of cluster attributes.
The Jet diagnostics algorithm is used to ensure correct reconstruction of jets by plotting
attributes of all reconstructed jets, such as number of jets, $E_T$, $p_T$, and $\eta$. In addition, $E_T$
and $p_T$ plots of the leading jet are also created. Finally, the Hypo diagnostics algorithm
is used to check the TrigHLTJetHypo algorithm by plotting attributes of jets passing the
requirements of the trigger, particularly the $E_T$ and $\eta$ criteria.

The diagnostic algorithms retrieve the RoI, cell, cluster and jet containers from the
input trigger element. They do not interfere with the internal coding of other algorithms,
do not alter the trigger element, and can be easily added or removed from the sequence by
changing the menu configuration. Unlike the monitoring histograms, that create one file
and combine entries if more than one trigger is used, the diagnostics tools create four files
containing the cell, cluster, jet and jet hypo histograms for each trigger used. Each file is
independent and no entries are combined when using multiple triggers.

Diagnostic plots were created using 1 000 events of a $t\bar{t}$ MC validation sample using the
`HLT_j110` single jet trigger as an example. Figure 4.3 shows the number of cells, clusters, all
jets and jets that pass the TrigHLTJetHypo algorithm for each event. All entries in the cell
histogram have the same value of 187 724 [165] since FS was used and the RoI is the whole
calorimeter for every event. Figure 4.4 shows the distributions of cells, clusters, all jets, and
jets that pass the TrigHLTJetHypo algorithm for each event as a function of $\eta$ and $\phi$. The
number of cells is larger in the central regions, which reflects the structure of the calorimeter.
The distribution of clusters indicates a potential problem with a larger number of clusters
in the region $1.7 < |\eta| < 3.5$ that also appears in the distribution of all jets. The input file
is a validation sample and problems are expected, but this distribution shows the usefulness
of the diagnostic algorithms. Figure 4.5 shows the distribution of cells, clusters, all jets and
jets that pass the TrigHLTJetHypo algorithm for each event as a function of energy. Cells
can have negative energy due to noisy cells or cells integrating energy from more than one
proton-proton collision. This can also lead to clusters with some negative energy. Most jets
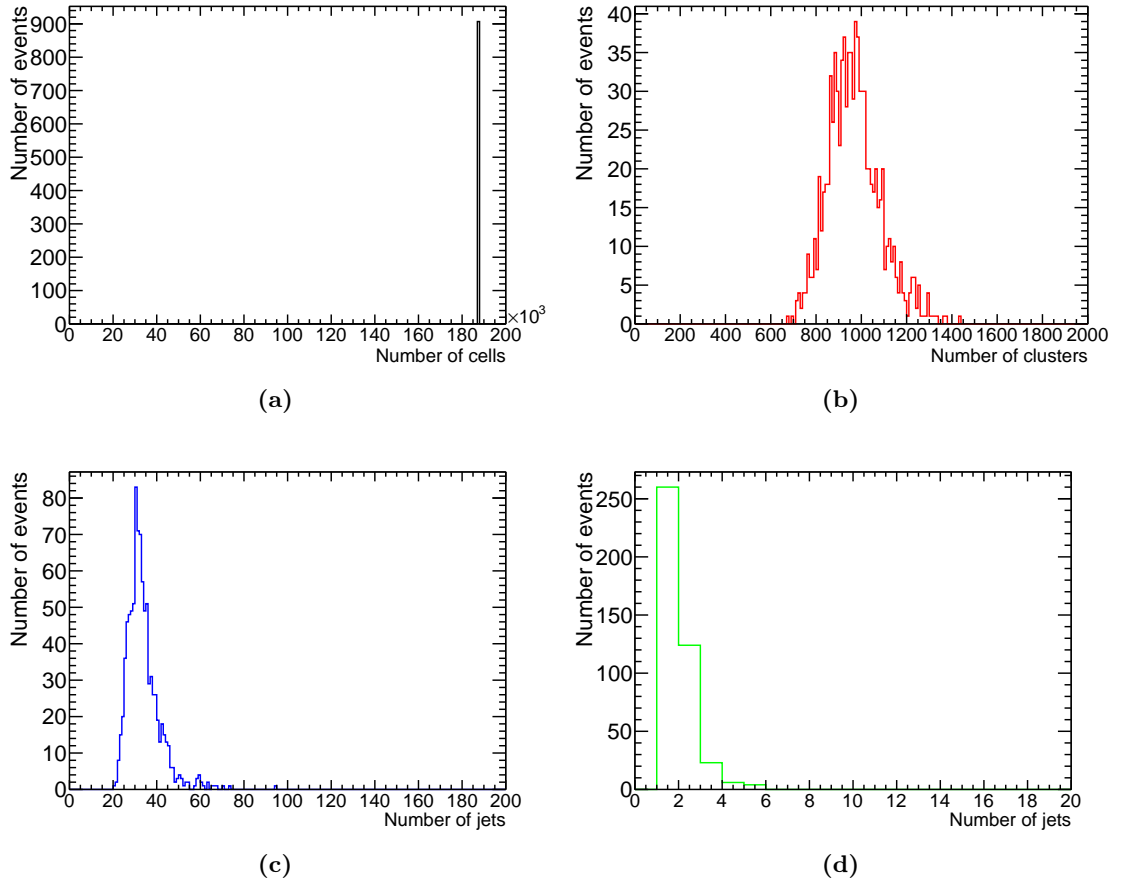
**Figure 4.3.** Number of events with a given number of (a) cells, (b) clusters, (c) all jets and (d) jets that pass the TrigHLTJetHypo algorithm, using the `HLT_j110` trigger.

appear to have very low $p_{\mathrm{T}}$ and are rejected by the TrigHLTJetHypo algorithm. Figure 4.6 shows the $E_{\mathrm{T}}$ of all leading jets and leading jets that pass the TrigHLTJetHypo algorithm. The leading jet is defined as the jet with the highest $p_{\mathrm{T}}$ in the event. Only jets with $E_{\mathrm{T}} >$ 110 GeV and $|\eta| < 3.2$ pass the TrigHLTJetHypo algorithm. There are no jets with $E_{\mathrm{T}} <$ 110 GeV in Figure 4.6b as expected.

**Figure 4.4.** Distributions of (a) cells, (b) clusters, (c) all jets and (d) jets that pass TrigHLT-JetHypo for each event, as a function of $\eta$ and $\phi$, using the `HLT_j110`trigger.

**(a)**
**(b)**
**(c)**
**(d)**

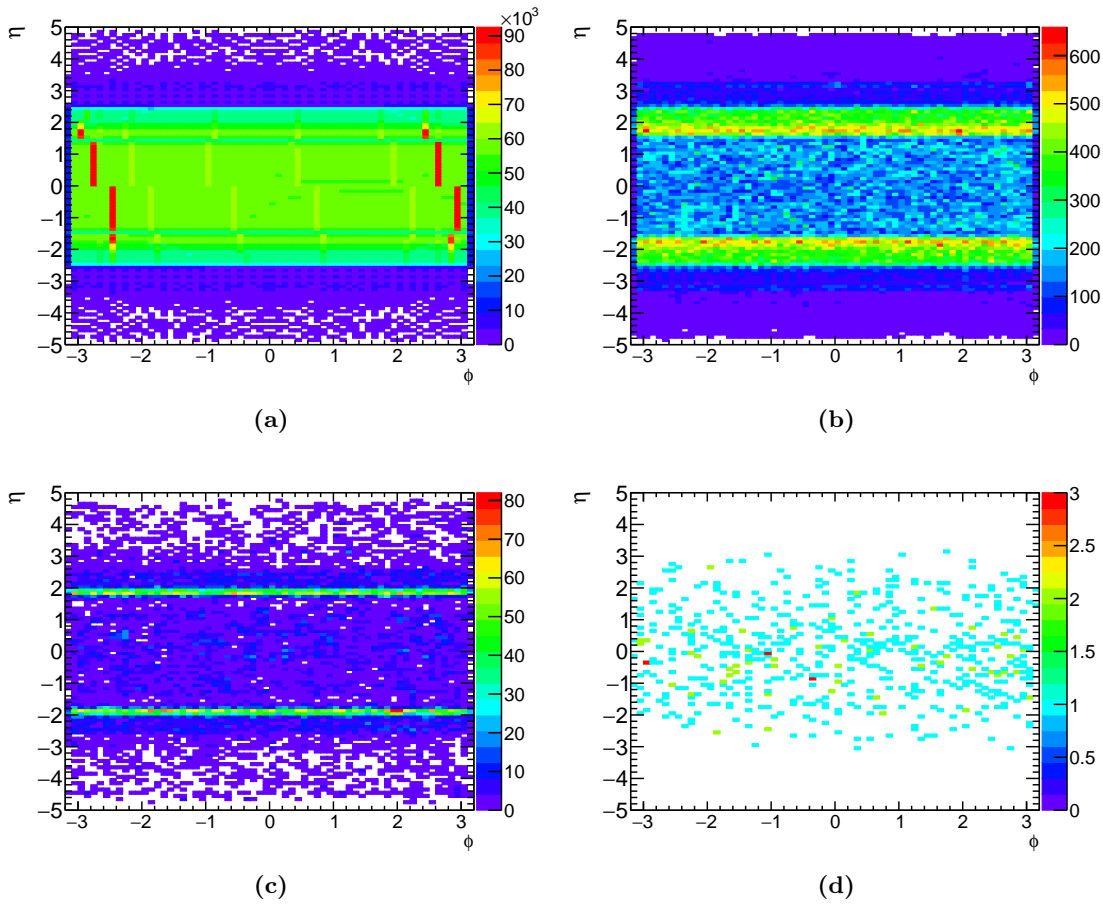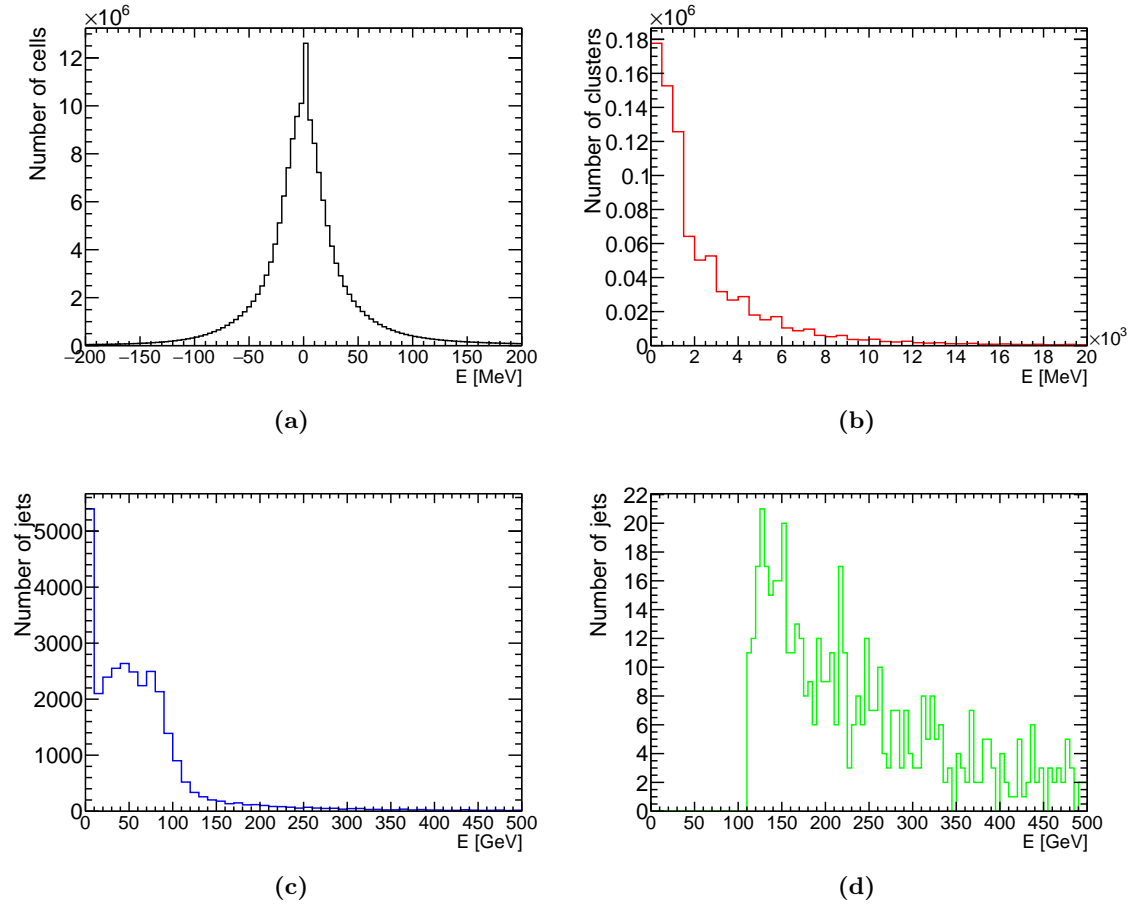**Figure 4.5.** Distributions of (a) cells, (b) clusters, (c) all jets and (d) jets that pass TrigHLT-JetHypo for each event, as a function of energy, using the `HLT_j110`trigger.
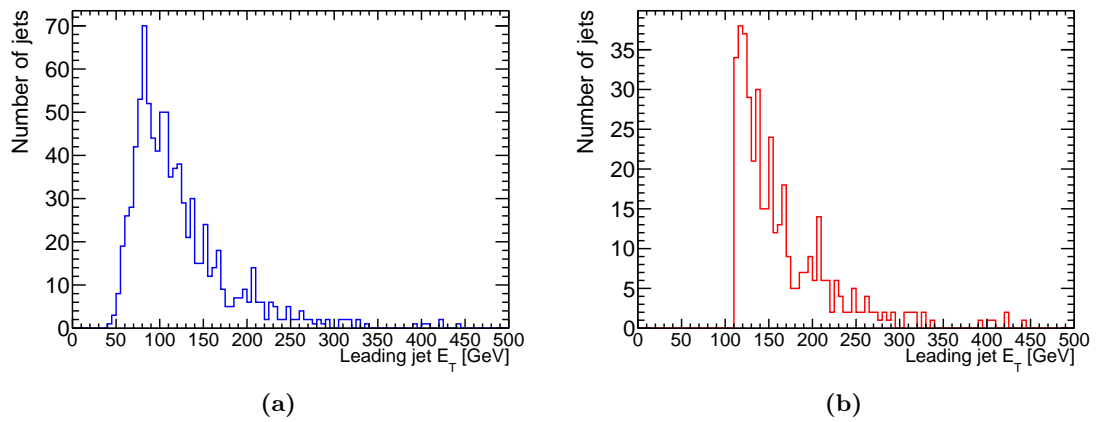


**(a)**
**(b)**

**Figure 4.6.** Distributions of (a) leading jets and (b) leading jets that pass TrigHLTJetHypo for each event, as a function of $E_T$, using the `HLT_j110` trigger.

## 4.2. Jet trigger validation package

The RunTimeTester (RTT) [166] is a Python framework used to validate ATLAS software [167]. It is run several times per day processing the latest ATLAS software release. It provides a tool for automating setting up and running of developer jobs and presenting results on a webpage [168]. The RTT is used for computationally long tests, up to 24 hours, and can detect rare software issues.

A new jet trigger validation software package, TrigJetValidation, has been developed to automate the validation process. TrigJetValidation runs the jet part of the generic trigger validation test, which creates two output text files with the number of events passing each chain or the trigger element. Post-processing tests are used to compare these two files to "reference" files and check if the counts have changed. The reference files are the output of the previous stable version. If a single entry in each file has changed, or a new chain has been added or removed from the jet trigger menu, the tests will fail.

The diagnostic algorithms have been added to TrigJetValidation. All the individual files for each chain are combined into a single diagnostics output file and the individual files are deleted. All chains have four different directories in that file, with histograms of cells, clusters, all jets, and jets passing TrigHLTJetHypo. Plotting macros can also be run on the diagnostics file to save individual histograms as images or plot multiple distributions on the same histogram. A macro that plots the $p_T$ and $E_T$ distributions of all jets of two chains, HLT_j85 and HLT_j175, with different calibrations on the same plot has been added to TrigJetValidation. The macro can be easily updated to include more chains or plot additional quantities.

The tests that compare the number of events passing each chains to a reference file are very useful to automatically identify changes in the trigger code, but they cannot identify which part of the jet trigger code has changed. Other than a chain being added or removed from the menu, the number of events could change due to code changes in the CellMaker, ClusterMaker or TrigHLTJetRec algorithms. Since the diagnostics file contains histograms for all chains, a new test was developed to extract the mean number of cells and the mean cell energy of each chain and store them in a text file. Another test extracts the mean number of clusters and mean cluster $E_T$ for each chain. The final validation tests compare these two files to reference files and fail if any numbers are different from the reference files. An example of these text files and a screenshot of the RTT results comparing them to the reference files is shown in Figure 4.7. In this case both tests have failed since both text files have different numbers, indicating a change in the CellMaker code and possibly the ClusterMaker code as well. The diagnostic tests were routinely used for early validation of the Run-2 jet trigger software in 2015.

**(a)**



**(b)**

**Figure 4.7.** (a) Example text files with only the first few jet chains in the menu showing the mean number of cells and clusters and the mean number of cell energy or cluster $E_{\mathrm{T}}$ for each trigger, and (b) failed RTT tests comparing the text files to the reference files.

## 4.3. Performance of jet triggers in 2015

The results presented here have been published in Ref [128].

### 4.3.1. Menu setup

The lowest unprescaled single-jet trigger in 2015 is `HLT_j360`, seeded by `L1_J100`, and has a rate of 18 Hz. The lowest unprescaled multi-jet triggers are `HLT_3j175`, `HLT_4j85`, `HLT_5j60` and `HLT_6j45`, with rates of 6, 20, 15 and 12 Hz respectively. The lowest unprescaled $H_{\mathrm{T}}$ trigger is `HLT_ht850` with a rate of 12 Hz, requiring at least one jet with $E_{\mathrm{T}} > 100$ GeV and $H_{\mathrm{T}} > 850$ GeV. A set of lower-threshold single-jet triggers between 15 and 360 GeV are prescaled to approximately 1 Hz each. The lowest-threshold single-jet trigger is `HLT_j15`, seeded by a random trigger at L1.

### 4.3.2. Jet trigger efficiencies

The performance of jet triggers is evaluated by calculating per-event efficiencies as a function of the $p_{\mathrm{T}}$ of an offline jet in the event, leading jets for single-jet triggers, and $N^{th}$ jet for $NjX$ multi-jet triggers. The per-event efficiency of a jet trigger is defined as:

$$\varepsilon_{\mathrm{trig}}^{\mathrm{jet}} = \frac{N_{\mathrm{events,\ pass\ trig\ and\ ref\ trig}}^{\geq 1\ \mathrm{jet}}}{N_{\mathrm{events,\ pass\ ref\ trig}}^{\geq 1\ \mathrm{jet}}} \tag{4.1}$$

where $N^{\geq 1 \text{ jet}}_{\text{events, pass ref trig}}$ is the number of events with at least one offline jet that passed the "reference" trigger, and $N^{\geq 1 \text{ jet}}_{\text{events, pass trig and ref trig}}$ is the number of events with at least one offline jet that also passed the trigger of interest, in addition to the reference trigger. Events in data are only recorded if they pass a trigger from the menu, so the denominator of the efficiency can be biased if all recorded data are used. For example, the distribution of the $p_{\text{T}}$ of the leading offline jet in 2015 data has a peak around 400 GeV, due to `HLT_j360` being the lowest unprescaled single-jet trigger. The bootstrap method is used to calculate jet trigger efficiencies in data, where the efficiency of a higher threshold trigger is determined using events passing a lower threshold trigger, referred to as the reference trigger. The reference trigger must be fully efficient before the turn-on region of the trigger of interest, otherwise it will bias the efficiency.

| L1 trigger | L1 reference trigger | HLT trigger | HLT reference trigger |
|:---:|:---:|:---:|:---:|
| L1_J20 | HLT_j25 | HLT_j25 | HLT_j15 |
| L1_J50 | HLT_j60 | HLT_j60 | HLT_j25 |
| L1_J75 | HLT_j60 | HLT_j175 | HLT_j110 |
| L1_J100 | HLT_j85 | HLT_j360 | HLT_j260 |
| L1_J20_31ETA49 | HLT_j15_320eta490 | HLT_j25_320eta490 | HLT_j15_320eta490 |
| L1_J50_31ETA49 | HLT_j45_320eta490 | HLT_j60_320eta490 | HLT_j25_320eta490 |
| L1_J75_31ETA49 | HLT_j60_320eta490 | HLT_j110_320eta490 | HLT_j85_320eta490 |
| L1_J100_31ETA49 | HLT_j85_320eta490 | HLT_j175_320eta490 | HLT_j110_320eta490 |
| L1_3J15 | HLT_j45 | HLT_4j45 | HLT_j85 |
| L1_3J40 | HLT_j60 | HLT_4j85 | HLT_j60 |
| L1_4J15 | HLT_j45 | HLT_5j45 | HLT_j60 |
| L1_4J20 | HLT_j45 | HLT_5j85 | HLT_j85 |

**Table 4.2.** Jet triggers and reference triggers. Other reference triggers can be used, provided they are fully efficient before the turn-on region of the trigger of interest.

Example reference triggers for a selection of single-jet and multi-jet L1 and HLT triggers are shown in Table 4.2. HLT triggers can be used as reference triggers for L1 triggers if their L1 seed is not the same as the trigger of interest. In addition to lower threshold multi-jet triggers, single-jet triggers can be used as reference triggers for multi-jet triggers, as long as the threshold is large enough to include additional high-$p_{\text{T}}$ jets that will pass the trigger requirements. Prescales can introduce artificial inefficiencies since they are usually different between the trigger of interest and the reference trigger. Because of this, the actual decision of the trigger is not used and instead the trigger is emulated when calculating the efficiencies. The HLT jets are stored for every event, irrespective of which

trigger has passed, so the decision of any trigger can be emulated by applying the $E_T$ and $\eta$ requirements on the HLT jet collection to check if any of those jets would pass the trigger of interest. The L1 seed decision can also be emulated from the stored L1 jets, and both the emulated HLT and L1 decisions must pass for the emulated trigger decision.

Jet trigger efficiencies are calculated using the full 2015 data with a total integrated luminosity of 3.2 fb$^{-1}$. Reference samples are selected using the triggers specified in Table 4.2 and only good quality data are considered, obtained when the detector was fully operational. Each event is required to have a primary vertex with at least two associated tracks.

Trigger efficiencies are presented as a function of the offline jet kinematics. Offline jets are reconstructed from topo-clusters calibrated at the EM scale using the anti-$k_t$ jet algorithm with a radius parameter of $R = 0.4$. They required to have $p_T > 7$ GeV and $|\eta| < 4.5$. Pileup jets are rejected by requiring offline jets with $20 < p_T < 50$ GeV and $|\eta| < 2.4$ to satisfy JVT $> 0.64$. Events containing bad quality offline jets with $p_T > 20$ GeV and $|\eta| < 4.5$ are rejected using the LooseBad criteria, in order to suppress non-collision backgrounds and calorimeter noise. An additional strict requirement on jet timing $< 10$ ns has been included for offline jets to ensure that the jets are in the correct bunch crossing. This is important because L1 jets are identified with a specific bunch crossing.

Multi-jet processes are generated using PYTHIA v8.186. The A14 tune [169] is used together with the NNPDF2.3lo PDF set [72]. The samples are passed through GEANT4 [170, 171] for a full simulation [172] of the ATLAS detector and are then reconstructed using the same analysis chain as the data. Pileup interactions are simulated with PYTHIA v8.186 using the A2 parton shower tune [173] and the MSTW2008lo PDF set [174].

Two-dimensional per-jet single-jet trigger efficiencies as a function of $\eta$ and $\phi$ are shown in Figure 4.8. These efficiencies have been calculated using a special run in early 2015 when most jet triggers were running unprescaled, using only 89 nb$^{-1}$ of data and a bunch spacing of 50 ns. The selected jet $p_T$ threshold is below the fully efficient point of the triggers in order to show the spatial dependence. Inefficiencies are observed in both central and forward triggers near the $|\eta| = 3.2$ boundary, due to differences in calibration between HLT and offline jets. HLT central jets with $|\eta|$ slightly less than 3.2 could be reconstructed as forward offline jets with $|\eta|$ above 3.2, and vice versa.

Figure 4.9 shows comparisons of L1 central and L1 forward per-event single-jet trigger efficiencies. The geometrical and algorithmic differences between L1 and offline procedures cause a broad turn-on. The $\eta$ ranges of the offline jets are chosen to ensure that the leading jet is fully constrained within the respective trigger central or forward regions. HLT central and forward per-event single-jet trigger efficiencies are shown in Figure 4.10. Steeper turn-on than L1 is observed due to use of the same jet algorithm for HLT and offline jets.
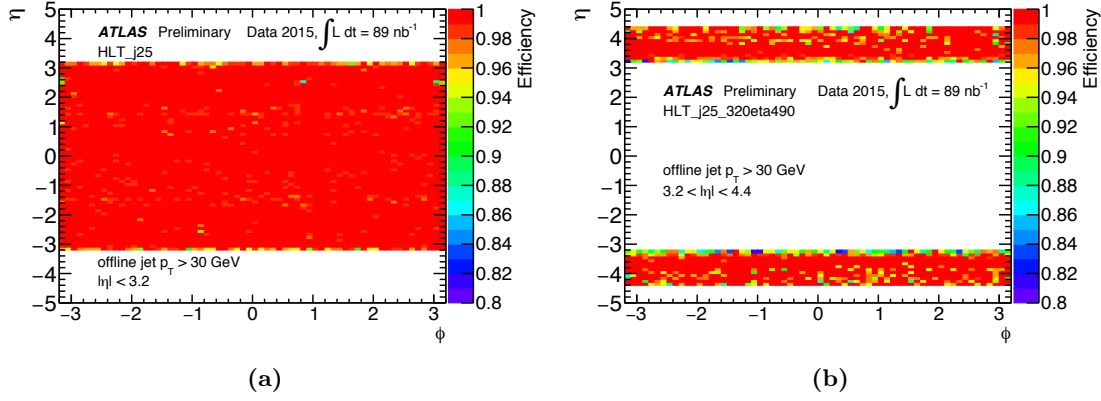
**Figure 4.8.** Comparison of (a) `HLT_j25` central ($|\eta| < 3.2$) and (b) `HLT_j25_320eta490` forward ($3.2 < |\eta| < 4.4$) per-jet single-jet trigger efficiency as a function of $\eta$ and $\phi$.
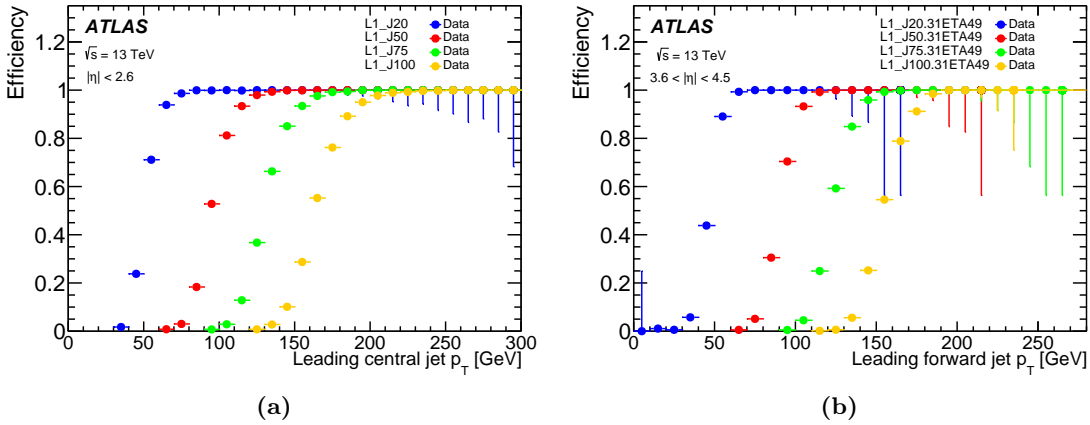


**Figure 4.9.** Comparison of (a) L1 central ($|\eta| < 2.6$) and (b) forward ($3.6 < |\eta| < 4.5$) per-event single-jet trigger efficiencies. The geometrical and algorithmic differences between L1 and offline procedures cause broad turn-ons.

Furthermore, good agreement is also seen between data and simulation. Figure 4.11 shows comparisons of per-event isolated L1 and HLT multi-jet trigger efficiencies. Isolation is enforced by requiring each of the $N$ leading jets to be isolated by $\Delta R > 0.6$ from all other reconstructed offline jets with $p_\mathrm{T} > 20$ GeV. The efficiencies of `HLT_4j45` and `HLT_5j45` are very similar, so differences in offline and HLT jets do not depend on the number of jets and the performance of any multi-jet trigger can be reliably predicted.

Efficiencies are calculated using combinations of central and forward single-jet HLT triggers for the di-jet $\eta$-intercalibration [143], which requires both forward and central jets. The efficiencies are first calculated as a function of the average $p_\mathrm{T}$ of the two leading jets and the fully efficient point is determined from the plots. Efficiencies are then calculated as

**(a)**　　　　　　　　　　　　　　**(b)**
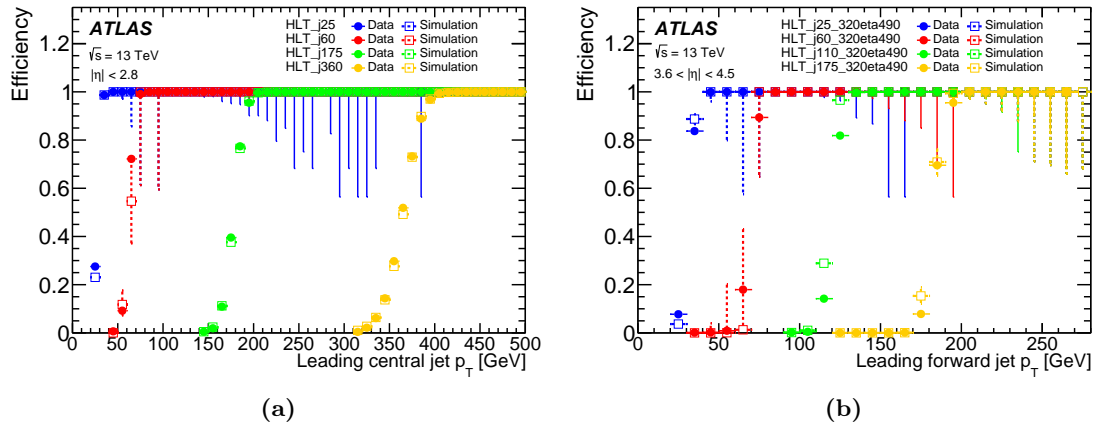
**Figure 4.10.** Comparison of (a) HLT central ($|\eta| < 2.8$) and (b) forward ($3.6 < |\eta| < 4.5$) per-event single-jet trigger efficiency turn-on curves. Steeper turn-on than L1 is observed and good agreement between data and simulation.



**(a)**　　　　　　　　　　　　　　**(b)**
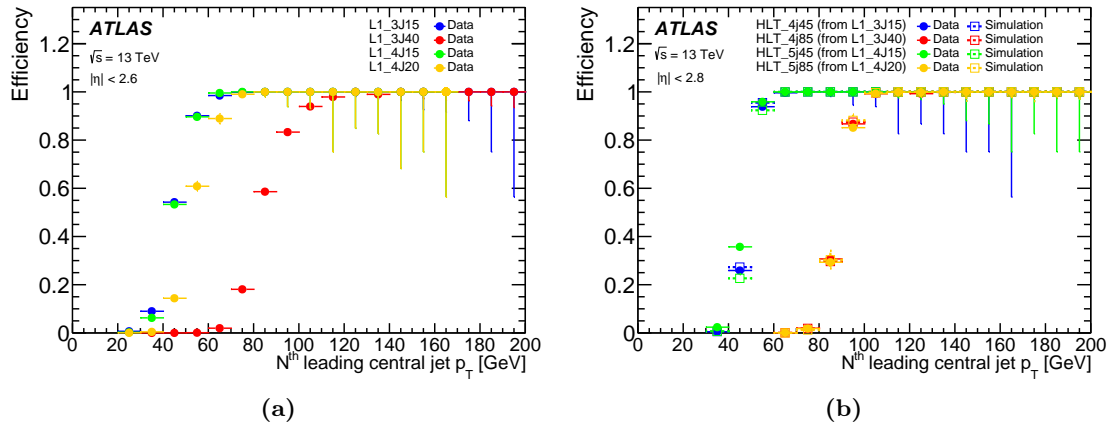
**Figure 4.11.** Comparison of per-event isolated (a) L1 and (b) HLT multi-jet trigger efficiency turn-on curves. Isolation is enforced by requiring each of the $N$ leading jets to be isolated by $\Delta R > 0.6$ from all other reconstructed offline jets with $p_\mathrm{T} > 20$ GeV.

a function of the $\eta$ of the most forward of the two leading jets, for events with average $p_\mathrm{T}$ above the fully efficient point of the trigger combination of interest, and examples for a selection of triggers are shown in Figure 4.12. The combination of the central and forward triggers is fully efficient across $\eta$, whereas the individual central or forward triggers are not.
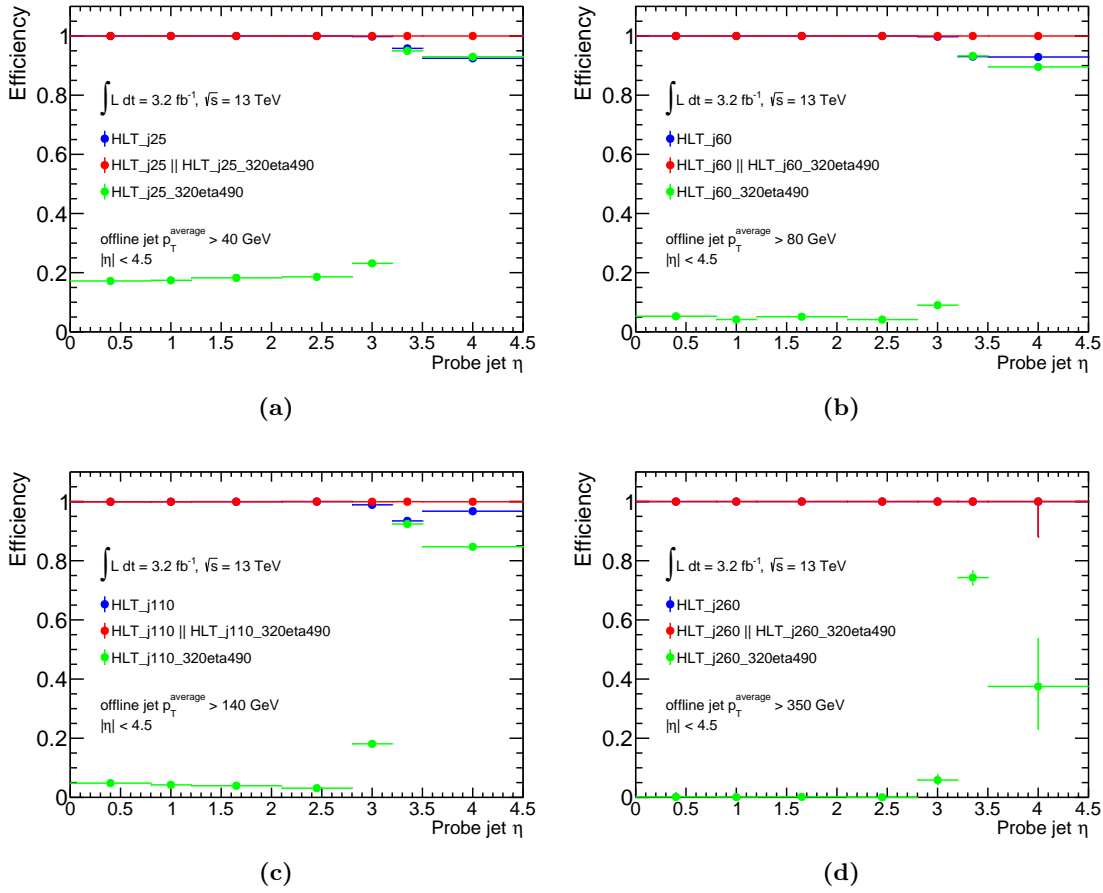
**Figure 4.12.** Efficiencies of combinations of central and forward single-jet HLT triggers as a function of the $\eta$ of the most forward of the two leading jets (a) `HLT_j25`, (b) `HLT_j60`, (c) `HLT_j110`, and (d) `HLT_j260`. The average $p_T$ of the two leading jets must be greater than the fully efficient point of the trigger combination. The combination of the central and forward triggers is fully efficient across $\eta$, whereas the individual central or forward triggers are not.

# Chapter 5.

# Search for dark matter

This Chapter presents a novel measurement of detector-corrected observables using ratio measurements to search for DM. The results from the work presented here have been published in Ref [175].

## 5.1. The $R^{\mathrm{miss}}$ observable

Missing transverse momentum is the experimental signature of DM at the LHC and jets are the most common high-$p_{\mathrm{T}}$ objects, making searches in $p_{\mathrm{T}}^{\mathrm{miss}}$ + jets events particularly appealing. Example Feynman diagrams for WIMP pair production in association with one jet, and via VBF production are shown in Figure 5.1, including the SM processes with the same experimental signature due to the $Z \to \nu\bar{\nu}$ decay.

In this analysis, a new variable sensitive to DM production is defined by

$$R^{\mathrm{miss}} = \frac{\sigma_{\mathrm{fid}}\left(p_{\mathrm{T}}^{\mathrm{miss}} + \mathrm{jets}\right)}{\sigma_{\mathrm{fid}}\left(\ell^+\ell^- + \mathrm{jets}\right)} \tag{5.1}$$

where $\sigma_{\mathrm{fid}}\left(p_{\mathrm{T}}^{\mathrm{miss}} + \mathrm{jets}\right)$ is the fiducial cross-section for the production of events with $p_{\mathrm{T}}^{\mathrm{miss}}$ in association with jets, corresponding to the inclusive $Z \to \nu\bar{\nu}$ + jets production in the absence of BSM events. The $\sigma_{\mathrm{fid}}\left(\ell^+\ell^- + \mathrm{jets}\right)$ is the fiducial cross-section for the inclusive production of events with $\ell^+\ell^-$ in association with jets, consistent with the decay of a $Z/\gamma^*$ boson to an oppositely charged same-flavour lepton pair. The denominator includes events in which the mediator is a virtual photon in the $\ell^+\ell^-$ + jets measurement, however this contribution can be reduced by requiring the dilepton invariant mass to be close to the mass of the $Z$ boson. Only electron and muon pairs are considered since events with tau lepton pairs are experimentally more challenging to identify. The value of $R^{\mathrm{miss}}$ predicted
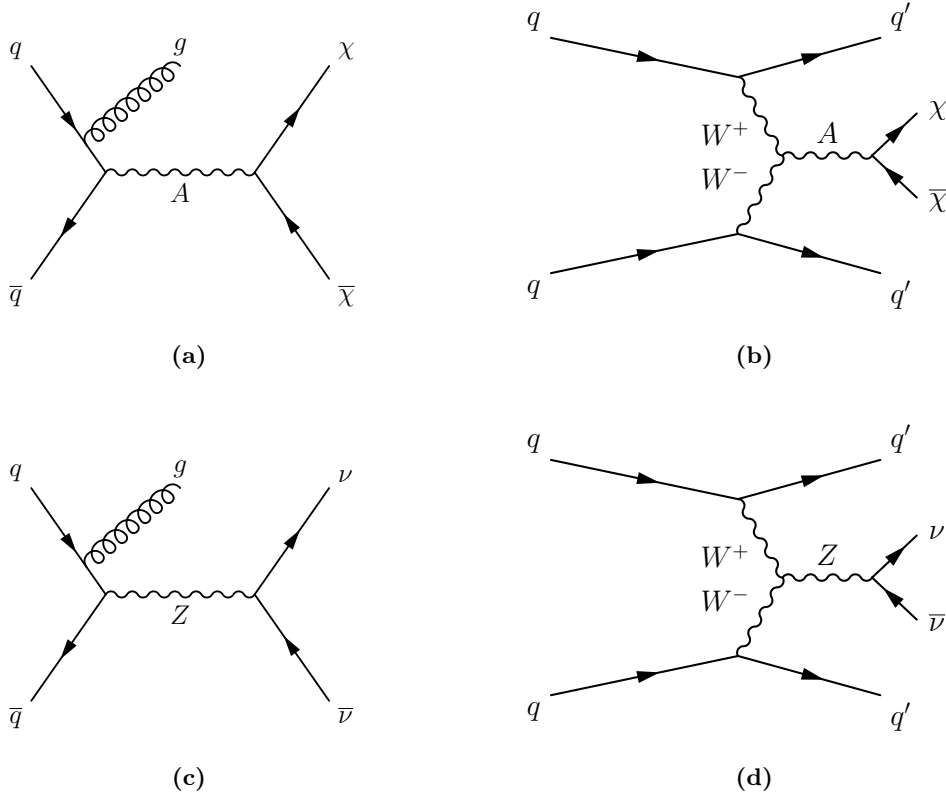
**Figure 5.1.** Feynman diagrams for WIMP production, $\chi$, with mediator $A$ (a) in association with one jet and (b) via VBF production. Example Feynman diagrams for the SM background to (c) the process with one jet and (d) the VBF process.

by the SM is 5.9 [9] and BSM contributions to $p_{\mathrm{T}}^{\mathrm{miss}}$ + jets events in the numerator would lead to a discrepancy.

Two phase spaces are defined for this analysis, the $\geq 1$ jet phase space with at least one high-$p_{\mathrm{T}}$ jet, and the VBF phase space with at least two high-$p_{\mathrm{T}}$ jets and additional selection requirements to enhance the VBF process, which is sensitive to DM models involving couplings to electroweak (EWK) bosons. The $R^{\mathrm{miss}}$ observable is corrected for detector inefficiency and resolution and is measured differentially as a function of four variables, $p_{\mathrm{T}}^{\mathrm{miss}}$ in the $\geq 1$ jet phase space, and $p_{\mathrm{T}}^{\mathrm{miss}}$, $m_{\mathrm{jj}}$ and $\Delta\phi_{\mathrm{jj}}$ in the VBF phase space, where $m_{\mathrm{jj}}$ is the di-jet invariant mass and $\Delta\phi_{\mathrm{jj}}$ is the difference in azimuthal angle between the two leading jets. The $p_{\mathrm{T}}^{\mathrm{miss}}$ is directly sensitive to the DM system and the BSM models typically have harder $p_{\mathrm{T}}^{\mathrm{miss}}$ distributions than the SM $Z$ + jets process. The $m_{\mathrm{jj}}$ distribution provides more discriminating power for VBF processes at large values and the azimuthal correlation between the two jets can be very different depending on the spin of the mediator.

The advantages of this detector-corrected ratio approach include the cancellation of the theoretical and many of the experimental systematic uncertainties. The selection criteria for the numerator and the denominator are chosen to be as similar as possible. Even though the denominator contains charged leptons instead of invisible neutrinos, the $p_T^{miss}$ in the denominator can be made similar to that of the numerator by treating the identified charged leptons as invisible particles in the $p_T^{miss}$ calculation. Theorists without access to the ATLAS detector simulation can use the measurement to test alternative BSM models not considered in this analysis. The detector-corrected ratios can also be used to improve the MC simulation of the SM processes in the extreme regions of the phase spaces. Any future improvements to the SM simulation can be used to update the exclusion limits on the BSM models. The main disadvantages of this approach are the limited statistical precision achievable using the $\ell^+\ell^-$ + jets data for the denominator, since the branching ratio of $Z \to \ell^+\ell^-$ is less than that of $Z \to \nu\bar{\nu}$, and the fact that understanding detector effects and correcting for them is more time consuming than a detector level measurement.

The remainder of this Chapter describes how the measurement is performed. The MC samples used for the analysis are described in Section 5.2. The event and object selections for detector level and particle level are provided in Section 5.3. The measurement of the $p_T^{miss}$ + jets numerator including determination of all backgrounds and systematic uncertainties is given in Section 5.4. The measurement of the $\ell^+\ell^-$ + jets denominator and detector corrections is given in Section 5.5. The construction of the detector-corrected ratio $R^{miss}$ and comparisons to the SM predictions are provided in Section 5.6. Finally, the detector-corrected ratios are used to set limits on BSM models in Section 5.7.

## 5.2. Monte Carlo simulation

Events containing $W$ or $Z$ bosons in association with jets ($V$ + jets) [176] are generated using the SHERPA v2.2.0 generator. In SHERPA, MEs are calculated for up to two partons at NLO accuracy and up to four partons at LO accuracy using Comix [177] and OpenLoops [178], and merged using the ME+PS@NLO prescription [179]. The fully hadronic final state is generated using PS, hadronisation and MPI algorithms. The NNPDF3.0nnlo PDF set [180] is used in conjunction with dedicated PS tuning developed by the SHERPA authors. The samples are normalised to cross-sections at NNLO accuracy [181]. The samples have been produced with a simplified scale setting prescription in the multi-parton MEs, to improve the event generation speed. A theory-based re-weighting of the jet multiplicity distribution is applied at event level, derived from event generation with the strict scale prescription.

$V$ + jets processes are also generated using MADGRAPH5_aMC@NLO v2.2.2 at LO interfaced to the PYTHIA v8.186 PS, hadronisation and UE model in order to allow additional cross-checks. The A14 tune is used together with the NNPDF3.0nlo PDF set and these samples are also normalised to the same cross-sections at NNLO accuracy as the SHERPA $V$ + jets samples.

Purely EWK production of $V$ + jets events, which include the VBF Z diagram but also semileptonic $VV$ diagrams where one of the weak bosons decays hadronically, are generated at LO accuracy in QED using SHERPA v2.1.1 with the CT10nlo PDF set [70] and the dedicated PS tuning developed by the SHERPA authors. This generator combination is also used to produce fully leptonic decays of dibosons [182] at NLO accuracy in QED. These generator cross-sections have been scaled down by 9% to account for the usage of $\alpha_{\text{QED}} = 1/129$ rather than $1/132$, corresponding to the use of current parameters defined by the Particle Data Group as input to the $G_\mu$ scheme [183]. $V$ + jets processes generated using SHERPA v2.1.1 are also used for cross-checks.

Top-antitop pair production [184] and single-top production in the $Wt$ [185] and $s$-channels [186] are generated using the POWHEG-BOX v2 generator with the CT10nlo PDF sets in the ME calculations. Single-top production in the $t$-channel [187] is generated using the POWHEG-BOX v1 generator. This generator uses the 4-flavour scheme for the NLO ME calculations together with the fixed four-flavour PDF set CT10f4. For all top processes [188], top-quark spin correlations are preserved, and for $t$-channel, top quarks are decayed using MadSpin [189]. The PS, hadronisation and UE are added by interfacing the POWHEG-BOX events to PYTHIA v6.428, using the CTEQ6L1 PDF set [190] and the Perugia 2012 tune [191] for UE activity. The top mass is set to 172.5 GeV. The top-pair samples are normalised to a calculation at NNLO accuracy including soft-gluon resummation at next-to-next-to-leading logarithmic (NNLL) accuracy [192]. The single-top samples are normalised to a NLO calculation including the resummation of soft gluon terms at NNLL accuracy [193–195].

Multi-jet processes are generated at LO accuracy in QCD using PYTHIA v8.186 for $2 \rightarrow 2$ partonic scattering plus PS for additional jet activity. The A14 tune is used together with the NNPDF2.3lo PDF set [72]. The EvtGen v1.2.0 program [196] is used for modelling the properties of the bottom and charm hadron decays in all samples generated with MADGRAPH5_aMC@NLO, POWHEG-BOX and PYTHIA.

WIMP simplified signal models with $s$-channel spin-1 mediator exchange at NLO precision are generated using POWHEG-BOX v2 r3049 DMV model [197] and interfaced to PYTHIA v8.205 for the PS, hadronisation and the UE, with the A14 tune and the NNPDF3.0nlo PDF set. The couplings of the mediator to SM quarks, $g_q$, and of WIMP

particles to the mediator, $g_\chi$, are set to a constant value of 0.25 and 1, respectively. A grid of samples is produced for WIMP masses ranging from 1 GeV to 1 TeV and mediator masses between 10 GeV and 2 TeV.

The invisible decay of the Higgs boson, $H \to ZZ \to \nu\bar{\nu}\nu\bar{\nu}$, is generated using Powheg-Box v1 [198–200] with the CT10 PDF set, and interfaced to Pythia v8.165 for the PS, hadronisation and UE. The Higgs boson production processes are normalised to cross-sections calculated by the LHC Higgs Cross Section Working Group [201].

An implementation of the EFT model described in Section 2.2.2 is generated using MadGraph5_aMC@NLO v2.2.3 with the NNPDF2.3lo PDF set, interfaced to Pythia v8.212 with the A14 tune to simulate the PS, hadronisation and the UE.

All SM MC samples are passed through GEANT4 for a full simulation of the ATLAS detector and are then reconstructed using the same analysis chain as the data. The invisible Higgs and the EFT samples are only used at particle level, while the WIMP simplified signal models are also used at detector level to cross-check the detector corrections. Pileup interactions are simulated using Pythia v8.186 with the A2 parton shower tune and the MSTW2008lo PDF set.

Detector-level MC events with charged leptons are reweighted using scale factors (SFs) per-lepton to account for known efficiency differences between data and simulation [148, 150, 151]. The SFs are defined as the lepton efficiency in data divided by the lepton efficiency in the MC. The pileup interactions in the MC samples are initially generated using a pileup profile expected for the data. However, there are some differences between data and simulation, due to the difference in the measured luminosity at the beginning of the data taking period and the final calibrated luminosity. The impact of pileup reweighting has been investigated and found to have little impact on this analysis, so no additional reweighting has been applied to correct for the remaining mismodelling.

## 5.3. Event and object selection

### 5.3.1. Particle-level selection

Particles used in the analysis are required to be final-state particles, defined as having a mean lifetime of more than $10\,\mathrm{mm}c^{-1}$, where $c$ is the speed of light. Prompt final state particles are defined as not originating from the decay of a hadron or a tau lepton. Particle-level electrons and muons are "dressed" [202], by adding the four-momenta of FSR photons within $\Delta R = 0.1$. Particles that can interact via the strong or EM forces are

| $R^{\text{miss}}$ | $\geq 1$ jet | VBF |
|---|---|---|
| $p_{\text{T}}^{\text{miss}}$ | $> 200$ GeV | |
| Lepton veto | No $e, \mu$ with $p_{\text{T}} > 7$ GeV, $|\eta| < 2.5$ | |
| All jet $|y|$ | $< 4.4$ | |
| All jet $p_{\text{T}}$ | $> 25$ GeV | |
| $\Delta\phi(\text{jet}, p_{\text{T}}^{\text{miss}})$ | $> 0.4$, for the four leading jets with $p_{\text{T}} > 30$ GeV | |
| Leading jet $p_{\text{T}}$ | $> 120$ GeV | $> 80$ GeV |
| Subleading jet $p_{\text{T}}$ | – | $> 50$ GeV |
| Leading jet $|\eta|$ | $< 2.4$ | – |
| $m_{\text{jj}}$ | – | $> 200$ GeV |
| Central-jet veto | – | No jets with $p_{\text{T}} > 25$ GeV |
| **Denominator only** | $\geq 1$ jet and VBF | |
| Leading lepton $p_{\text{T}}$ | $> 80$ GeV | |
| Subleading lepton $p_{\text{T}}$ | $> 7$ GeV | |
| Lepton $|\eta|$ | $< 2.5$ | |
| $m_{\ell\ell}$ | 66–116 GeV | |
| $\Delta R(\text{jet}, \text{lepton})$ | $> 0.5$, otherwise jet is removed | |

**Table 5.1.** Particle-level fiducial definitions for the $\geq 1$ jet and VBF phase spaces.

referred to as visible particles, whereas particles that do not interact via the strong or EM forces (neutrinos, DM particles) are referred to as invisible particles. The $p_{\text{T}}^{\text{miss}}$ is defined as the magnitude of the negative vector sum of the transverse components of all final-state visible particles within $|\eta| < 4.9$. Jets are reconstructed using the anti-$k_t$ jet clustering algorithm with a jet-radius parameter of $R = 0.4$, excluding muons and invisible particles.

The phase space dependent requirements for both the $p_{\text{T}}^{\text{miss}}$ + jets numerator and the $\ell^+\ell^-$ + jets denominator at particle level are summarised in Table 5.1. The $p_{\text{T}}^{\text{miss}}$ is required to be larger than 200 GeV, motivated by the efficiency plateau of the trigger used at detector-level (HLT_xe70). All jets are required to have $p_{\text{T}} > 25$ GeV and $|y| < 4.4$. The $\geq 1$ jet phase space is defined as having at least one jet with $p_{\text{T}} > 120$ GeV and $|\eta| < 2.4$. The VBF phase space is defined as having at least two jets with $p_{\text{T}} > 50$ GeV, at least one of which has $p_{\text{T}} > 80$ GeV, and $m_{\text{jj}} > 200$ GeV. The $m_{\text{jj}}$ requirement is used to suppress contributions from diboson events if one of the bosons decays hadronically. A central-jet veto is applied to reject events with any additional jets with $p_{\text{T}} > 25$ GeV within the rapidity interval between the two leading jets. The central jet veto is used to enhance the contribution from VBF processes, in which less QCD radiation is expected in

the rapidity gap between the two leading jets, due to the colourless exchange. Multi-jet backgrounds are suppressed by requiring $\Delta\phi(\text{jet}_i, p_T^{\text{miss}}) > 0.4$, where $i = 1, \ldots 4$ runs over the four highest $p_T$ jets with $p_T > 30$ GeV.

A lepton veto is applied on electrons and muons (prompt or from tau lepton decays) to events in the numerator to reduce the contribution from background processes, mainly $W^\pm +$ jets. Hadronically decaying tau leptons are not included in the lepton veto at particle level.

Events selected for the denominator are required to contain exactly one pair of oppositely charged prompt muons or electrons, with $p_T > 7$ GeV and $|\eta| < 2.5$. The leading lepton is required to have $p_T > 80$ GeV to reduce backgrounds from $t\bar{t}$ events, which typically have a lower leading lepton $p_T$. The selected leptons are not included in the $p_T^{\text{miss}}$ calculation in order to make the $p_T^{\text{miss}}$ as similar as possible to the quantity used in the numerator. The invariant mass of the lepton pair, $m_{\ell\ell}$, is required to be between 66–116 GeV to minimise the contribution from $\gamma^* \to \ell^+\ell^-$ and associated interference terms. Jets are removed if they are within $\Delta R < 0.5$ of muons or electrons. A large $\Delta R$ requirement is chosen due to observed differences between electrons and muons when a smaller $\Delta R$ cut is used, because electrons are included in the jet reconstruction while muons are not.

### 5.3.2. Detector-level selection

Only the requirements on the detector-level objects are described in this Section. The reconstruction, identification and calibration of each object in the detector are described in Section 3.3. The detector-level kinematic definitions for the fiducial $\geq 1$ jet and VBF phase spaces are the same as the particle-level ones, with additional requirements described below.

Muons are required to have $p_T > 7$ GeV, $|\eta| < 2.5$ and to be of type *Combined* or *Segment-tagged*. They must also satisfy a set of *Loose* selection criteria, which include track quality requirements to suppress backgrounds from fake tracks and muons from hadron decays. Impact parameter requirements are applied to ensure that the muon candidates originate from the primary vertex. The longitudinal impact parameter requirement is $|z_0 \times \sin\theta| < 0.5$ mm and the transverse significance with respect to the primary vertex requirement is $|d_0|/\sigma(d_0) < 3$, where $|d_0|$ is the distance of closest approach to the primary vertex in the transverse plane and $|z_0 \times \sin\theta|$ is the distance of closest approach in the longitudinal direction. Isolated muon candidates are selected using the *LooseTrackOnly* isolation working point. Muons selected for the $\mu^+\mu^- +$ jets denominator are not required

to be isolated due to the inefficiency of this requirement and the very low background in these events.

Electrons are required to have $p_T > 7$ GeV and $|\eta| < 2.47$, excluding the transition regions between barrel and end-cap EM calorimeters of $1.37 < |\eta| < 1.52$, referred to as the crack region. They must also satisfy a set of *Loose* likelihood selection criteria and originate from areas of the calorimeter without problems. Impact parameter requirements are applied to ensure that the electron candidates originate from the primary vertex. The longitudinal impact parameter requirement is $|z_0 \times \sin\theta| < 0.5$ mm and the transverse significance with respect to the primary vertex requirement is $|d_0|/\sigma(d_0) < 5$. Isolated electron candidates are selected using the *LooseTrackOnly* isolation working point.

Hadronically decaying tau leptons are required to have $p_T > 20$ GeV and be within $|\eta| < 2.47$, excluding the crack region. They must also satisfy a set of *Loose* selection criteria, have one or three associated tracks, a unit charge, and pass an electron overlap removal.

Jets are reconstructed from topo-clusters at the EM scale using the anti-$k_t$ jet algorithm with a jet-radius parameter of $R = 0.4$. They are required to have $p_T > 25$ GeV and $|y| < 4.4$. Pileup jets are rejected by requiring jets with $20 < p_T < 50$ GeV and $|\eta| < 2.4$ to satisfy JVT $> 0.64$. Photons are not considered and are treated as jets in the analysis.

A modified version of the recommended overlap removal procedure [203] is used to remove overlaps between muons, electrons, tau leptons and jets. Jets are removed if they are within $\Delta R < 0.5$ of selected isolated muons or electrons. Jets are also removed if they are within $\Delta R < 0.2$ of selected tau leptons. Additional overlap removal requirements are used for the non-isolated muons of the $\mu^+\mu^- +$ jets denominator. In this case, jets are considered to be consistent with a final-state photon and removed if they are within $\Delta R < 0.5$ of a muon, with less than five associated ID tracks and jet $p_T$ less than twice the $p_T$ of the muon. Otherwise the muon is considered to originate from the jet and is removed if it has $p_T < 20$ GeV. Electrons and tau leptons within $\Delta R < 0.3$ of a muon are also considered to be consistent with a final-state photon and removed.

Events for the $p_T^{\text{miss}} +$ jets numerator and the $\mu^+\mu^- +$ jets denominator are selected using HLT_xe70, the lowest unprescaled $p_T^{\text{miss}}$ trigger in 2015. A $p_T^{\text{miss}}$ trigger can be used to select events for the $\mu^+\mu^- +$ jets denominator since muons are not used in the trigger $p_T^{\text{miss}}$ calculation. Events for the $e^+e^- +$ jets denominator are selected using a logical OR combination of three single electron triggers, HLT_e24_lhmedium_L1EM20VH, HLT_e60_lhmedium and HLT_e120_lhloose. Only good quality data are considered, obtained when the detector was fully operational, with a total integrated luminosity of 3.2 fb$^{-1}$. Each event is required to have a primary vertex with at least two associated tracks. The $p_T^{\text{miss}}$
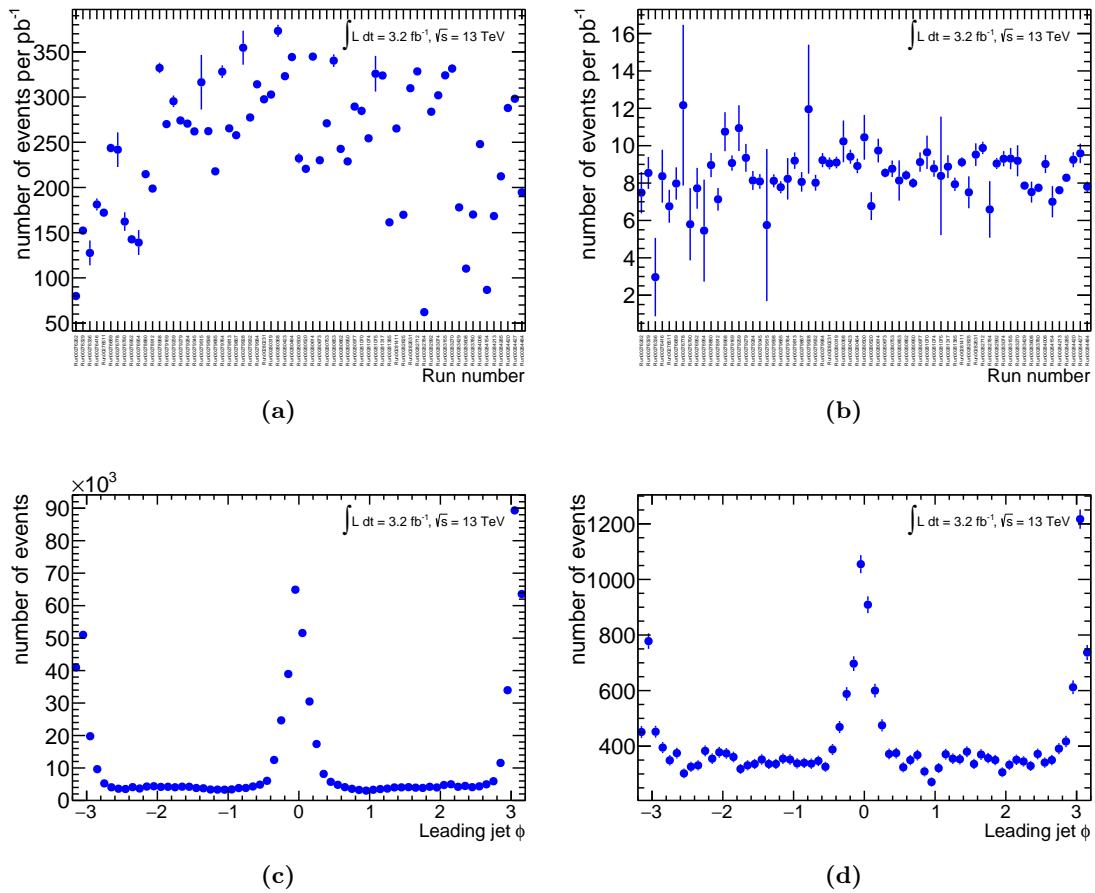
**Figure 5.2.** Data stability in the $p_{\mathrm{T}}^{\mathrm{miss}}$ + jets signal region before requiring the leading jet to pass the tight jet cleaning cuts. The number of events per pb$^{-1}$ for each of the 65 runs in the 2015 dataset are shown (a) in the $\geq 1$ jet phase space, and (b) in the VBF phase space. The distributions are very unstable due to large contamination from non-collision backgrounds, causing large spikes in the $\phi$ distribution of the leading jet around $\pm\pi$ and 0, shown in (c) the $\geq 1$ jet phase space, and (d) the VBF phase space.

in each event must be greater than 200 GeV, motived by the `HLT_xe70` trigger efficiency plateau. The detector-level lepton veto includes hadronically decaying tau leptons.

Events containing bad quality jets are rejected using the *LooseBad* criteria, in order to suppress non-collision backgrounds and calorimeter noise. However, the $p_{\mathrm{T}}^{\mathrm{miss}}$ + jets signal region has a large contamination from non-collision backgrounds, even after the jet cleaning using the *LooseBad* criteria. Figure 5.2a and 5.2b shows the data stability, defined as the number of events per pb$^{-1}$ as a function of the 65 data collection runs in the 2015 dataset. The event yields per luminosity are very unstable, due to large contamination from non-collision backgrounds. The non-collision backgrounds cause large spikes in the $\phi$ distribution of the leading jet around $\pm\pi$ and 0 as shown in Figure 5.2c and 5.2d. The
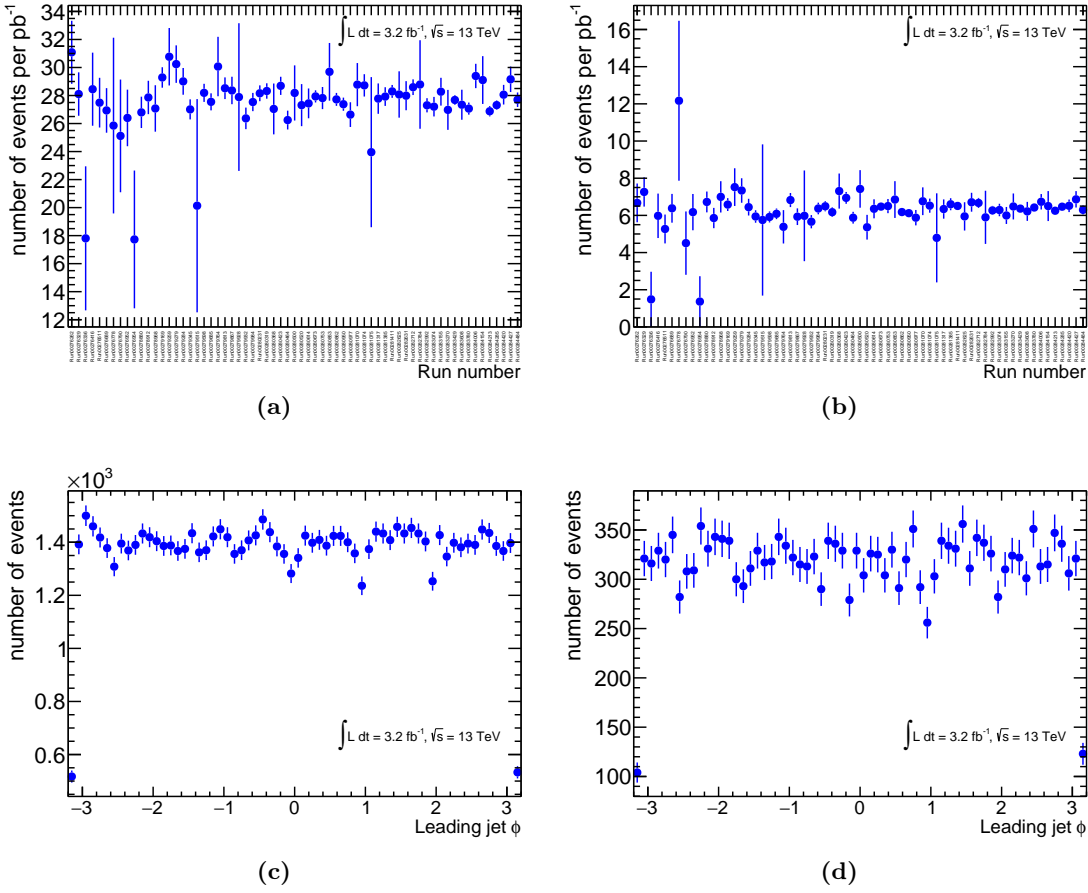
**Figure 5.3.** Data stability in the $p_T^{miss}$ + jets signal region after requiring the leading jet to pass the tight jet cleaning cuts. The number of events per pb$^{-1}$ for each of the 65 runs in the 2015 dataset are shown (a) in the $\geq 1$ jet phase space, and (b) in the VBF phase space. The distributions are stable and the large spikes have disappeared from the $\phi$ distribution of the leading jet, in (c) the $\geq 1$ jet phase space, and (d) the VBF phase space.

*TightBad* jet-cleaning criteria are used on the leading jet to further reduce the non-collision backgrounds, improving the data stability as shown in Figure 5.3 and removing the spikes in the $\phi$ distribution.

## 5.4. The $p_T^{miss}$ + jets numerator

The comparison of data and MC for the selected $p_T^{miss}$ + jets events is shown in Figure 5.4. This region was blinded by requiring $p_T^{miss} < 500$ GeV and $m_{jj} < 750$ GeV to avoid potential bias when looking at the tails of the distributions. The results were unblinded after all selections and background determination methods were finalised and approved by the

relevant ATLAS working group. The total backgrounds are approximately as large as the $Z \to \nu\bar{\nu}$ component with the largest contributions coming from the $W^{\pm} +$ jets samples and smaller contributions from top-quark and diboson events. These events contain genuine $p_T^{\mathrm{miss}}$ from neutrinos and can survive the lepton veto if either the charged lepton is not reconstructed and identified or is outside the acceptance of the tracking detector. The clear disagreement between data and MC in conjunction with the size of the $W^{\pm} +$ jets backgrounds mean that data-driven methods are required to constrain the modelling of $W^{\pm} +$ jets events. These methods are described in Section 5.4.1. The background from $Z \to \ell^+\ell^-$ events, in which both leptons are not identified or are outside the detector acceptance, is very small and is estimated using the MC.

The remaining small background in Figure 5.4 comes from multi-jet events, in which the $p_T$ of one or more jets is mismeasured, leading to a large $p_T^{\mathrm{miss}}$. The $\Delta\phi(\mathrm{jet}, p_T^{\mathrm{miss}})$ requirement is designed to suppress this background as the $p_T^{\mathrm{miss}}$ typically points to the direction of the mismeasured jet. Even though the contribution from this background is small, a control region is used to estimate it using the jet smearing method [204]. The control region requires one of the four leading jets to satisfy $\Delta\phi(\mathrm{jet}, p_T^{\mathrm{miss}}) < 0.1$. Combinations of single-jet triggers are used to select events with high-$p_T$ jets. These events are required to have well-measured jets resulting in small $p_T^{\mathrm{miss}}$ and are referred to as seed events. The jets in the seed events are smeared $25\,000$ times per event according to the distribution of the jet response, resulting in events passing the $p_T^{\mathrm{miss}} > 200$ GeV requirement which are then used to extrapolate between the control and the signal region. A 50% uncertainty is assigned to the number of predicted events, together with a smaller uncertainty, estimated by varying the event selection criteria used as input for the jet smearing method [175].

## 5.4.1. Methodology for determining the $W^{\pm} +$ jets backgrounds

The $W^{\pm} +$ jets control regions have identical event selection requirements to the $p_T^{\mathrm{miss}} +$ jets signal region, with the exception that a single charged lepton with $p_T > 25$ GeV is required. In each control region, MC samples are compared to the data if they contain a prompt lepton from $W \to l\nu$, or a lepton from the tau lepton decay in $W \to \tau\nu$. Contributions from other processes ($Z \to \ell^+\ell^-$ events or multi-jet events) are subtracted from the data. To avoid double counting, contributions from MC samples that contain more than one prompt lepton (such as fully leptonic $t\bar{t}$ and diboson events) are split using particle-level information according to the following criteria. An event containing a prompt muon or a muon from a tau lepton decay enters the $W \to \mu\nu$ control region. An event containing a prompt electron or an electron from a tau lepton decay enters the $W \to e\nu$ control region if there are no additional prompt muons or muons from a tau lepton decay. An event
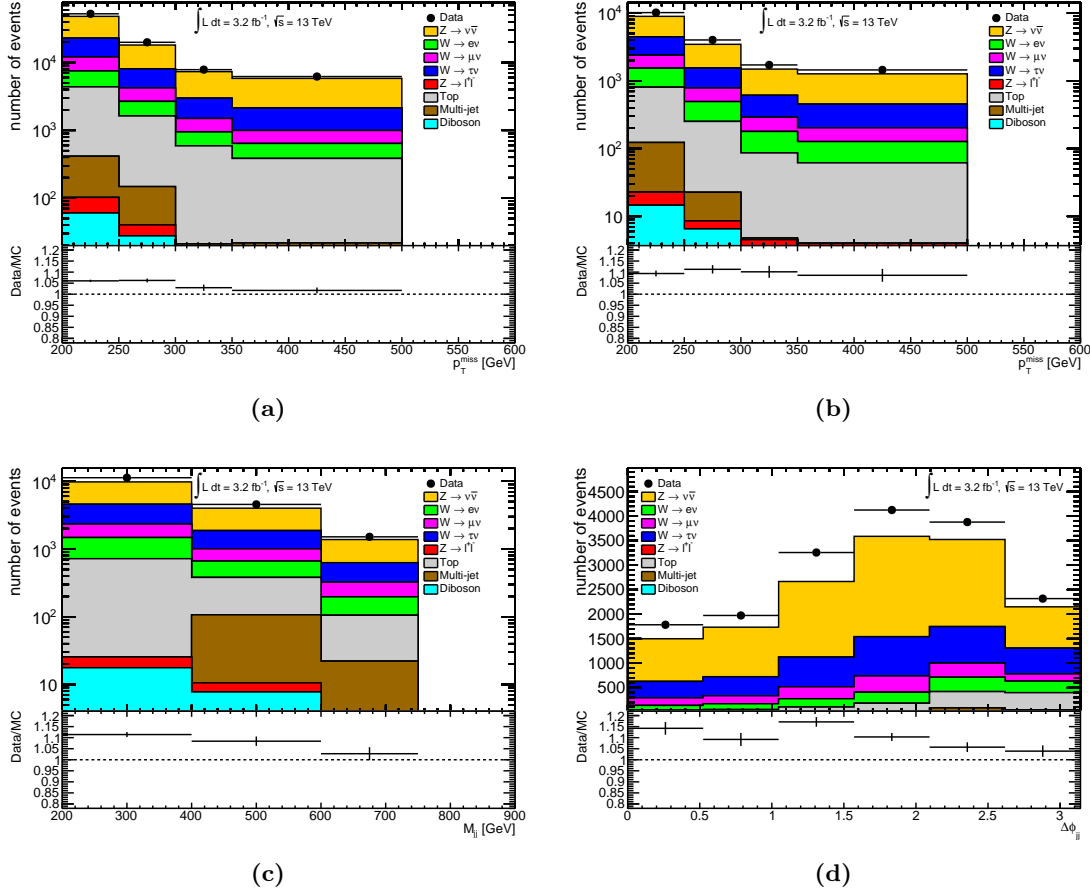
**Figure 5.4.** Comparisons between data and MC for the blinded $p_T^{miss}$ + jets numerator as a function of (a) $p_T^{miss}$ in the $\geq 1$ jet phase space, and (b) $p_T^{miss}$, (c) $m_{jj}$, (d) $\Delta\phi_{jj}$ in the VBF phase space. The contributions from the EWK $V$ + jets samples have been added to the $V$ + jets samples.

containing a prompt hadronically decaying tau lepton enters the $W \to \tau\nu$ control region if there are no additional prompt muons or electrons.

$W^{\pm}$ + jets events enter the signal region if the lepton is outside the detector acceptance ($p_T < 7$ GeV and $|\eta| > 2.5$) or within the acceptance but not reconstructed or identified, failing one or more of the selection requirements. While it is not possible to identify these events in the data, they are present in the MC and can be identified. Two methods, labelled Method 1 and Method 2, are used to estimate this background and give consistent results. The background estimates from Method 1 are used in the nominal analysis chain. Method 1 has been developed for this analysis, while Method 2 was used in previous mono-jet analyses.

**Method 1**

Method 1 starts from first principles, separating the contributions from out-of-acceptance and in-acceptance $W^{\pm} +$ jets events. The number of $W^{\pm} +$ jets background events that are selected in the $p_{\mathrm{T}}^{\mathrm{miss}} +$ jets signal region in the data, $N_{\mathrm{background}}^{\mathrm{Method\,1}}$, can be written as

$$N_{\mathrm{background}}^{\mathrm{Method\,1}} = N_{\mathrm{out}} + N_{\mathrm{missed}} \tag{5.2}$$

where $N_{\mathrm{out}}$ is the number of events in which the lepton is outside the acceptance and $N_{\mathrm{missed}}$ is the number of events in which the lepton is within the acceptance but not reconstructed and identified. These two terms can be written as

$$N_{\mathrm{background}}^{\mathrm{Method\,1}} = (1 - a_7)\,N_{\mathrm{all}} + a_7\,(1 - \varepsilon)\,N_{all} \tag{5.3}$$

where $a_7$ is the fraction of events within the acceptance and with lepton $p_{\mathrm{T}} > 7$ GeV, $\varepsilon$ is the lepton efficiency averaged across all selected events, and $N_{\mathrm{all}}$ is the number of $W^{\pm} +$ jets events that contain zero or one reconstructed charged leptons that would pass all other $p_{\mathrm{T}}^{\mathrm{miss}} +$ jets selection cuts. The $N_{\mathrm{all}}$ term can be written in terms of events selected in a control region in data, such that

$$N_{\mathrm{background}}^{\mathrm{Method\,1}} = (1 - a_7)\,\frac{N_{\mathrm{control}}}{\varepsilon \cdot a_{25}} + a_7\,(1 - \varepsilon)\,\frac{N_{\mathrm{control}}}{\varepsilon \cdot a_{25}} \tag{5.4}$$

where $a_{25}$ is the fraction of events within the acceptance and with lepton $p_{\mathrm{T}} > 25$ GeV and $N_{\mathrm{control}}$ is the number of events selected in the control region in the data with reconstructed lepton $p_{\mathrm{T}} > 25$ GeV.

The above equation can obviously be algebraically simplified, but it is written in the form given in Equation 5.4 in order to make explicit the 'in' and 'out' of acceptance terms separately. The equation is written in terms of an average lepton efficiency, which is achieved by using $p_{\mathrm{T}}$- and $\eta$-dependent efficiencies on an event-by-event basis. The acceptance terms are evaluated from the MC simulation. The MC events are reweighted using SFs per-lepton to account for known efficiency differences between data and simulation. This means effectively that $N_{25} \rightarrow \langle SF \rangle \times N_{25}$, where $\langle SF \rangle$ is the average scale factor for the efficiency of the lepton. The value of $N_{\mathrm{background}}^{\mathrm{Method\,1}}$ is predicted bin-by-bin for each observable of interest, such as $p_{\mathrm{T}}^{\mathrm{miss}}$ in the $\geq 1$ jet phase space, with the input values of $N_{\mathrm{control}}$, $\varepsilon$, $a_7$ and $a_{25}$ also determined bin-by-bin for each observable of interest. The statistical uncertainties on the acceptance terms are determined using a bootstrap method [205], accounting for correlations between terms. The muon efficiencies are provided by the relevant ATLAS Combined Performance working group, whereas the electron and tau efficiencies are calculated from the $W \rightarrow e\nu$ and $W \rightarrow \tau\nu$ MC samples as part of this analysis and are given in Appendix A.

**Method 2**

The number of $W^{\pm} + $ jets background events that are selected in the $p_{\mathrm{T}}^{\mathrm{miss}} + $ jets signal region in the data, $N_{\mathrm{background}}^{\mathrm{Method\,2}}$, can be estimated using a different method

$$N_{\mathrm{background}}^{\mathrm{Method\,2}} = \frac{N_{\mathrm{control}}}{N_{\mathrm{control}}^{\mathrm{MC}}} \times N_{\mathrm{background}}^{\mathrm{MC}} \tag{5.5}$$

where $N_{\mathrm{control}}$ is the yield in the data control region with lepton $p_{\mathrm{T}} > 25$ GeV, $N_{\mathrm{control}}^{\mathrm{MC}}$ is the yield for the MC in the control region, and $N_{\mathrm{background}}^{\mathrm{MC}}$ is the MC estimate of the $W^{\pm} + $ jets background in the signal region. The predicted number of background events is determined bin-by-bin for each observable of interest. To reduce the effects of statistical fluctuations, the quantity $N_{\mathrm{control}}$ / $N_{\mathrm{control}}^{\mathrm{MC}}$ is plotted as a function of each observable of interest and fitted using a first-order polynomial. The value of the fitted function is used to supply the value of $N_{\mathrm{control}}$ / $N_{\mathrm{control}}^{\mathrm{MC}}$ in Equation 5.5.

The MC is corrected for the known efficiency differences between data and simulation. This means that the number of simulated events in the control region is scaled by the scale factors per-lepton such that $N_{\mathrm{control}} \to \langle SF \rangle \times N_{\mathrm{control}}$. The number of background events in the signal region in the simulation cannot be similarly reweighted due to the explicit lepton veto, meaning a per-lepton reweighting factor cannot be defined. However, $N_{\mathrm{all}}^{\mathrm{MC}}$, which is the number of MC $W^{\pm} + $ jets events that contain zero or one charged leptons (counting electrons, muons and tau leptons) that would pass all other $p_{\mathrm{T}}^{\mathrm{miss}} + $ jets selection cuts, is independent of lepton efficiencies. An increase in efficiency would increase the number of events in the control region but decrease the number of events in the signal region. Therefore, $N_{\mathrm{background}}^{\mathrm{MC}}$ can be defined using the following equation.

$$N_{\mathrm{background}}^{\mathrm{MC}} = N_{\mathrm{all}}^{\mathrm{MC}} - \langle SF \rangle N_{\mathrm{control}}^{\mathrm{MC}} \tag{5.6}$$

The quantity $N_{\mathrm{background}}^{\mathrm{MC}}$ obtained from Equation 5.6 is used in Equation 5.5.

The two methods are not independent as they use the same events in data and simulation. Method 2 requires the lepton $p_{\mathrm{T}}$ and $\eta$ distributions to be well modelled in MC, because the ratio of data to MC can be affected by differences in reconstruction and identification efficiency for leptons with different kinematics. Method 1 is less susceptible to mismodelling in the lepton $p_{\mathrm{T}}$ and $\eta$ distributions, as the number of events in data and MC are corrected on an event-by-event basis for lepton efficiency. If the lepton kinematics are well modelled in MC then the two methods should give very similar results. The uncertainties shown in the following distributions are statistical only, unless otherwise stated. Plots are labelled with "Method 1" or "Method 2" depending on the method used to create them.

### 5.4.2. Background estimate for events with $W \to \mu\nu$

The control region for events with $W \to \mu\nu$ contains a single muon with $p_{\mathrm{T}} > 25$ GeV and no other leptons. The `HLT_xe70` trigger, used in the signal region, is also used in this control region to select events. The muon is treated as invisible in the $p_{\mathrm{T}}^{\mathrm{miss}}$ calculation and the $p_{\mathrm{T}}^{\mathrm{miss}}$ in this control region corresponds to the $p_{\mathrm{T}}$ of the W boson.

Contributions from processes that do not contain a prompt lepton from $W \to \mu\nu$, or a muon from the tau lepton decay in $W \to \tau\nu$, are estimated using the MC and subtracted from the data. This includes $Z \to \ell^+\ell^-$ and multi-jet events. The subtraction of the multi-jet background can be problematic due to the fact that few multi-jet events pass the event selection criteria, but those that do tend to have large MC event weights and produce fluctuations in the background-subtracted data as shown in Figure 5.5. For Method 2, the fit to the data and MC ratio in the control region smooths out these fluctuations. However, for Method 1, the fluctuations in the background-subtracted data in the control region would be propagated directly to the signal region when applying the acceptance corrections. For this reason, the impact of multi-jet events in the control region for events with $W \to \mu\nu$ on the background prediction in the signal region is estimated using Method 2 (by applying and not applying the subtraction of multi-jet events from the data in the control region) and the Method 1 prediction in the signal region is scaled accordingly.

A data-driven method [206] has also been investigated for determining the multi-jet background. This method defines four control regions in data and MC by reversing two of the selection requirements: isolation or the transverse significance with respect to the primary vertex. Control region A is the same as the control region for events with $W \to \mu\nu$, control region B requires the muon to fail the isolation requirement, control region C requires the muon to fail the transverse significance with respect to the primary vertex requirement, and control region D requires the muon to fail both the isolation and transverse significance requirements, resulting in a multi-jet enriched control region. The four control regions can be used to define four equations containing four unknowns that can be algebraically solved to determine the multi-jet background. Multi-jet events are not included in the MC for this method, but they are included in the data. The method relies on control region D having more events in data than the MC, due to the multi-jet background in the data. When this method was used, the MC predicted more events than the data for control region D, indicating that the multi-jet background is very small, and the events in control region D are actual $W \to \mu\nu$ events with the lepton simply failing the two reversed requirements. This cross-check justifies the subtraction of the multi-jet background from MC only.

Efficiency-corrected distributions of muon kinematics are shown in Figure 5.6. Reasonable agreement between data and MC is observed. There is an asymmetry in the
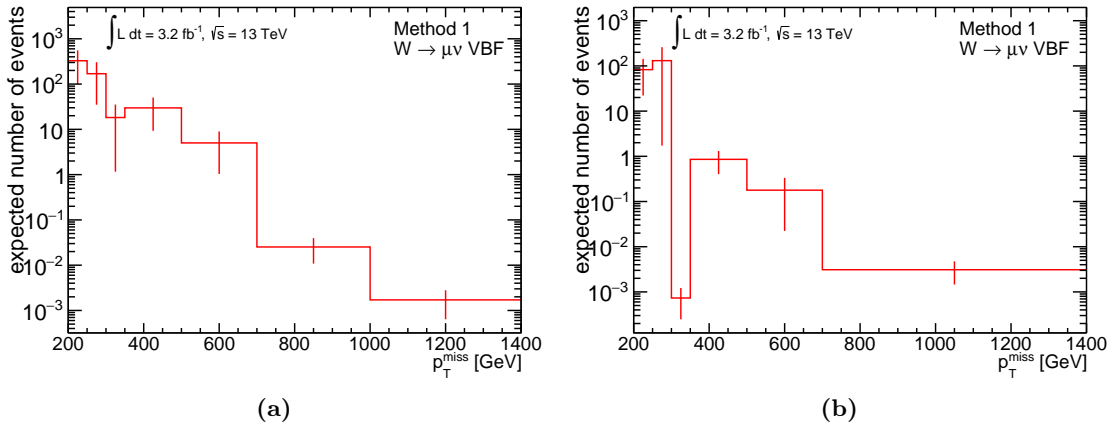
**Figure 5.5.** Multi-jet background in the efficiency corrected control region for events with $W \to \mu\nu$ as a function of (a) $p_T^{\text{miss}}$ in the $\geq 1$ jet phase space, and (b) $p_T^{\text{miss}}$ in the VBF phase space.

$\eta$ distribution caused by the SHERPA v2.2.0 samples, that is not present in the MAD-GRAPH5_aMC@NLO samples.

Comparisons between data and MC as a function of $p_T^{\text{miss}}$ in the $\geq 1$ jet and VBF phase spaces are shown in Figure 5.7. The efficiency correction has a negligible effect on the data and MC agreement. The data are larger than the MC at low $p_T^{\text{miss}}$ and smaller at high $p_T^{\text{miss}}$. This might suggest additional backgrounds not accounted for in the data, but is actually a known mismodelling of the SHERPA v2.2.0 samples [207]. This mismodelling justifies the need for a data-driven background method. The dominant contribution comes from the $W \to \mu\nu$ MC sample as expected, followed by the contribution of $t\bar{t}$ and single-top events. The contribution from the $W \to \tau\nu$ MC sample is significantly smaller and is less important when calculating the acceptance corrections.

Figure 5.8 shows the out-of-acceptance terms for processes that produce a muon from the decay of a $W^{\pm}$ boson, calculated from simulation. As the $p_T^{\text{miss}}$ increases, the $W^{\pm}$ boson, and hence the muon, is produced more centrally and within the acceptance, resulting in a decrease in the out-of-acceptance term. The contribution from the EWK $W \to \mu\nu$ MC sample has the lowest fraction of events out-of-acceptance due to the $W^{\pm}$ boson being centrally produced in weak boson fusion events. The acceptance term from the $W \to \tau\nu$ MC sample, including EWK $W \to \tau\nu$, is much larger than the rest, and is generally larger than unity, indicating that there are more events in the signal region than in the control region. However, the effect of the $W \to \tau\nu$ MC sample on the combined acceptance correction is very small as this process is much smaller than the $W \to \mu\nu$ and $t\bar{t}$ processes after the event selection requirements.
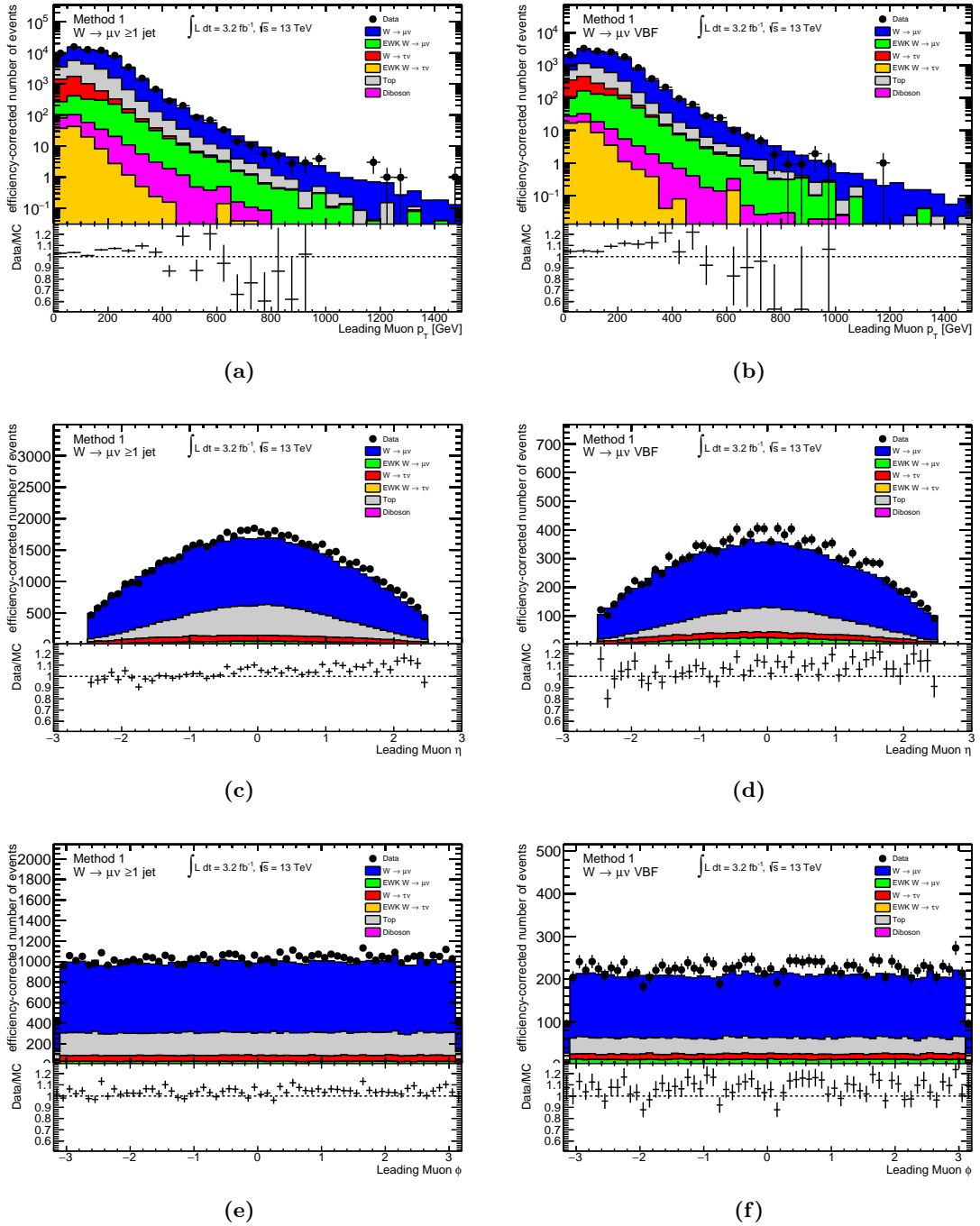
**Figure 5.6.** Lepton kinematic comparisons between data and MC in the efficiency corrected control region for events with $W \to \mu\nu$ as a function of muon $p_T$, $\eta$ and $\phi$ in (a,c,e) the $\geq 1$ jet phase space and (b,d,f) the VBF phase space.
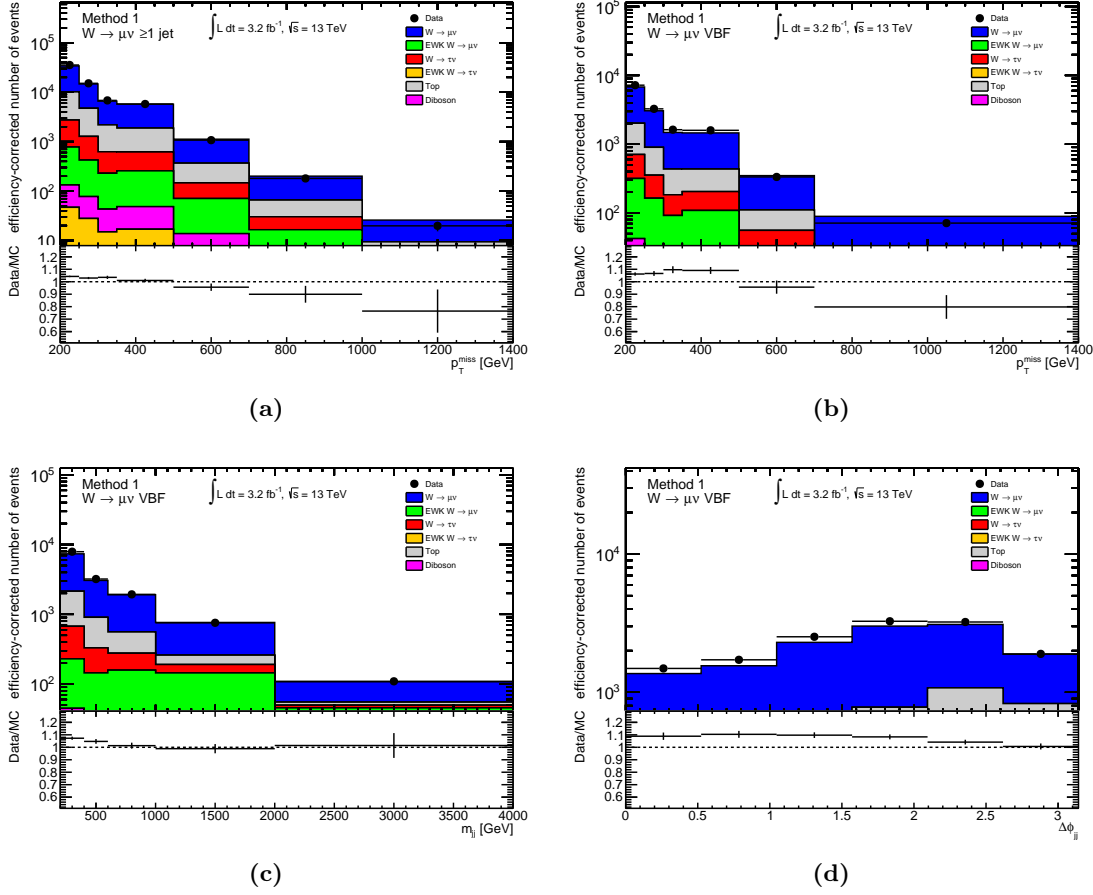
**Figure 5.7.** Comparisons between data and MC in the efficiency corrected control region for events with $W \to \mu\nu$ as a function of (a) $p_T^{\text{miss}}$ in the $\geq 1$ jet phase space and (b) $p_T^{\text{miss}}$, (c) $m_{jj}$, (d) $\Delta\phi_{jj}$ in the VBF phase space.

The in-acceptance terms for processes that produce a muon from the decay of a $W^\pm$ boson in the two phase spaces, calculated from simulation, are shown in Figure 5.9. The distributions are relatively flat and significantly smaller than the out-of-acceptance terms, due to the very high muon reconstruction and identification efficiencies. At large values of $p_T^{\text{miss}}$ the contributions from in- and out- of acceptance are comparable.

Figure 5.10 shows the data-driven background predictions for processes that produce a muon from the decay of a $W^\pm$ boson using Method 1 and Method 2 in the two phase spaces. There is a good agreement between the two methods and there are statistically significant shape differences with respect to the MC-only background, justifying the choice for a data-driven estimate.

**Figure 5.8.** Out-of-acceptance term for events with $W \to \mu\nu$ as a function of (a) $p_T^{miss}$ in the $\geq 1$ jet phase space, and (b) $p_T^{miss}$, (c) $m_{jj}$, (d) $\Delta\phi_{jj}$ in the VBF phase space. The individual out-of-acceptance terms for all MC samples used in this control region are shown, but only the terms from the combination of all samples are used in the prediction for $W \to \mu\nu$ events. The term from the $W \to \tau\nu$ sample has been scaled by 0.2. The uncertainties shown are statistical only.
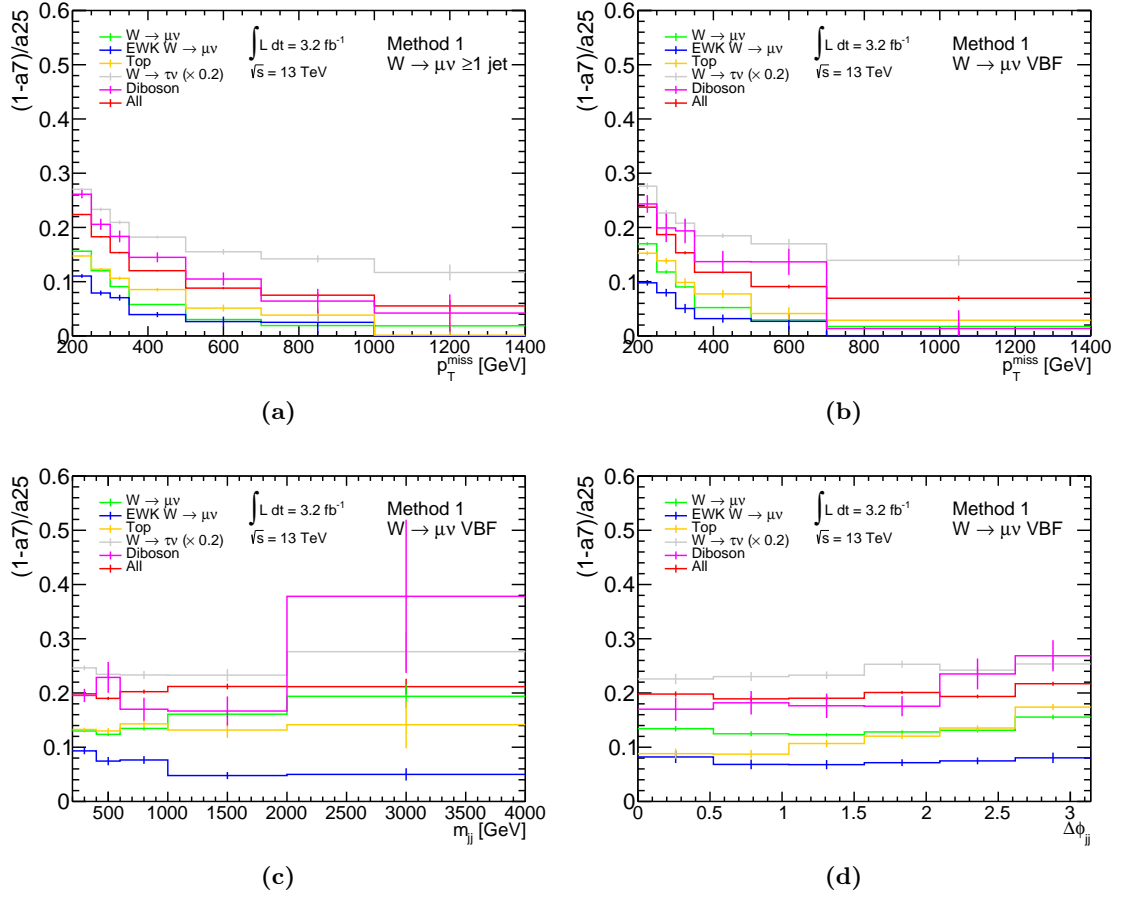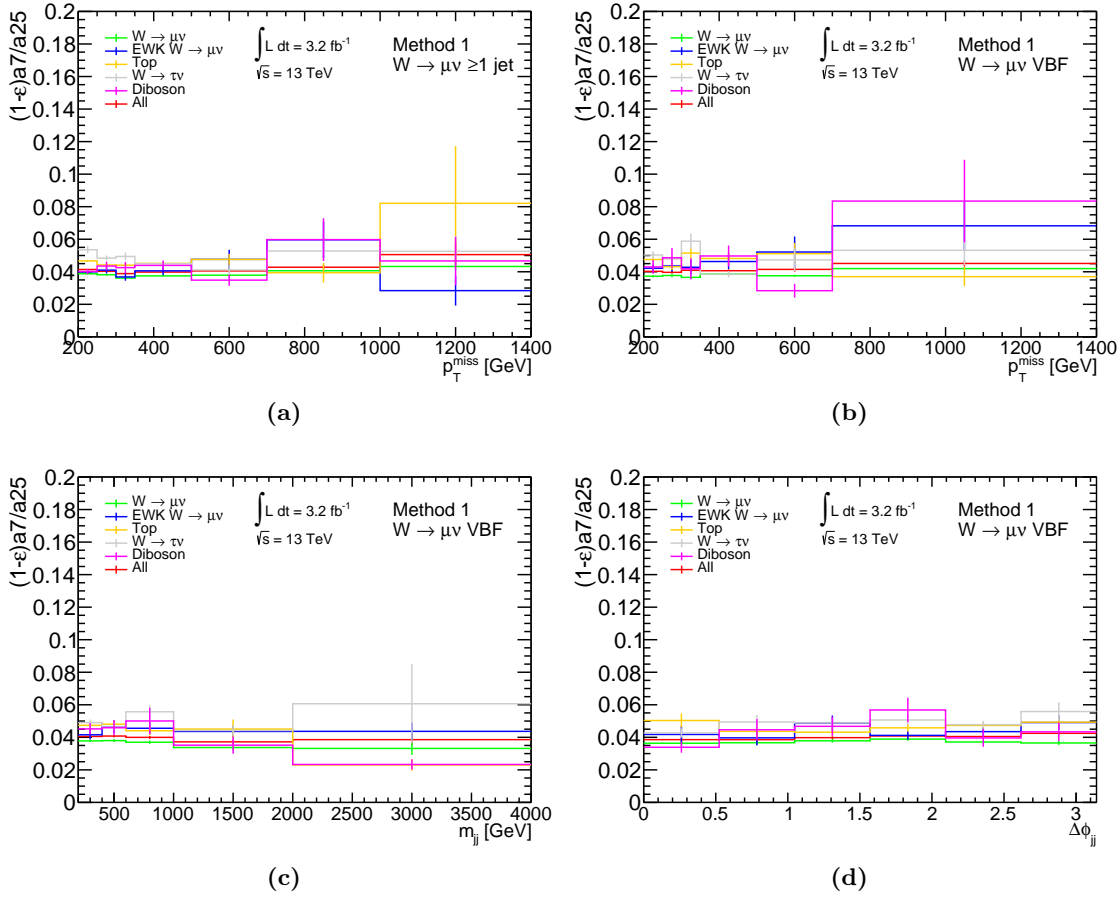
**Figure 5.9.** In-acceptance term for events with $W \to \mu\nu$ as a function of (a) $p_T^{\text{miss}}$ in the $\geq 1$ jet phase space, and (b) $p_T^{\text{miss}}$, (c) $m_{\text{jj}}$, (d) $\Delta\phi_{\text{jj}}$ in the VBF phase space. The individual in-acceptance terms for all MC samples used in this control region are shown, but only the terms from the combination of all samples are used in the prediction for $W \to \mu\nu$ events. The uncertainties shown are statistical only.
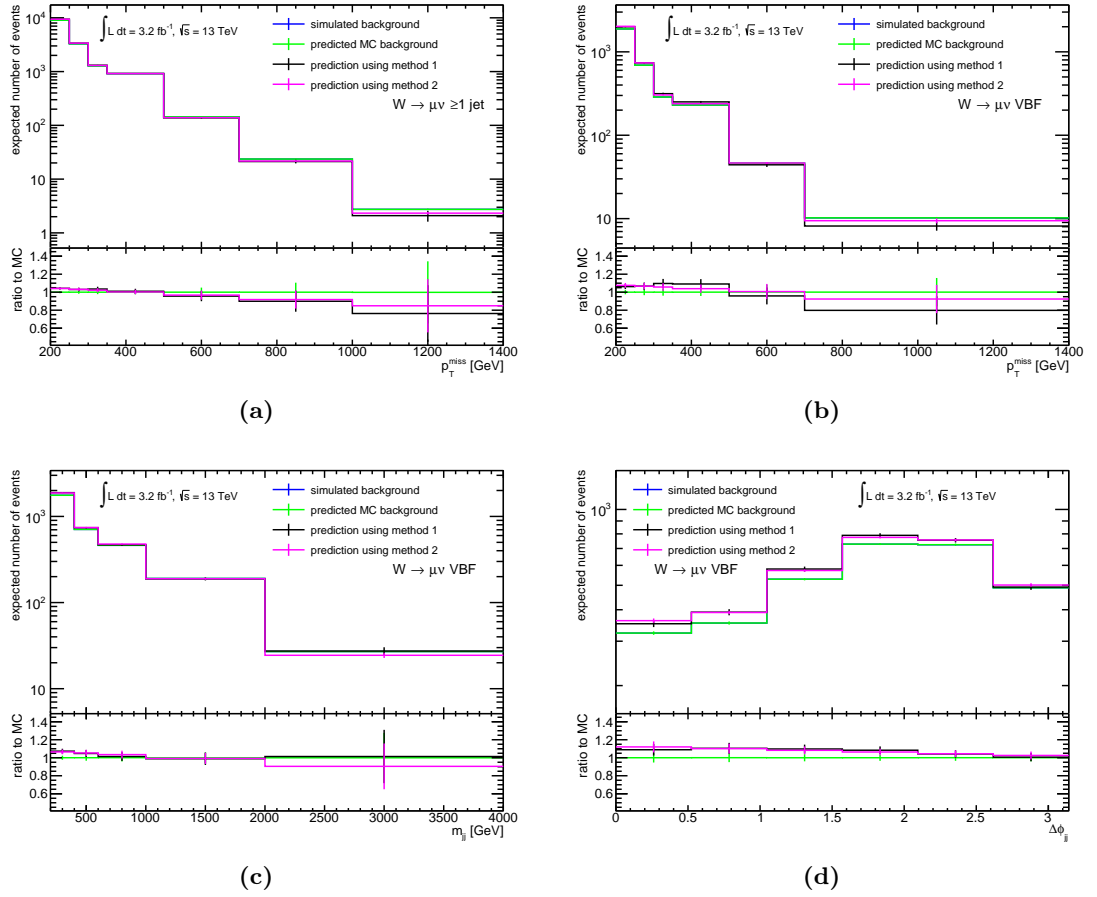
**Figure 5.10.** Data-driven background prediction for events with $W \to \mu\nu$ as a function of (a) $p_T^{\mathrm{miss}}$ in the $\geq 1$ jet phase space, and (b) $p_T^{\mathrm{miss}}$, (c) $m_{jj}$, (d) $\Delta\phi_{jj}$ in the VBF phase space. The uncertainties shown are statistical only. Simulated background is the direct output of the MC for the signal region. Predicted MC background is a closure test for Method 1 with MC only.

### 5.4.3. Background estimate for events with $W \to e\nu$

The control region used to constrain background from from processes with $W \to e\nu$ is defined to contain a single electron satisfying the *Tight* likelihood selection criteria with $p_T > 25$ GeV and no other leptons. The combination of three single electron triggers (`HLT_e24_lhmedium_L1EM20VH` || `HLT_e60_lhmedium` || `HLT_e120_lhloose`) is used to select events in this control region. The electron is again not used in the $p_T^{\text{miss}}$ calculation, however, as the electron will be reconstructed and calibrated as a jet, the $p_T^{\text{miss}}$ is not the $W^{\pm}$ boson $p_T$, but is closer to the neutrino $p_T$. This mimics the $p_T^{\text{miss}}$ reconstruction of these backgrounds in the signal region.

Contributions from processes that do not contain a prompt lepton from $W \to e\nu$ or an electron from the tau lepton decay in $W \to \tau\nu$, are estimated using the MC and subtracted from the data. The multi-jet background contribution is found to be negligible and is not subtracted from data. The difference in the electron identification working points between the signal and control regions requires the background prediction equation for Method 1 to be slightly modified, to account for tight electron efficiencies in the control region and loose in the signal region, i.e.,

$$N_{\text{background}}^{\text{Method 1}} = (1 - a_7) \frac{N_{\text{control}}^e}{\varepsilon_{\text{tight}} \cdot a_{25}} + a_7 \left(1 - \varepsilon_{\text{loose}}\right) \frac{N_{\text{control}}^e}{\varepsilon_{\text{tight}} \cdot a_{25}} \tag{5.7}$$

where $a_7$ is the fraction of events within the acceptance and electron $p_T > 7$ GeV, $a_{25}$ is the fraction of events within the acceptance and electron $p_T > 25$ GeV, $\varepsilon_{\text{tight}}$ is the average electron efficiency for the *Tight* working point, $\varepsilon_{\text{loose}}$ is the average electron efficiency for the *Loose* working point and $\frac{N_{\text{control}}}{\varepsilon_{\text{tight}}}$ is the efficiency corrected yield in the control region with electron $p_T > 25$ GeV.

Equation 5.7 will have perfect closure only if $\frac{N_7(\text{loose})}{N_7(\text{tight})} = \frac{\varepsilon_{\text{loose}}}{\varepsilon_{\text{tight}}}$, where $N_7(\text{loose})$ is the number of events with a loose electron within the acceptance and $p_T > 7$ GeV, and $N_7(\text{tight})$ is the number of events with a tight electron within the acceptance and $p_T > 7$ GeV. Some small non-closure is expected in this case due to limited MC statistics.

Efficiency-corrected distributions of electron kinematics are shown in Figure 5.11. A reasonable agreement between data and MC is observed for the electron $\eta$ and $\phi$ distributions but the electron $p_T$ distribution appears to have some mismodelling. The good agreement for electron $\eta$ implies that the in-acceptance and out-of-acceptance approach using MC is justified. The poor $p_T$ mismodelling justifies the use of Method 1 for the analysis, since it corrects for the electron efficiency on an event-by-event basis using $p_T$- and $\eta$-dependent efficiencies.
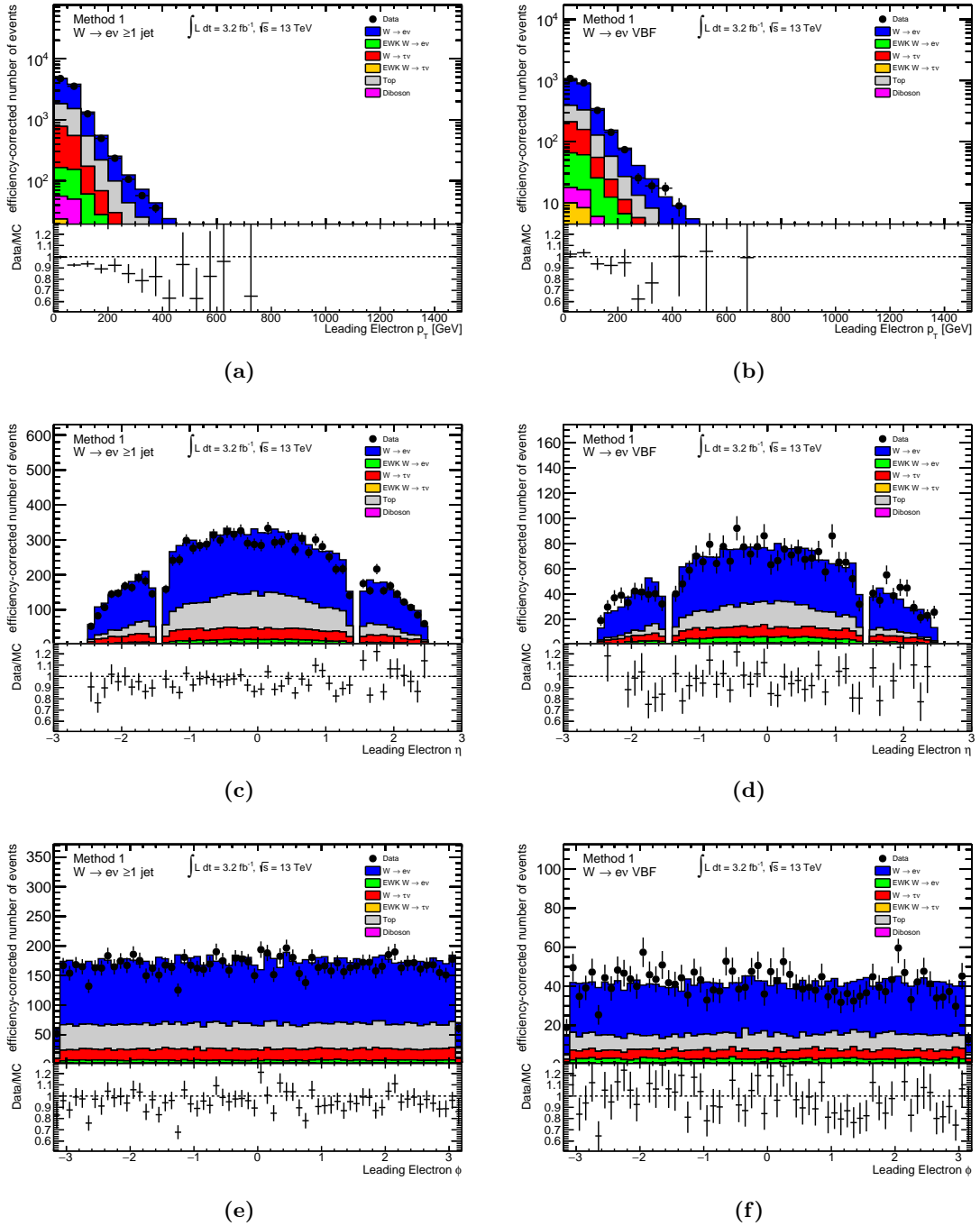
**Figure 5.11.** Lepton kinematic comparisons between data and MC in the efficiency corrected control region for events with $W \to e\nu$ as a function of electron $p_{\mathrm{T}}$, $\eta$ and $\phi$ in (a,c,e) the $\geq 1$ jet phase space and (b,d,f) the VBF phase space.
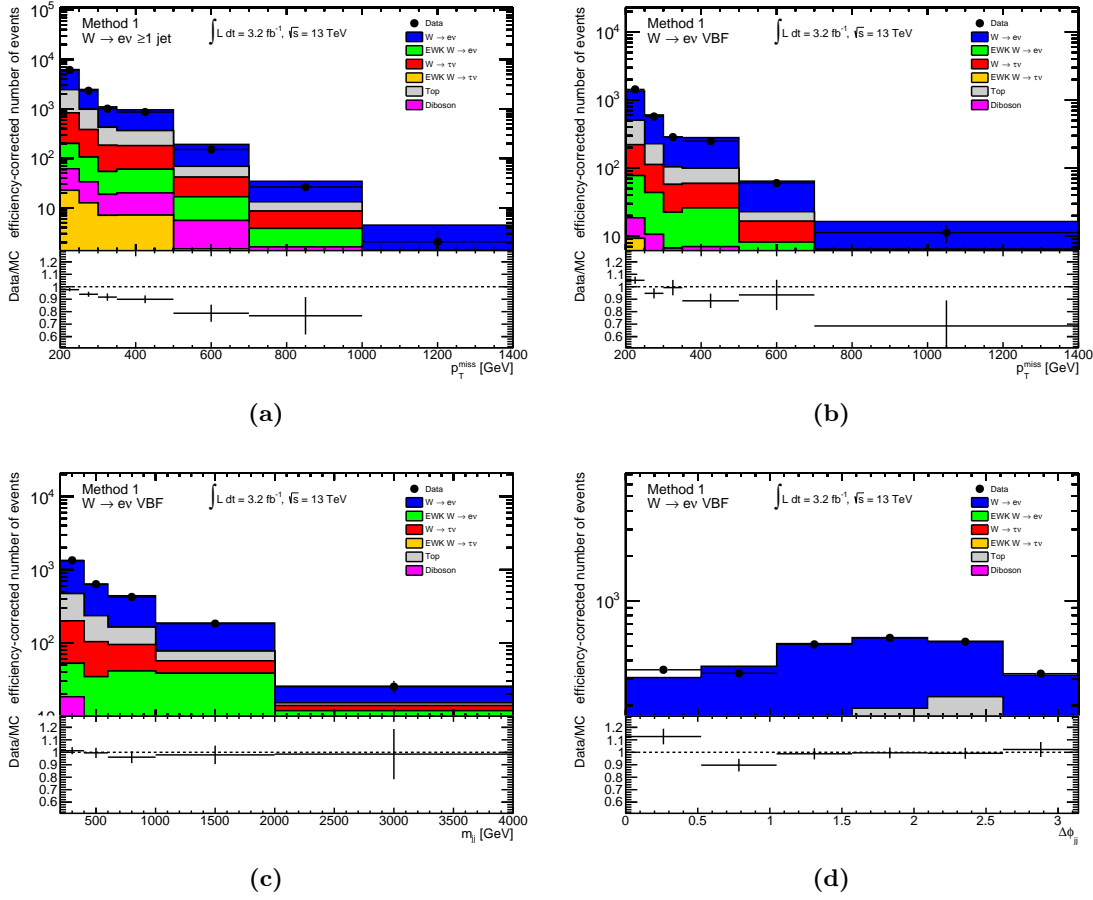
**Figure 5.12.** Comparisons between data and MC in the efficiency corrected control region for events with $W \to e\nu$ as a function of (a) $p_T^{miss}$ in the $\geq 1$ jet phase space and (b) $p_T^{miss}$, (c) $m_{jj}$, (d) $\Delta\phi_{jj}$ in the VBF phase space.

Comparisons between data and MC as a function of $p_T^{miss}$ in both phase spaces are shown in Figure 5.12. The data are typically below the MC as a function of $p_T^{miss}$ and this is different from the control region for events with $W \to \mu\nu$, due to the $p_T^{miss}$ corresponding to the neutrino $p_T$ with the electron reconstructed and calibrated as a jet, instead of the $W^{\pm}$ boson $p_T$. The dominant contribution in this region comes from the $W \to e\nu$ MC sample as expected, followed by the $t\bar{t}$ and single-top events. The $W \to \tau\nu$ contribution is significantly smaller and is less important when calculating the acceptance corrections.

Figure 5.13 shows the out-of-acceptance terms for processes that produce an electron from the decay of a $W^{\pm}$ boson in the two phase spaces. Similar conclusions can be drawn as for the events with $W \to \mu\nu$. Again, as the $p_T^{miss}$ increases, the $W^{\pm}$ boson, and hence the electron, is more central and within the acceptance, resulting in a decrease in the out-of-acceptance term. The contribution from the EWK $W \to e\nu$ MC sample has the
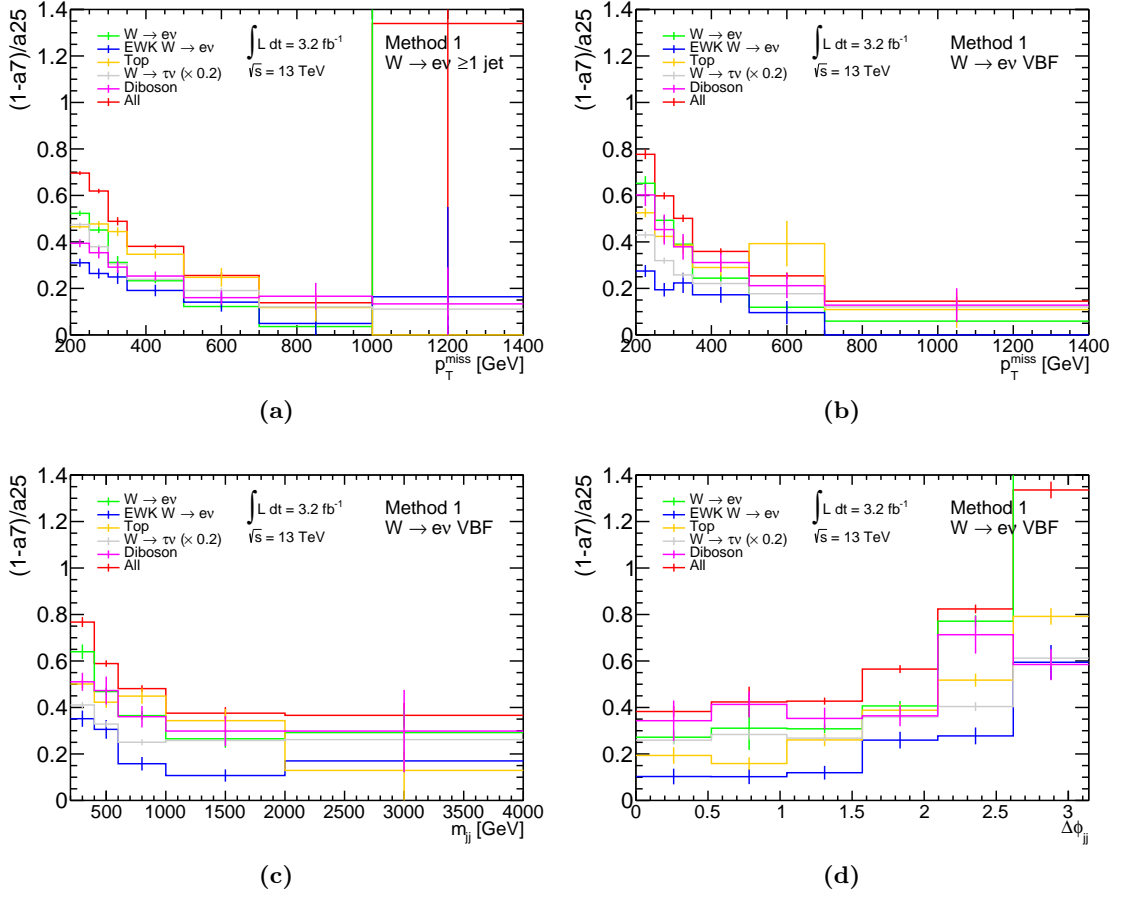
**Figure 5.13.** Out-of-acceptance term for events with $W \to e\nu$ as a function of (a) $p_T^{miss}$ in the $\geq 1$ jet phase space, and (b) $p_T^{miss}$, (c) $m_{jj}$, (d) $\Delta\phi_{jj}$ in the VBF phase space. The term from the $W \to \tau\nu$ sample has been scaled by 0.2. The uncertainties shown are statistical only.

lowest fraction of events out-of-acceptance due to the $W^{\pm}$ boson being centrally produced. The acceptance term from the $W \to \tau\nu$ MC sample, including EWK $W \to \tau\nu$, is generally larger than unity, indicating that there are more events in the signal region than the control region. The effect of the $W \to \tau\nu$ MC sample on the combined acceptance correction is very small.

The in-acceptance terms for processes that produce an electron from the decay of a $W^{\pm}$ boson in the two phase spaces are shown in Figure 5.14. The distributions are relatively flat and comparable to the out-of-acceptance terms. The larger in-acceptance term with respect to that for events with $W \to \mu\nu$ is due to the lower electron reconstruction and identification efficiencies.

**(a)**



**(b)**



**(c)**



**(d)**
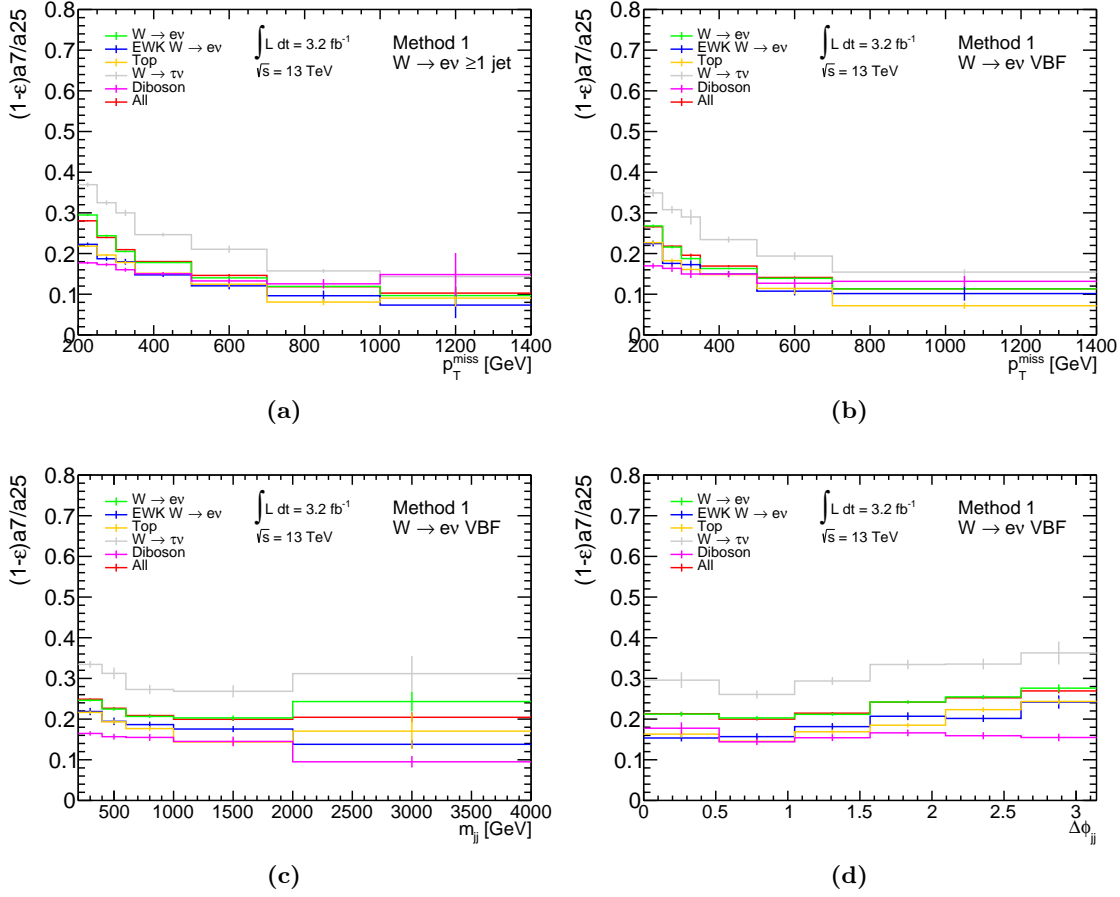
**Figure 5.14.** In-acceptance term for events with $W \to e\nu$ as a function of (a) $p_\mathrm{T}^\mathrm{miss}$ in the $\geq 1$ jet phase space, and (b) $p_\mathrm{T}^\mathrm{miss}$, (c) $m_\mathrm{jj}$, (d) $\Delta\phi_\mathrm{jj}$ in the VBF phase space. The uncertainties shown are statistical only.

Figure 5.15 shows the data-driven background predictions for processes that produce an electron from the decay of a $W^\pm$ boson using Method 1 and Method 2 in the two phase spaces. There is good agreement between the two methods and there are statistically significant differences with respect to the MC only background for the $p_\mathrm{T}^\mathrm{miss}$ distributions, justifying the choice for a data-driven estimate.

**Figure 5.15.** Data-driven background prediction for events with $W \to e\nu$ as a function of (a) $p_{\mathrm{T}}^{\mathrm{miss}}$ in the $\geq 1$ jet phase space, and (b) $p_{\mathrm{T}}^{\mathrm{miss}}$, (c) $m_{\mathrm{jj}}$, (d) $\Delta\phi_{\mathrm{jj}}$ in the VBF phase space. The uncertainties shown are statistical only. Simulated background is the direct output of the MC for the signal region. Predicted MC background is a closure test for Method 1 with MC only.

### 5.4.4. Background estimate for events with $W \to \tau\nu$

It is challenging to define a pure control region in data for the hadronic $W \to \tau\nu$ backgrounds, due to the difficulty in separating hadronically decaying tau leptons from jets. Because of this, the control regions for events with $W \to e\nu$ and $W \to \mu\nu$ are used to estimate the contribution of events with $W \to \tau\nu$. The prediction equations for Method 1 and Method 2 are modified such that the predicted number of background events with $W \to \tau\nu$ is given by

$$N_{\text{background}}^{\text{Method 1}} = \left[ (1 - a_{20}) \frac{N_{\text{control}}^{\tau,\text{MC}}}{\varepsilon \cdot a_{25}} + a_{20} (1 - \varepsilon) \frac{N_{\text{control}}^{\tau,\text{MC}}}{\varepsilon \cdot a_{25}} \right] \times \frac{N_{\text{control}}^{l}/\varepsilon^{l}}{N_{\text{control}}^{l,\text{MC}}/\varepsilon^{l,\text{MC}}} \qquad (5.8)$$

where $N_{\text{control}}^{i}$ is the number of events within the acceptance and with a leptonic object ($i = e, \mu, \tau, l = e, \mu$) with $p_{\text{T}} > 25$ GeV, $\varepsilon^{i}$ is the $p_{\text{T}}$- and $\eta$-dependent reconstruction efficiency for object i, MC labels quantities derived from simulation, and $a_x$ with $x = 20, 25$ is the fraction of events within the acceptance and a reconstructed hadronically decaying tau lepton with $p_{\text{T}} > 20$ GeV and 25 GeV respectively.

Similarly, the equation for Method 2 is

$$N_{\text{background}}^{\tau, \text{Method 2}} = \frac{N_{\text{control}}^{l}}{N_{\text{control}}^{l,\text{MC}}} \times N_{\text{background}}^{\tau,\text{MC}} \qquad (5.9)$$

where again the control regions for $W \to e\nu$ and $W \to \mu\nu$ events are used.

The predictions for events with $W \to \tau\nu$ obtained using the equations above are not strictly correct due to differences between the number of particles seen by the $p_{\text{T}}^{\text{miss}}$ calculation for $W \to \mu\nu$, $W \to e\nu$ and $W \to \tau\nu$. $W \to \tau\nu$ events contain two neutrinos and the hadronically decaying tau lepton is likely to be reconstructed as a jet. The events in the electron control region, however, contain only one neutrino, whereas the events in the muon control region ignore the muon entirely. This means that the $p_{\text{T}}^{\text{miss}}$ reconstructed in a $W \to \tau\nu$ event is somewhere between the definitions used in the electron and muon control regions. Because of this, the prediction for events with $W \to \tau\nu$ is taken as the midpoint of the two predictions obtained using the control regions for $W \to e\nu$ and $W \to \mu\nu$ events. The spread of the predictions is assigned as a systematic uncertainty due to the choice of control region.

Figure 5.16 shows the data-driven background predictions for processes that produce a hadronically decaying tau lepton from the decay of a $W^{\pm}$ boson in the two phase spaces using the control regions for events with $W \to e\nu$ and $W \to \mu\nu$ separately. The difference in the $p_{\text{T}}^{\text{miss}}$ definition between the control regions for events with $W \to e\nu$ and $W \to \mu\nu$,
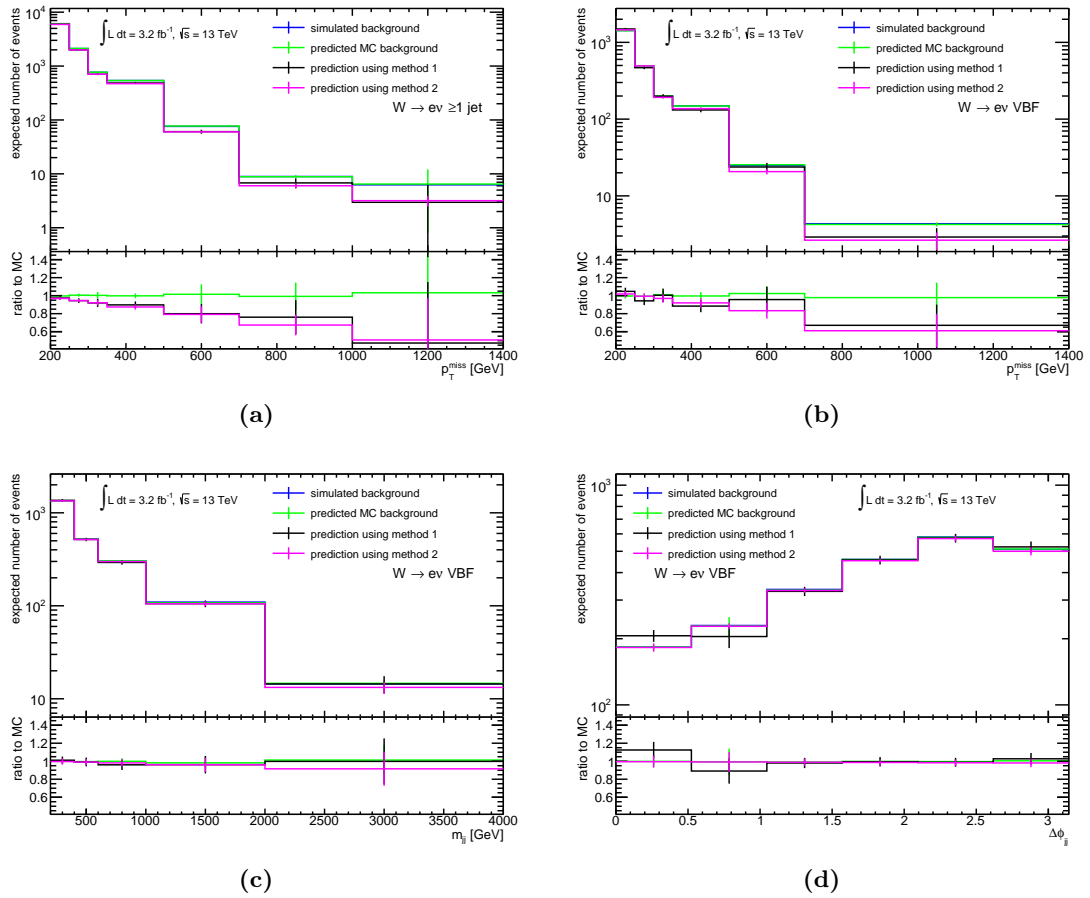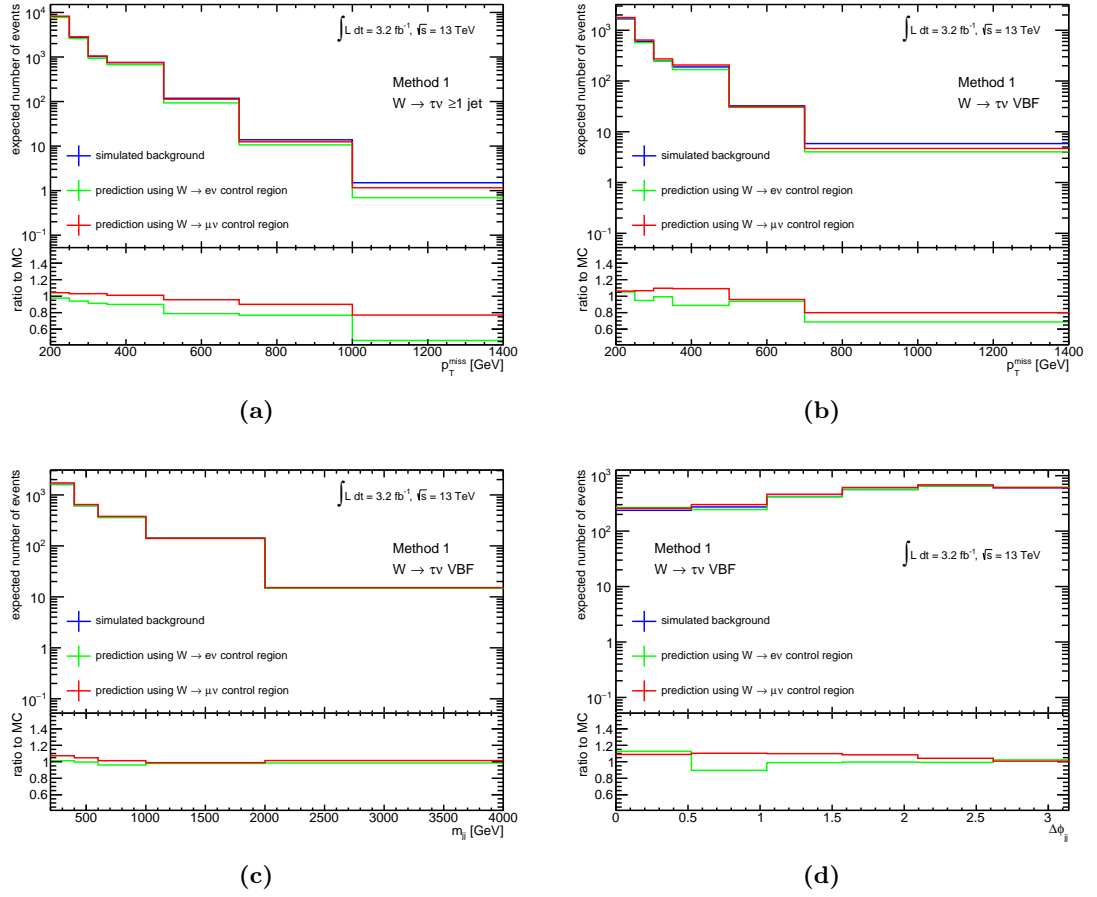
**Figure 5.16.** Choice of control region for the data-driven background prediction for events with $W \to \tau\nu$ as a function of (a) $p_T^{\text{miss}}$ in the $\geq 1$ jet phase space, and (b) $p_T^{\text{miss}}$, (c) $m_{jj}$, (d) $\Delta\phi_{jj}$ in the VBF phase space.

and the mismodelling of the simulation result in differences between the two predictions, more noticeably in the $p_T^{\text{miss}}$ distributions.

Figure 5.17 shows the data-driven background predictions for processes that produce a hadronically decaying tau lepton from the decay of a $W^\pm$ boson using Method 1 and Method 2 in the two phase spaces. There is good agreement between the two methods and there are statistically significant differences with respect to the MC background.

**(a)**

**(b)**

**(c)**

**(d)**
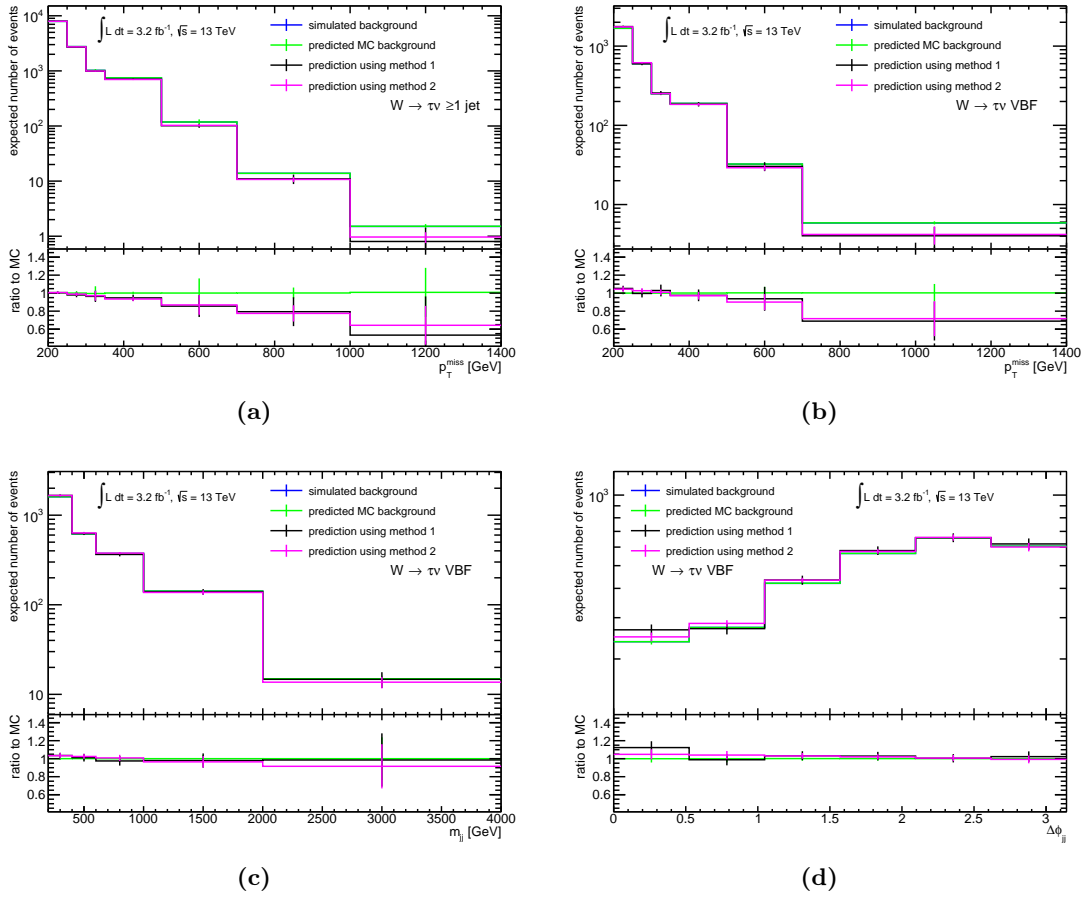
**Figure 5.17.** Data-driven background prediction for events with $W \to \tau\nu$ as a function of (a) $p_T^{\mathrm{miss}}$ in the $\geq 1$ jet phase space, and (b) $p_T^{\mathrm{miss}}$, (c) $m_{jj}$, (d) $\Delta\phi_{jj}$ in the VBF phase space. Simulated background is the direct output of the MC for the signal region. Predicted MC background is a closure test for Method 1 with MC only.

### 5.4.5. Cross-checks of the $W^{\pm} + \mathrm{jets}$ background predictions

Several cross-checks are performed to ensure the data-driven background estimates are accurate. Figure 5.18 shows the closure test of the background prediction for events with $W \to \mu\nu$ using Method 1 with all terms in the equation taken from the MC. This is a purely technical check of the self-consistency of the method. The background prediction for events with $W \to \mu\nu$, and also the prediction for events with $W \to \tau\nu$, which is not shown here, have perfect closure as expected. The background prediction for events with $W \to e\nu$ has a small non-closure due to statistical fluctuations in the signal and the control regions which differ in electron identification working points.
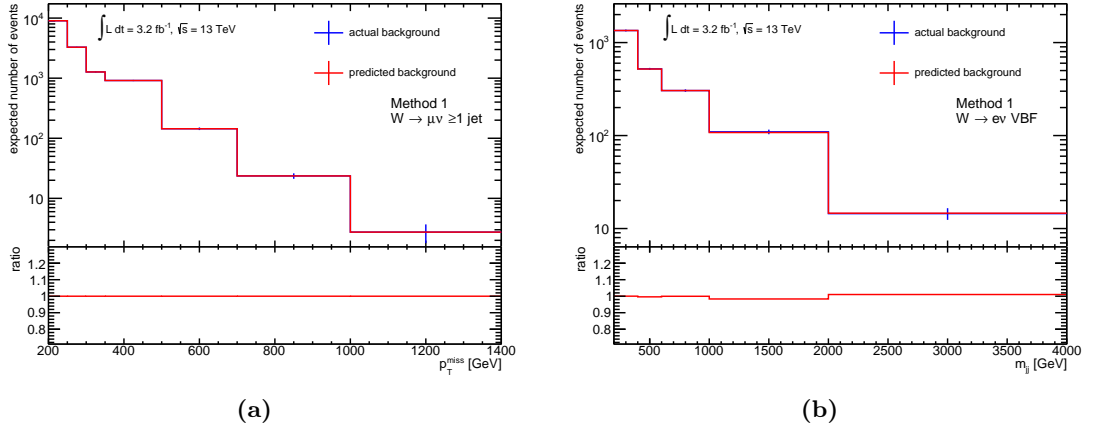


|              | (a)         |              | (b)         |

**Figure 5.18.** Closure of (a) the background prediction for events with $W \to \mu\nu$ as a function of $p_{\mathrm{T}}^{\mathrm{miss}}$ in the $\geq 1$ jet phase space and (b) the background prediction for events with $W \to e\nu$ as a function of $m_{\mathrm{jj}}$ in the VBF phase space. 'Actual background' is the direct output of the MC in the signal region and 'predicted background' is the prediction using Equation 5.4 with all terms from the MC. The predicted background contains no uncertainties for this test.

The prediction for the out-of-acceptance part of the $W^{\pm} + \mathrm{jets}$ backgrounds relies on the correct $\eta$-modelling in the MC. This is validated using a data-driven approach. The control regions in both data and MC are split into lepton $|\eta| < 1.0$ and $|\eta| > 1.0$. The control region with $|\eta| < 1.0$ is used to predict the data with $|\eta| > 1.0$ using Method 2. The advantage of this approach is that the prediction can be compared to the observed data to check the agreement. There is a good agreement between the predictions and the actual data within the statistical uncertainties, as shown in Figure 5.19.

The backgrounds are also estimated using the MADGRAPH5_aMC@NLO and SHERPA v2.1.1 $W^{\pm} + \mathrm{jets}$ samples, instead of the default SHERPA v2.2.0 samples. The differences between SHERPA v2.2.0 and SHERPA v2.1.1 are typically larger than the differences
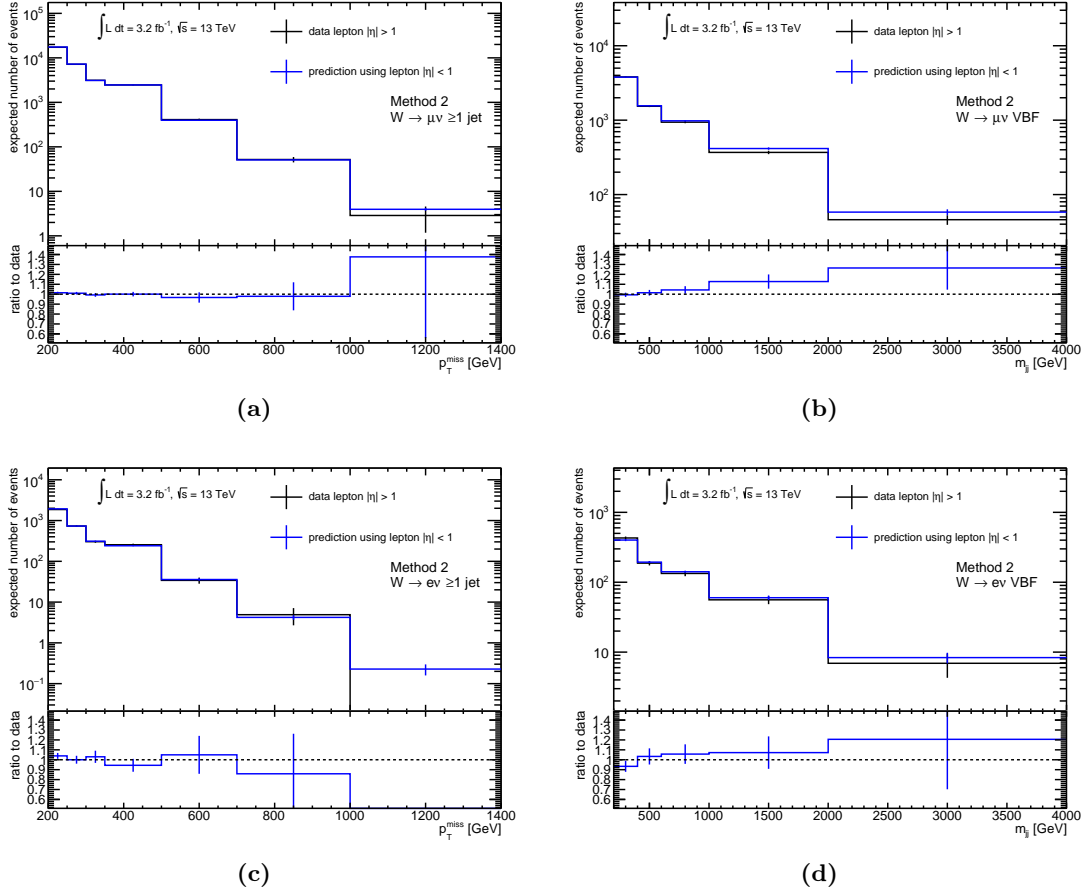
**Figure 5.19.** Validation of the predictions using events with (a,b) $W \to \mu\nu$ and (c,d) $W \to e\nu$ as a function of (a,c) $p_T^{miss}$ in the $\geq 1$ jet phase space and (b,d) $m_{jj}$ in the VBF phase space.

SHERPA v2.2.0 and MADGRAPH5_aMC@NLO as shown in Figure 5.20. The background predictions using SHERPA v2.1.1 are used as an additional systematic uncertainty.

Top-enhanced control regions are defined for the control regions with $W \to \mu\nu$ and $W \to e\nu$ events in order to check if the MC simulation of top-quark events is accurate in the phase spaces used in the analysis. Requirements on the presence of $b$-jets are made in addition to the baseline cuts. A $b$-jet is defined as a jet with $p_T > 30$ GeV, $|\eta| < 2.5$ and MV2c20 discriminant $> -0.0436$, corresponding to the 70% identification efficiency working point [208]. The MV2c20 algorithm is a BDT algorithm used to discriminate $b$-jets from light jets and $c$-jets. Top-enhanced control regions for events with $W \to \mu\nu$ and $W \to e\nu$ requiring $\geq 1$ or $\geq 2$ $b$-jets are selected and the results are shown in Figure 5.21. The data and MC agreement in these plots is reasonable. A 30% uncertainty is applied to the
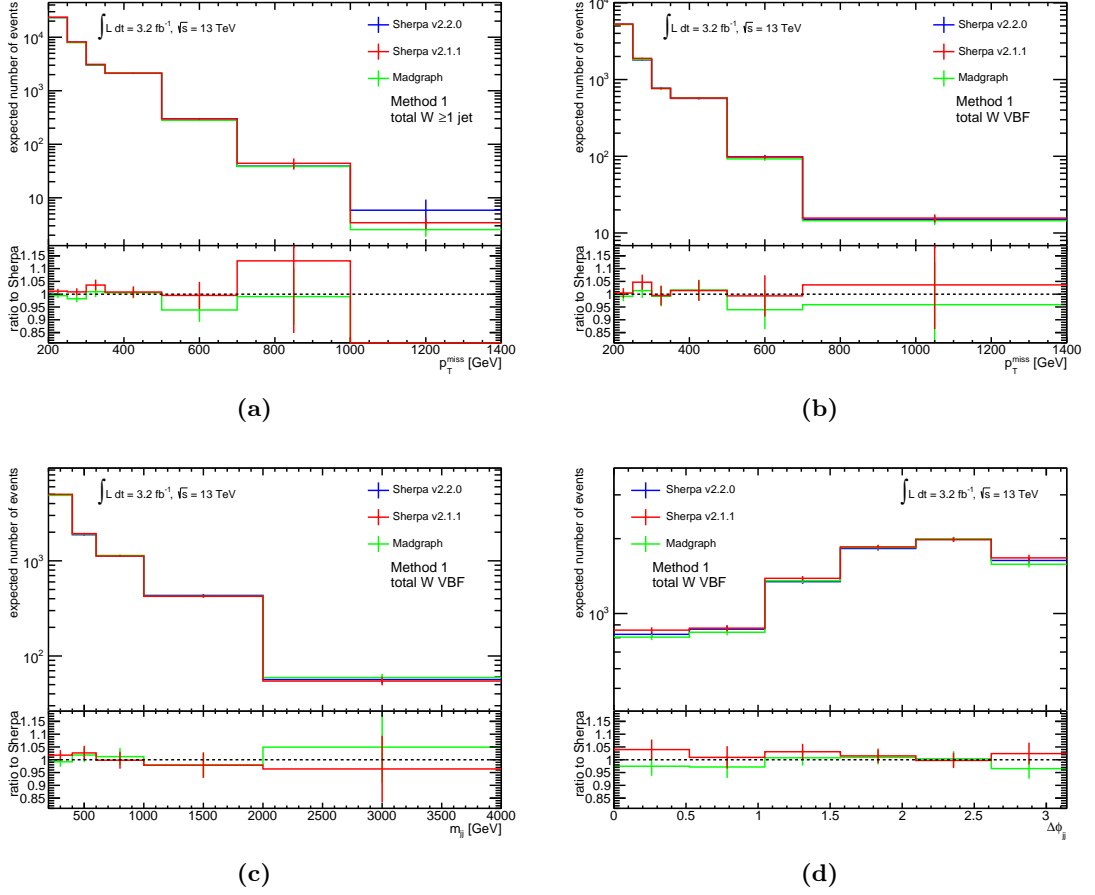
**Figure 5.20.** Comparison of the total $W^{\pm}$ + jets background prediction using Method 1 with the MadGraph5_aMC@NLO and Sherpa v2.1.1 samples as a function of (a) $p_T^{\text{miss}}$ in the $\geq 1$ jet phase space, and (b) $p_T^{\text{miss}}$, (c) $m_{\text{jj}}$, (d) $\Delta\phi_{\text{jj}}$ in the VBF phase space.

top cross-section and used a systematic uncertainty in all three $W^{\pm}$ + jets background predictions.

Cross-checks to check the impact of pileup are also performed. The control and signal regions in both data and MC are split into low ($\langle\mu\rangle < 10$), medium ($10 < \langle\mu\rangle < 12$) and high ($\langle\mu\rangle > > 12$) average number of interactions per bunch crossing. Figure 5.22 shows cross-checks as a function of $p_T^{\text{miss}}$ in the $\geq 1$ jet phase space for events with $W \rightarrow \mu\nu$ and $W \rightarrow e\nu$, including the ratio of signal to control region in data and the ratio of low to medium $\langle\mu\rangle$ and high to medium $\langle\mu\rangle$ normalised to unity in both data and MC. No statistically significant difference is seen between the three regions of $\langle\mu\rangle$ and similar dependencies are observed in data and MC. Similar results are also observed in the VBF phase space, but with less statistics and larger uncertainties.

(a)

(b)

(c)

(d)
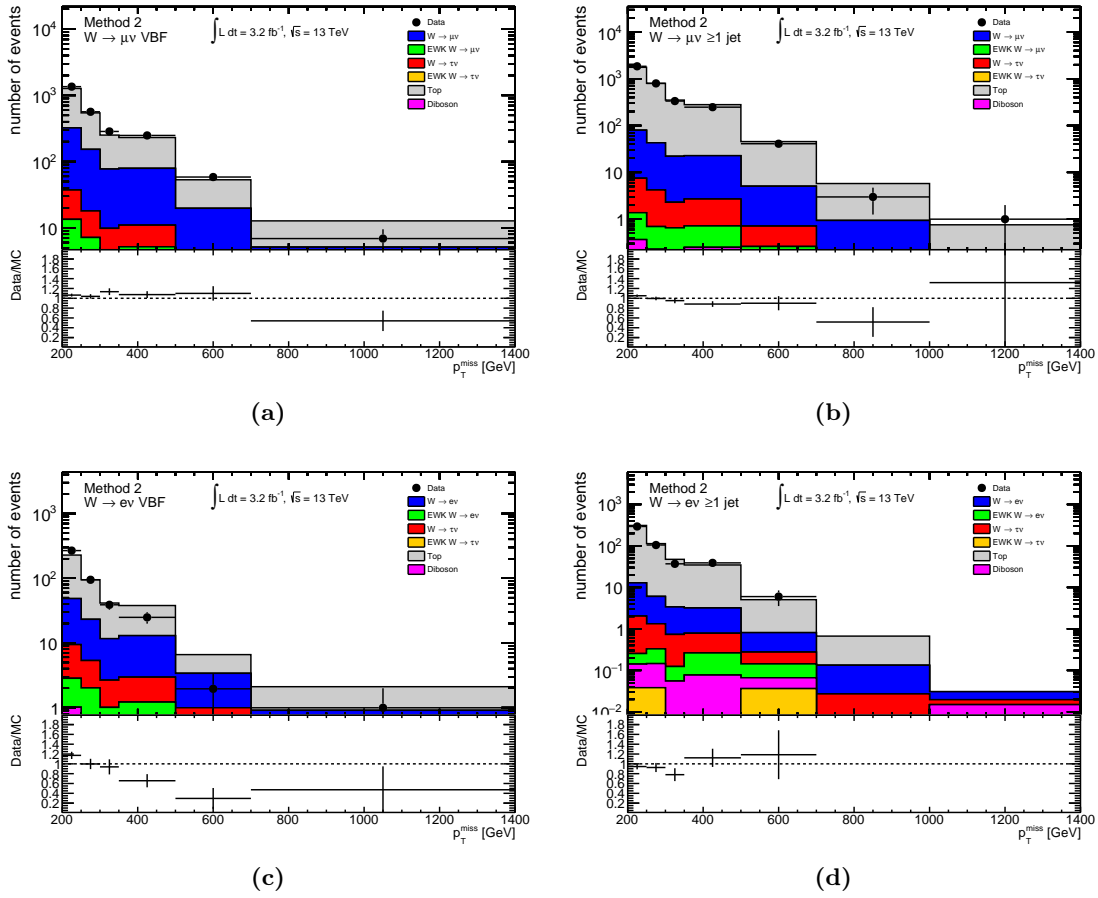
**Figure 5.21.** Top enhanced control region for events with $W \to \mu\nu$ requiring (a) $\geq 1$ b-jets as a function of $p_T^{miss}$ in the VBF phase space and (b) $\geq 2$ b-jets as a function of $p_T^{miss}$ in the $\geq 1$ jet phase space. Top-enhanced control region for events with $W \to e\nu$ requiring (c) $\geq 1$ b-jets as a function of $p_T^{miss}$ in the VBF phase space and (d) $\geq 2$ b-jets as a function of $p_T^{miss}$ in the $\geq 1$ jet phase space.
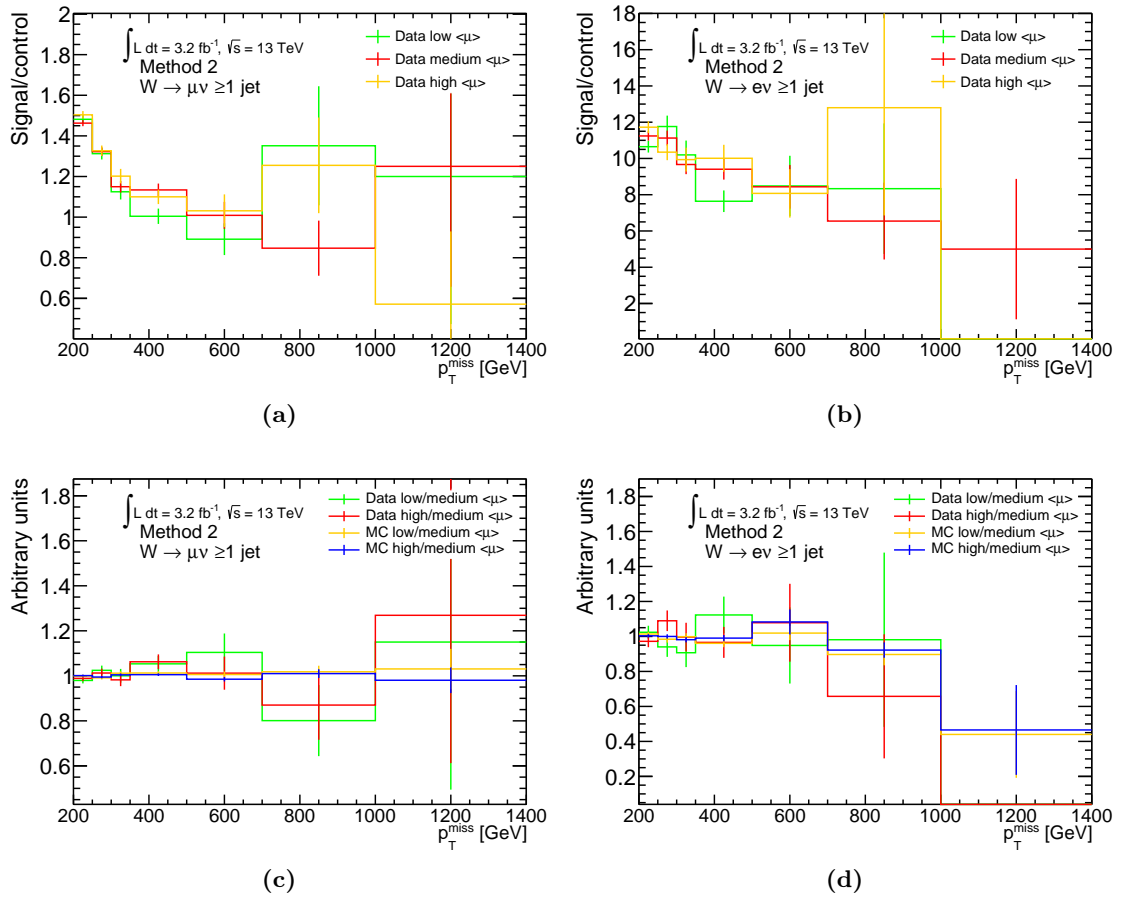
**Figure 5.22.** Control and signal regions for events with $W \to \mu\nu$ and $W \to e\nu$ split into low, medium and high $\langle\mu\rangle$ as a function of $p_{\mathrm{T}}^{\mathrm{miss}}$ in the $\geq 1$ jet phase space. Ratio of signal to control region in data for the control regions for events with (a) $W \to \mu\nu$ and (b) $W \to e\nu$. Ratios of low to medium $\langle\mu\rangle$ and high to medium $\langle\mu\rangle$ normalised to unity in both data and MC for the control regions for events with (c) $W \to \mu\nu$ and (d) $W \to e\nu$.

### 5.4.6. Systematic uncertainties

The systematic uncertainties on the $W^{\pm}+$jets data-driven background estimates are separated into experimental and theoretical components. Every object calibration, energy scale, energy resolution or efficiency procedure has an associated experimental systematic uncertainty which corresponds to differences between the performance in data and simulation. The impact of these uncertainties, estimated by varying the object calibration or SF by one standard deviation around the nominal value is determined by the relevant ATLAS performance groups. The uncertainties in the background prediction associated with $p_{\mathrm{T}}^{\mathrm{miss}}$ and lepton calibration and resolution are found to negligible. The uncertainty on the lepton calibration shifts the lepton $p_{\mathrm{T}}$ by a small amount and this only affects the lepton veto or lepton selection. Jets are used in many different cuts and selections, and the JES uncertainties change the jet momentum causing events to either pass or fail the various criteria. The JES uncertainties are small but not negligible, whereas the jet energy resolution uncertainties are negligible. The dominant experimental uncertainties on each of the three $W \to l\nu$ channels are the uncertainties associated with the lepton efficiencies. For events with $W \to \mu\nu$ these are the uncertainties on the muon reconstruction and isolation SFs applied to the MC. For events with $W \to e\nu$ these are the uncertainties on electron reconstruction, identification, isolation and trigger SFs, and also the statistical uncertainties on the calculated electron efficiencies. For events with $W \to \tau\nu$ these are the uncertainties on the hadronically decaying tau lepton reconstruction, identification and electron overlap removal SFs.

The dominant theoretical uncertainties arise from the variations of the factorisation, renormalisation and resummation scales, each scale varied by factors of 0.5 and 2, and the CKKW matching scale between 15 GeV and 30 GeV, with the nominal being 20 GeV. The PDF uncertainties are smaller but also included. They are derived from the nominal NNPDF3.0nnlo PDF set [180] and the MMHT2014nnlo [209] and CT14nnlo [210] PDF sets using their recommended PDF uncertainty prescription. A small uncertainty from the value used for the strong coupling constant, $\alpha_{\mathrm{s}}$, is also included, derived from up and down variations of 0.117 and 0.119, respectively, with the nominal value being 0.118. A combined PDF uncertainty is obtained from the envelope [211] of the three PDF sets and their respective uncertainties, which include the uncertainty on the strong coupling constant.

Additional systematic uncertainties include the uncertainty from the multi-jet background estimation in the control region for events with $W \to \mu\nu$, the uncertainty from the choice of control region used to normalise the prediction for events with $W \to \tau\nu$, and the uncertainty from the variation of top MC sample cross-sections by 30%. The difference in

**Figure 5.23.** Systematic uncertainties on the data-driven background prediction for events with $W \to \mu\nu$ as a function of (a) $p_T^{\mathrm{miss}}$ in the $\geq 1$ jet phase space, and (b) $p_T^{\mathrm{miss}}$, (c) $m_{\mathrm{jj}}$, (d) $\Delta\phi_{\mathrm{jj}}$ in the VBF phase space.

the $W^\pm$ + jets background prediction when using SHERPA v2.1.1 instead of SHERPA v2.2.0 is also assigned as a systematic uncertainty.

The systematic uncertainties on the data-driven background prediction for events with $W \to \mu\nu$ grouped by source of uncertainty are shown in Figure 5.23. The dominant uncertainties are from the muon SFs ranging from 5% at low $p_T^{\mathrm{miss}}$ to 35% at high $p_T^{\mathrm{miss}}$ in the $\geq 1$ jet phase space. The increase with $p_T^{\mathrm{miss}}$ is due to the increasing importance of the in-acceptance events.

Figure 5.24 shows the systematic uncertainties on the the data-driven background prediction for events with $W \to e\nu$. Similar to the background prediction for events with $W \to \mu\nu$, the dominant uncertainties are from the electron SFs and efficiencies ranging from 7% at low $p_T^{\mathrm{miss}}$ to 15% at high $p_T^{\mathrm{miss}}$ in the $\geq 1$ jet phase space, with the remaining
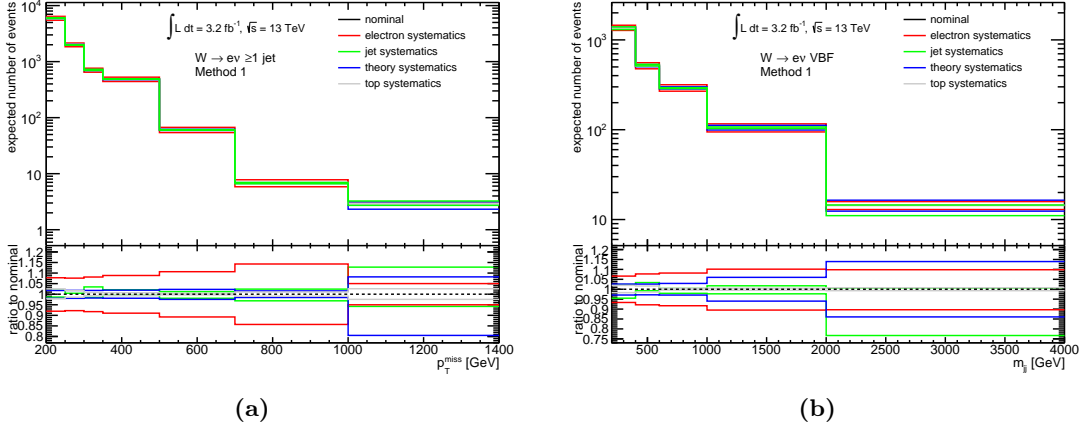
**Figure 5.24.** Systematic uncertainties on the data-driven background prediction for events with $W \to e\nu$ as a function of (a) $p_T^{\text{miss}}$ in the $\geq 1$ jet phase space, and (b) $m_{jj}$ in the VBF phase space.



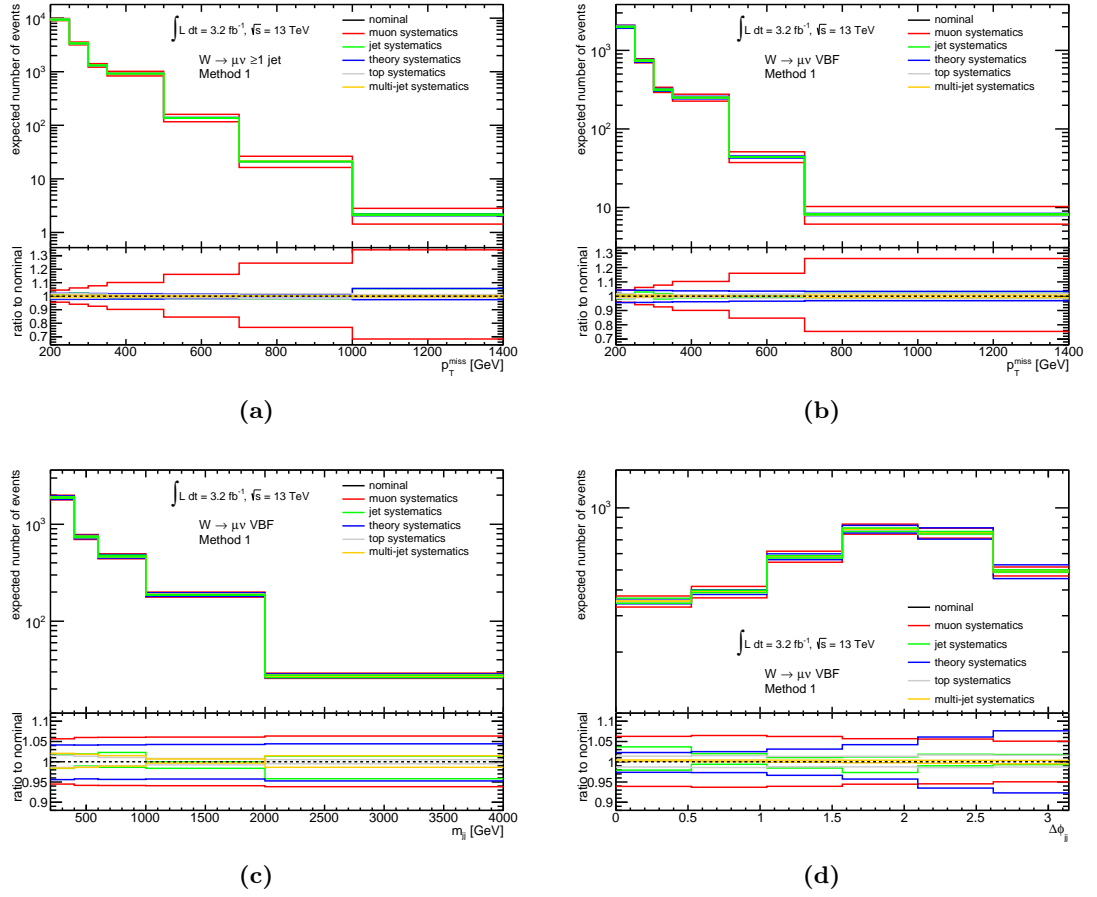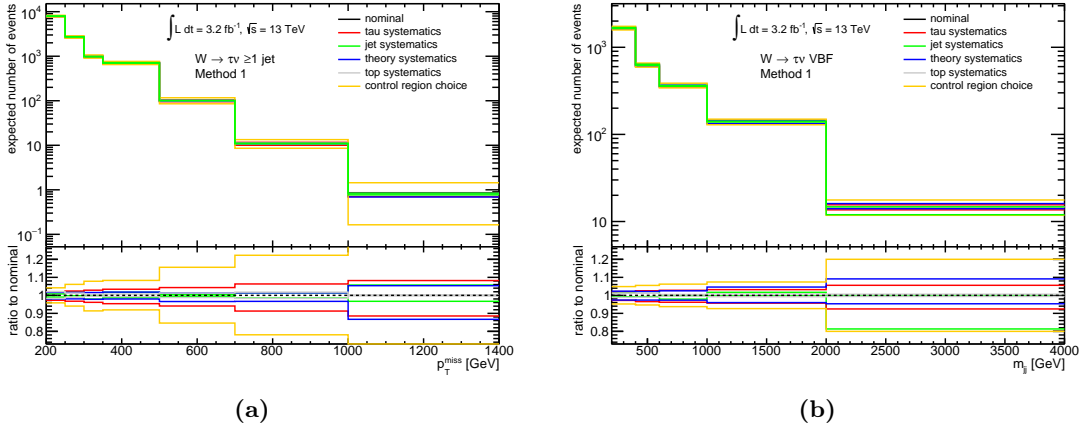**Figure 5.25.** Systematic uncertainties on the data-driven background prediction for events with $W \to \tau\nu$ as a function of (a) $p_T^{\text{miss}}$ in the $\geq 1$ jet phase space, and (b) $m_{jj}$ in the VBF phase space.

uncertainties being smaller. The last bin at large $p_T^{\text{miss}}$ shows statistical fluctuations from the jet and theory systematics due to limited statistics.

Figure 5.25 shows the systematic uncertainties on the data-driven background prediction for events with $W \to \tau\nu$. The dominant uncertainty in this case is from the choice of control region used to normalise the prediction, ranging from 5% at low $p_T^{\text{miss}}$ to more than 30% at high $p_T^{\text{miss}}$ in the $\geq 1$ jet phase space. The uncertainties from the tau lepton SFs are also important ranging from 2% at low $p_T^{\text{miss}}$ to more 9% at high $p_T^{\text{miss}}$, with the remaining uncertainties being very small. The last bin at large $p_T^{\text{miss}}$ shows statistical fluctuations from the jet and theory systematics due to limited statistics.

### 5.4.7. The $p_\mathrm{T}^\mathrm{miss}$ + jets numerator results

Detector-level comparisons of data and MC simulation of $Z \to \nu\bar{\nu}$ events and estimated backgrounds in the $\geq 1\,\mathrm{jet}$ and VBF phase spaces are shown in Figure 5.26. The data are typically larger than the MC prediction plus the estimated backgrounds, however, they are consistent within the total statistical and systematic uncertainties. The systematic uncertainties on the MC predictions include JES, theory, lepton SF uncertainties, and the additional systematic uncertainties discussed in Section 5.4.6. The dominant systematic uncertainty component is due to the theoretical modelling uncertainties of the $Z \to \nu\bar{\nu}$ MC sample. Statistical uncertainties due to the finite size of the MC samples are included in the shaded bands.

The number of observed events in the signal region and the SM predictions including the individual contributions, are summarised in Table 5.2. Both the statistical and systematic uncertainties are included in the SM predictions. The three $W \to l\nu$ channels contribute approximately 18%, 12%, and 15% to the event yield for $W \to \mu\nu$, $W \to e\nu$ and $W \to \tau\nu$ events, respectively. The contribution of the three channels depends on the lepton veto criteria and $p_\mathrm{T}^\mathrm{miss}$ definitions.

| **Signal region** | $\geq 1\,\mathrm{jet}$ phase space | VBF phase space |
|---|---:|---:|
| Observed events ($3.2\,\mathrm{fb}^{-1}$) | 87654 | 20091 |
| SM prediction | $82901 \pm 7915$ | $18579 \pm 1428$ |
| $Z \to \nu\bar{\nu}$ MC | $44146 \pm 7715$ | $9608 \pm 1356$ |
| $W \to \mu\nu$ | $15189 \pm 1006$ | $3355 \pm 256$ |
| $W \to e\nu$ | $9213 \pm 823$ | $2319 \pm 225$ |
| $W \to \tau\nu$ | $12471 \pm 863$ | $2837 \pm 223$ |
| Multi-jet | $1257 \pm 668$ | $320 \pm 173$ |
| $Z \to \ell^+\ell^-$ MC | $626 \pm 9$ | $140 \pm 3$ |

**Table 5.2.** Number of events in the signal region of the $p_\mathrm{T}^\mathrm{miss}$ + jets numerator for the $\geq 1\,\mathrm{jet}$ and VBF phase spaces. The combined statistical and systematic uncertainties are also included. The $W^\pm$ + jets number of events are the data-driven estimates using Method 1. The multi-jet background is predicted using the jet smearing method, whereas the $Z \to \nu\bar{\nu}$ and $Z \to \ell^+\ell^-$ events are the MC predictions for $3.2\,\mathrm{fb}^{-1}$.

Figure 5.27 shows comparisons between data and background-subtracted SM prediction of $p_\mathrm{T}^\mathrm{miss}$ + jets events. The backgrounds from Figure 5.26 are subtracted from the data and
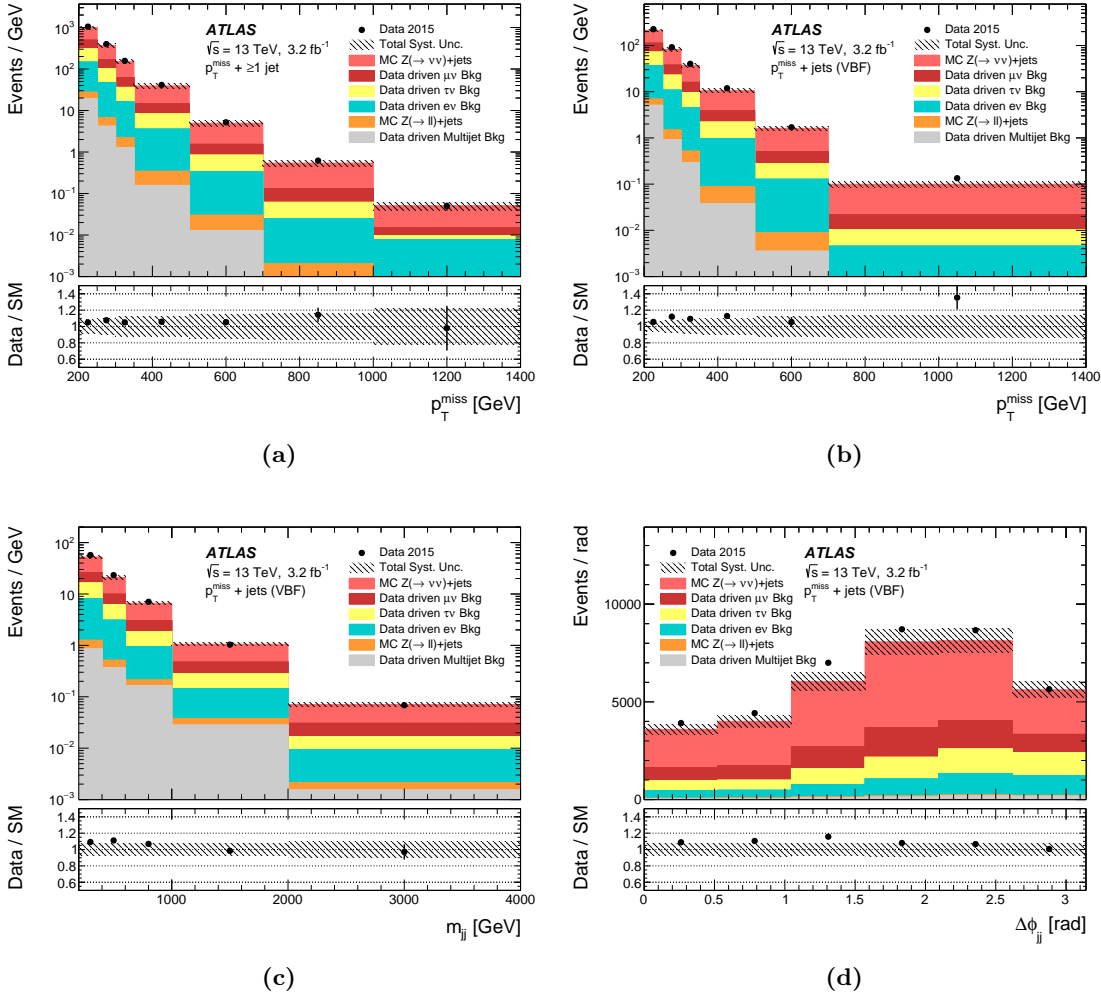
**Figure 5.26.** Comparisons between data and SM prediction of $p_{\mathrm{T}}^{\mathrm{miss}}$ + jets events plus predicted backgrounds as a function of (a) $p_{\mathrm{T}}^{\mathrm{miss}}$ in the $\geq 1$ jet phase space, and (b) $p_{\mathrm{T}}^{\mathrm{miss}}$, (c) $m_{\mathrm{jj}}$, (d) $\Delta\phi_{\mathrm{jj}}$ in the VBF phase space. Statistical uncertainties on the data are shown as error bars and the total combined statistical and systematic uncertainties on the backgrounds are shown as shaded bands.

the result is compared to the $Z \to \nu\bar{\nu}$ MC prediction. The dominant systematic uncertainty is from the theoretical systematics of the $Z \to \nu\bar{\nu}$ MC sample, reaching almost 20%. These measurements could be unfolded to particle level and used to set limits on BSM models, however, the large theoretical uncertainty would be a limiting factor. The construction of the ratio $R^{\mathrm{miss}}$ almost eliminates this theoretical uncertainty and will be discussed in Section 5.6.

**(a)**

**(b)**

**(c)**

**(d)**
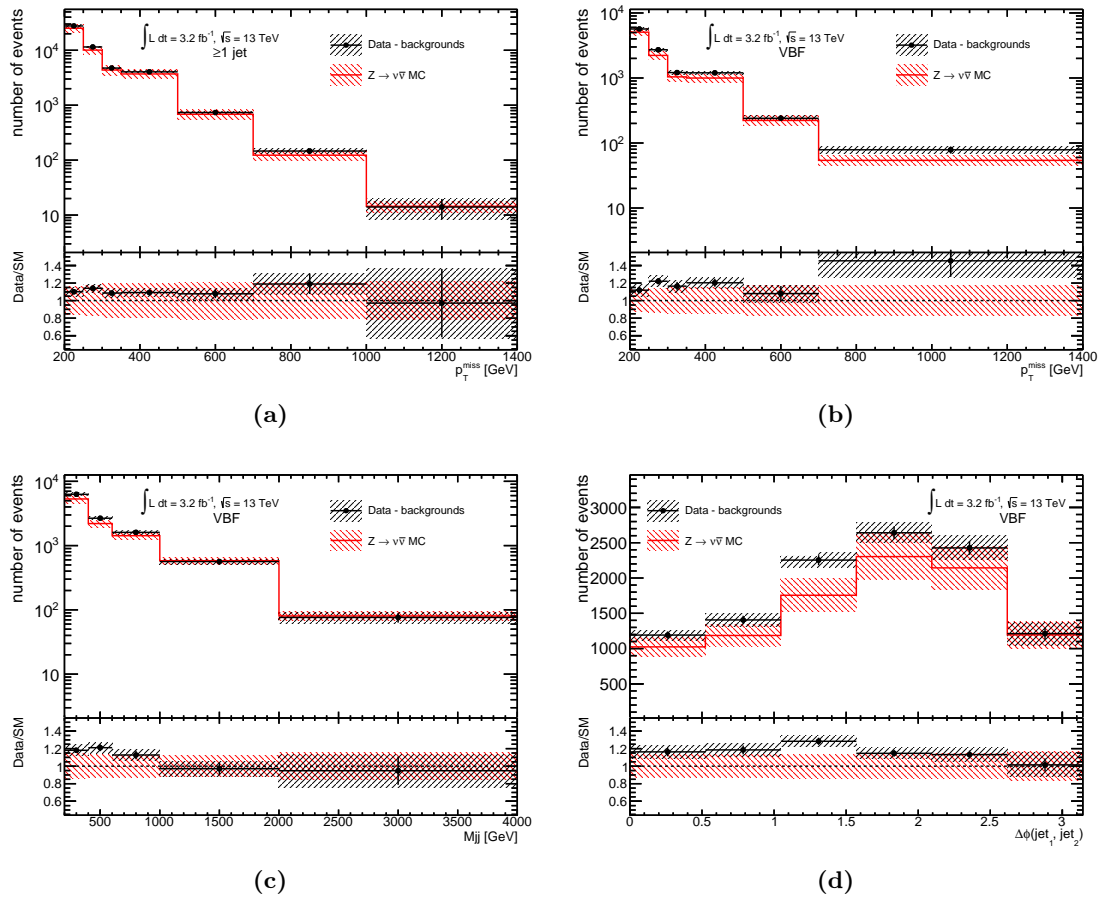
**Figure 5.27.** Comparisons between data minus predicted backgrounds and MC simulation of $Z \to \nu\bar{\nu}$ events as a function of (a) $p_T^{\text{miss}}$ in the $\geq 1$ jet phase space, and (b) $p_T^{\text{miss}}$, (c) $m_{\text{jj}}$, (d) $\Delta\phi_{\text{jj}}$ in the VBF phase space. Statistical uncertainties are shown as error bars and the total combined statistical and systematic uncertainties are shown as shaded bands.

## 5.5. The $\ell^+\ell^- +$ jets denominator and detector corrections

The dominant background to the $\ell^+\ell^- +$ jets denominator is due to top-quark events, with smaller contributions from diboson, $W^\pm +$ jets, and $Z \to \tau^+\tau^-$ events. A control region is defined for a data-driven estimation of these backgrounds using the same selection with the exception of requiring an opposite flavour lepton pair ($e^+\mu^-$ or $e^-\mu^+$). This removes the contribution from $\ell^+\ell^-$ events which come from $Z$ bosons and enhances the contribution from background events. Comparisons of data and MC in this control region show discrepancies of up to 50%. The data-driven estimate is determined using Method 2, as defined for the $W^\pm +$ jets backgrounds in the $p_T^{\text{miss}}$ numerator in Section 5.4.1. The difference between the data-driven estimate and the MC-only backgrounds is assigned as a systematic uncertainty.

The dominant experimental systematic uncertainties in the $\ell^+\ell^- +$ jets denominator are due to the lepton efficiencies, namely the muon reconstruction SFs and the electron reconstruction, identification, isolation and trigger SFs. Subdominant uncertainties from the jet energy scale are also included. The dominant theory uncertainties are the scale variations with smaller contributions from the combined PDF uncertainty. Figure 5.28 shows detector-level comparisons of data and MC simulation of $Z \to \ell^+\ell^-$ events and estimated backgrounds in the $\geq 1$ jet and VBF phase spaces. Statistical uncertainties from the finite size of the MC samples are included in the shaded bands. The data are typically larger than the MC prediction plus the estimated backgrounds, however, they are consistent within the systematic uncertainties.

A correction factor is applied to the denominator of the ratio to correct the data for detector and trigger inefficiencies and resolutions. The correction factor is defined as the ratio of $R^{\text{miss}}$ at detector-level to that at particle-level using $Z \to \nu\bar{\nu}$ and $Z/\gamma^* \to \ell^+\ell^-$ MC as a function of the measured variables. Another correction factor, $C_Z$, is defined as the ratio of the particle-level selection to the detector-level for the $\ell^+\ell^- +$ jets events only. The two correction factors are very similar, indicating that the dominant contribution to the correction factor is due to the lepton selection inefficiencies, as shown in Figure 5.29. Theoretical uncertainties and uncertainties due to jet energy scales or lepton-veto efficiencies almost completely cancel in the ratio. The reconstruction and identification efficiencies for muons are larger than that of electrons causing differences in the correction factors for the two channels. The correction factor for $Z \to \mu^+\mu^-$ decreases from 0.9 to 0.85 as a function of $p_T^{\text{miss}}$, whereas the correction factor for $Z \to e^+e^-$ increases from 0.7 to 0.8.

The effect of BSM models on the correction factors has been studied and was determined to be small. Any BSM models that are consistent with the data would only slightly change
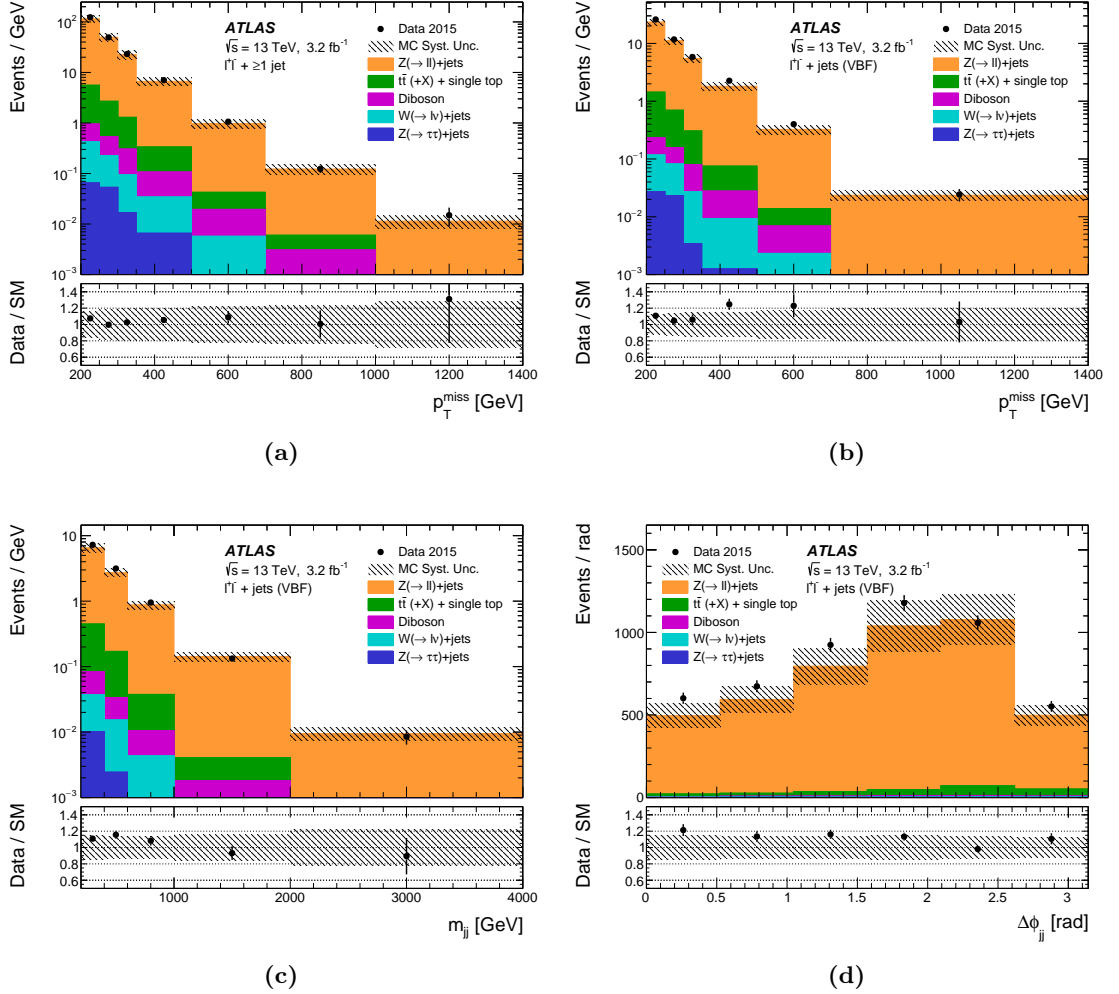
**Figure 5.28.** Comparisons between data and MC simulation of $Z \to \ell^+ \ell^-$ events plus predicted backgrounds as a function of (a) $p_T^{\mathrm{miss}}$ in the $\geq 1$ jet phase space, and (b) $p_T^{\mathrm{miss}}$, (c) $m_{\mathrm{jj}}$, (d) $\Delta\phi_{\mathrm{jj}}$ in the VBF phase space. [175]

the correction factors, therefore such models can be constrained by detector-corrected results. Other BSM models with very large contributions would significantly change the correction factors and would already be excluded by the limits set in detector-level analyses.

## 5.6. Ratio determination

The ratio $R^{\mathrm{miss}}$ is calculated using the events from the $p_T^{\mathrm{miss}} + \mathrm{jets}$ numerator, the $\mu^+ \mu^- + \mathrm{jets}$ and $e^+ e^- + \mathrm{jets}$ denominators, and the detector correction factors. Backgrounds are first subtracted from events in data for the numerator and each denominator. The denominators

**Figure 5.29.** Detector correction factor for (a) $Z \to e^+ e^-$ and (b) $Z \to \mu^+ \mu^-$ as a function of $p_\mathrm{T}^\mathrm{miss}$ in the $\geq 1$ jet phase space, showing the bin-by-bin correction factor obtained by taking the ratio of $R^\mathrm{miss}$ at pa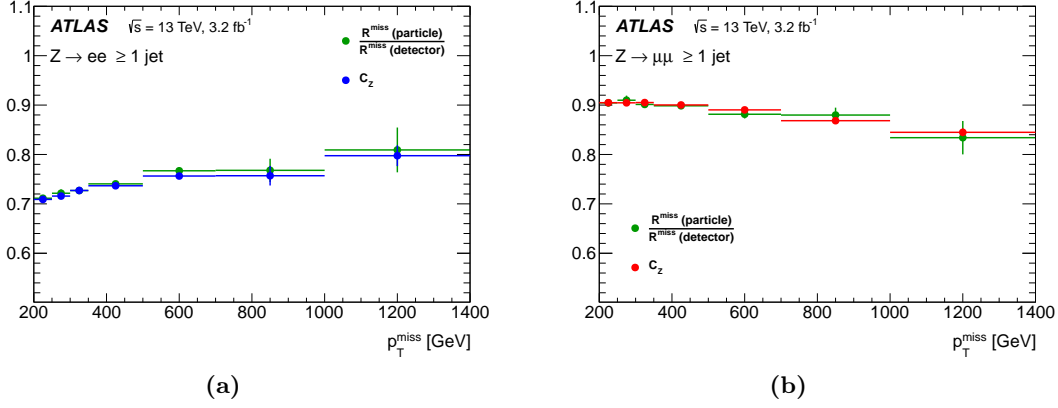rticle-level to that at detector-level. A correction factor, $C_\mathrm{Z}$, obtained from the ratio of the particle-level dilepton selection to the detector-level dilepton selection for the $\ell^+ \ell^- +$ jets events only, is also shown. [175]

are then corrected for detector effects by dividing each of them by their respective detector correction factors. The two detector-corrected denominators can be either added together or averaged into one flavour. The ratio is expected to be the same for all flavours due to lepton universality. The average of the denominators is chosen in order to reduce the MC samples needed to be generated in the future to test new models, however, the combination is significantly more complicated than the simple addition. The two denominators are combined using the Best Linear Unbiased Estimate (BLUE) combination method [212], which takes into account the correlations of statistical and systematic uncertainties between the two measurements in all bins and all four distributions. All sources of systematic uncertainties are assumed to be fully correlated between bins in the combination, with the exception of the muon and electron SF uncertainties, the correlation of which is found by considering the individual sources contributing to the total uncertainty. A bootstrap method, similar to the one used to calculate the statistical uncertainties for the acceptance corrections of the $W^\pm +$ jets backgrounds in Section 5.4.1, is used to account for statistical correlations between bins in the combination. The BLUE combination method has been cross-checked using a maximum likelihood fitting method, giving consistent results. The ratio is then constructed by dividing the background-subtracted $p_\mathrm{T}^\mathrm{miss} +$ jets numerator events with the averaged detector-corrected denominator, assuming fully correlated systematic uncertainties between them.

The size of the systematic and statistical uncertainties on the measured ratio for the lowest and highest $p_\mathrm{T}^\mathrm{miss}$ bins in the $\geq 1$ jet phase space and the lowest and highest $m_\mathrm{jj}$ bins in the VBF phase space are summarised in Table 5.3. The statistical uncertainty on the

data is taken as the Poisson error. Bins with large $p_\mathrm{T}^\mathrm{miss}$ or $m_\mathrm{jj}$ in the denominator have a small number of events leading to an asymmetric uncertainty on the ratio. The systematic uncertainties on the ratios are significantly smaller than the uncertainties on the numerator and denominator, mainly due to the cancellation of the theoretical uncertainties in the ratios.

| Systematic uncertainty source | Low $p_\mathrm{T}^\mathrm{miss}$ [%] | High $p_\mathrm{T}^\mathrm{miss}$ [%] | Low $m_\mathrm{jj}$ [%] | High $m_\mathrm{jj}$ [%] |
|---|---|---|---|---|
| Lepton efficiency | +3.5, −3.5 | +7.6, −7.1 | +3.7, −3.6 | +4.6, −4.4 |
| Jets | +0.8, −0.7 | +2.2, −2.8 | +1.1, −1.0 | +9.0, −0.5 |
| $W \to \tau\nu$ from control region | +1.2, −1.2 | +4.6, −4.6 | +1.3, −1.3 | +3.9, −3.9 |
| Multi-jet | +1.8, −1.8 | +0.9, −0.9 | +1.4, −1.4 | +2.5, −2.5 |
| Correction factor statistical | +0.2, −0.2 | +2.0, −1.9 | +0.4, −0.4 | +3.8, −3.6 |
| $W^\pm$ statistical | +0.5, −0.5 | +24, −24 | +1.1, −1.1 | +6.8, −6.8 |
| $W^\pm$ theory | +2.4, −2.3 | +6.0, −2.3 | +3.1, −3.0 | +4.9, −5.1 |
| Top cross-section | +1.5, −1.8 | +1.3, −0.1 | +1.1, −1.2 | +0.5, −0.4 |
| $Z \to \ell\ell$ backgrounds | +0.9, −0.8 | +1.1, −1.1 | +1.0, −1.0 | +0.1, −0.1 |
| **Total systematic uncertainty** | +5.2, −5.2 | +27, −26 | +5.6, −5.5 | +14, −11 |
| **Statistical uncertainty** | +1.7, −1.7 | +83, −44 | +3.5, −3.4 | +35, −25 |
| **Total uncertainty** | +5.5, −5.4 | +87, −51 | +6.6, −6.5 | +38, −27 |

**Table 5.3.** Summary of the uncertainties on the measured ratio for the lowest and highest $p_\mathrm{T}^\mathrm{miss}$ bins in the $\geq 1$ jet phase space and the lowest and highest $m_\mathrm{jj}$ bins in the VBF phase space. The statistical uncertainty is from the data. Statistical uncertainties on the MC are included as systematic uncertainties. The uncertainties vary monotonically as a function of the respective observable. [175]

Figure 5.30 shows the combined differential measurements of $R^\mathrm{miss}$ with the statistical and experimental uncertainties, compared to the SM particle-level predictions with theoretical uncertainties. The results are also compared to the number of events expected from the SM with the addition of a BSM model, for four BSM models. One is a simplified model of WIMP production with an $s$-channel exchange of an axial-vector mediator with mass of 1 TeV coupling to quarks and a WIMP mass of 10 GeV, another represents the Higgs boson decaying to invisible particles with 50% branching fraction, and the other two represent the predictions of two dimension-seven EFT operators allowing the production of DM through interactions with EWK bosons. Relatively good agreement is observed between the data and the SM prediction, consistent within the total statistical and systematic uncertainties, with a p-value for the agreement of all four distributions of 22%. The fiducial requirements on the charged leptons in the denominator cause less leptons to pass the selection and the ratio to be larger at low $p_\mathrm{T}^\mathrm{miss}$. Leptons have larger $p_\mathrm{T}$ and are more central at large $p_\mathrm{T}^\mathrm{miss}$ values and are more likely to pass the selection criteria. The $p_\mathrm{T}^\mathrm{miss}$

**(a)**

**(b)**

**(c)**

**(d)**
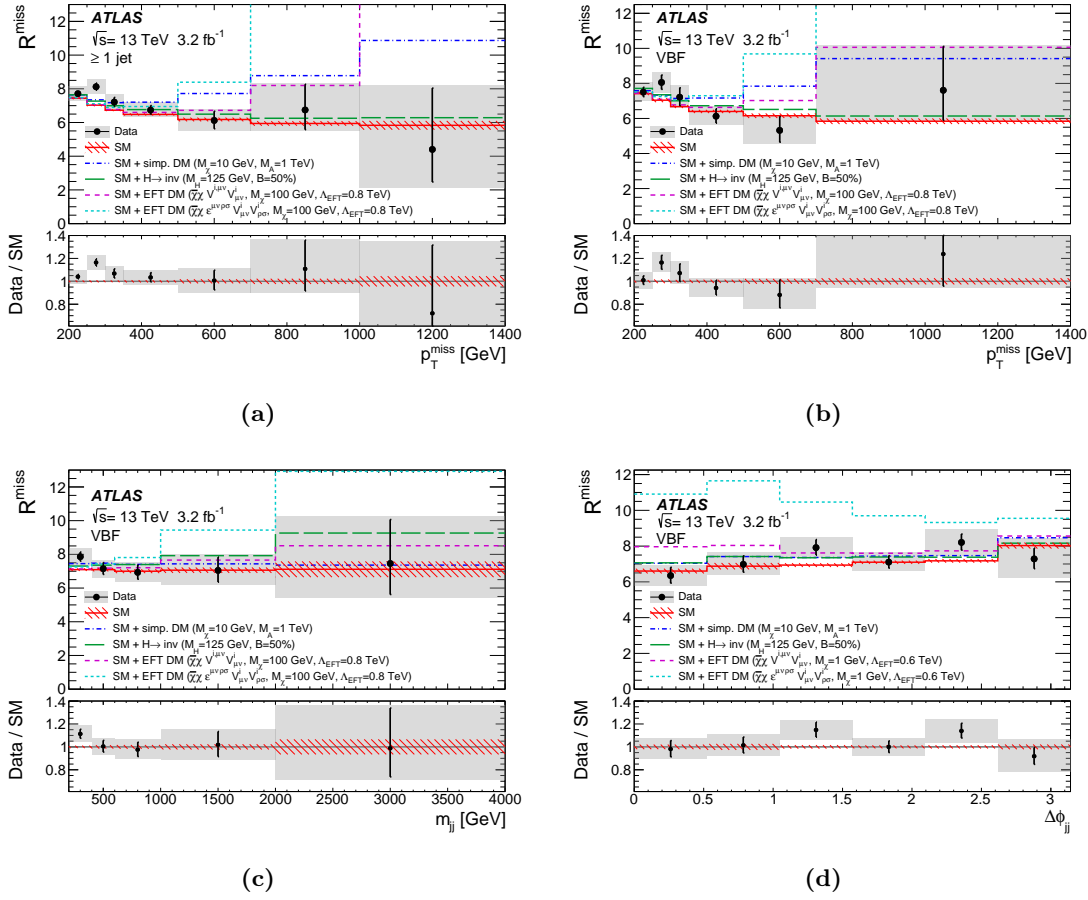
**Figure 5.30.** Measured $R^{\mathrm{miss}}$ as a function of function of (a) $p_{\mathrm{T}}^{\mathrm{miss}}$ in the $\geq 1$ jet phase space, and (b) $p_{\mathrm{T}}^{\mathrm{miss}}$, (c) $m_{\mathrm{jj}}$, (d) $\Delta\phi_{\mathrm{jj}}$ in the VBF phase space. Statistical uncertainties are shown as error bars and the total statistical and systematic uncertainties are shown as shaded bands. The results are compared to the SM particle-level prediction and to SM+BSM for four BSM models. The values of the third and fourth models in the highest $p_{\mathrm{T}}^{\mathrm{miss}}$ bin in the $\geq 1$ jet phase space are 18.8 and 38.3 respectively, and in the highest $p_{\mathrm{T}}^{\mathrm{miss}}$ bin in the VBF phase space the fourth model has a value of 19.4. [175]

distributions provide discriminating power for the simplified and EFT models, whereas the $m_{\mathrm{jj}}$ distribution provides more discriminating power for the invisible Higgs model which is fairly flat in all other distributions. The ratio increases at large $\Delta\phi_{\mathrm{jj}}$ due to more jets being removed in the denominator by the overlap-removal requirements. A covariance matrix for the four distributions is also constructed, taking into account the statistical and systematic correlations between all bins, and a statistical only correlation matrix, as shown in Figure 5.31.
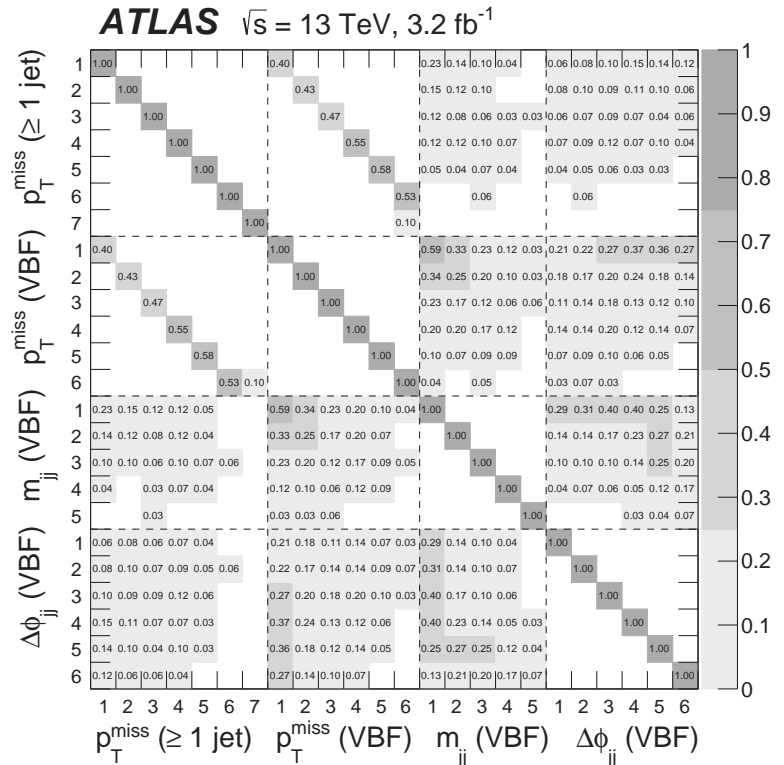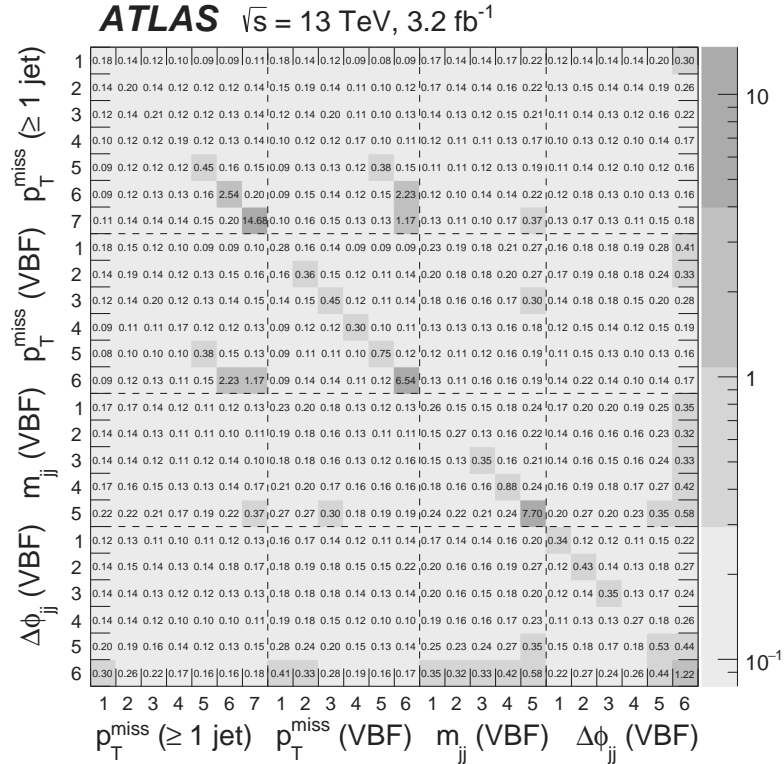
(a)



(b)

**Figure 5.31.** (a) Covariance matrix and (b) statistical only correlation matrix for all four measured distributions. The number on the axes indicates the bin number for each distribution. [175]

## 5.7. Constraining new physics

Limits are set on the production of a Dirac fermion DM in a generalised EFT where DM interacts only with electroweak bosons, on an axial-vector mediator WIMP simplified model, and the production of an invisibly decaying Higgs boson. No significant deviations are observed with no signs of new physics. The detector-corrected $R^{\text{miss}}$ ratio, the covariance matrix for the statistical and systematic uncertainties, and the theoretical uncertainties on the SM predictions of the numerator, denominator, and BSM models are used for setting limits. The limits on the DM production models are set by calculating the $\chi^2$, given by

$$\chi^2 = (\mathbf{y}_{\text{data}} - \mathbf{y}_{\text{pred}})^T C^{-1} (\mathbf{y}_{\text{data}} - \mathbf{y}_{\text{pred}}) \qquad (5.10)$$

where $\mathbf{y}_{\text{data}}$ is the vector of the measured $R^{\text{miss}}$ values, $\mathbf{y}_{\text{pred}}$ is the vector of the predicted $R^{\text{miss}}$ values for the hypothesis under test for the four distributions under study, and $C = C_{\text{stat}} + C_{\text{exp}} + C_{\text{model}}$ is the total covariance matrix defined as the sum of the statistical, experimental systematic and theoretical systematic covariances. Upper limits are derived using the CL$_{\text{S}}$ technique [213, 214] evaluated using the asymptotic approximation [215].

Limits on the production of a Dirac fermion DM in a generalised EFT where DM interacts only with electroweak bosons, described in Section 2.2.2, are set on the DM candidate mass, $m_\chi$, and the EFT scale, $\Lambda$. Only two dimension-seven operators are considered, $\bar{\chi}\chi V^{\mu\nu}V_{\mu\nu}$ and $\bar{\chi}\chi\varepsilon^{\mu\nu\rho\sigma}V_{\mu\nu}V_{\rho\sigma}$, with the former conserving CP and the latter violating it. Figure 5.32 shows the 95% CL exclusion limits for each operator compared to indirect detection limits [33, 216, 217]. The expected limits on the CP-conserving operator range from 0.78 at low DM masses ($< 200$ GeV) to 0.61 TeV at higher DM masses of 1 TeV and the observed limits range from 0.89 to 0.71 TeV. The limits on the CP-violating operator are stronger, with the expected limits ranging from 0.99 at low DM masses to 0.77 TeV at higher DM masses of 1 TeV and the observed limits ranging from 1.14 to 0.89 TeV. The limits from indirect detection searches interpreted in terms of these operators are sensitive up to EFT scales of 100–200 GeV. The limits assume that a single operator dominates the DM production rate, however it is possible to use the detector-corrected ratios and the covariance matrix to set limits on more complex models with multiple operators.

Limits on the axial-vector mediator WIMP simplified model, described in Section 2.2.2, are set on the mediator mass, $m_A$, and the WIMP candidate mass, $m_\chi$. The expected and observed 95% confidence level (CL) exclusion limits for this model, including the effect of $\pm 1\sigma$ experimental and theoretical uncertainties are shown in Figure 5.33. The expected relic density measured by Planck [218] and WMAP [219], and the region of non-perturbativity, defined by $m_\chi > \sqrt{\pi/2}m_A$, are also shown. WIMP masses below the
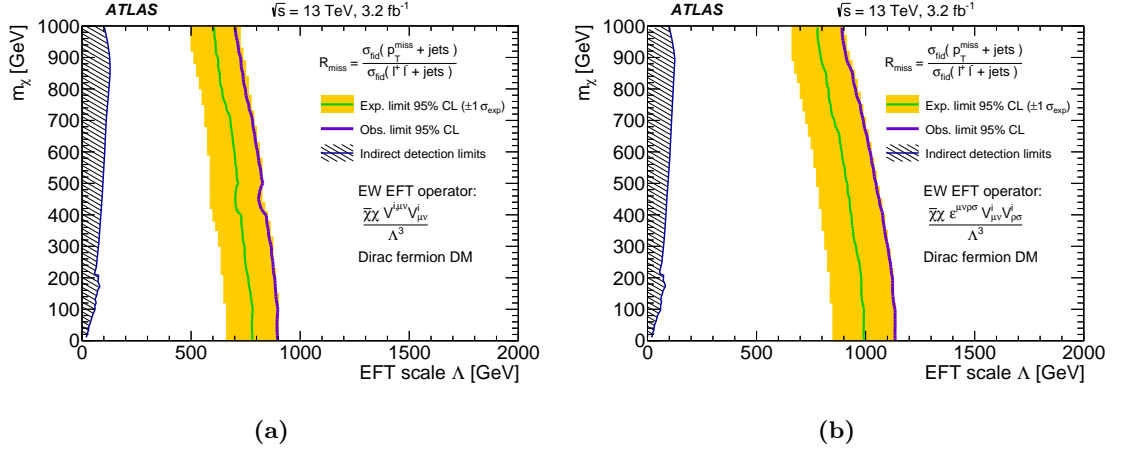
**Figure 5.32.** 95% CL exclusion contours for Dirac fermion DM produced via a contact interaction with two electroweak bosons as described in an EFT with two dimension-seven operators with different CP properties. The median of the observed and expected limits are shown, including the effect of $\pm 1\sigma$ experimental uncertainties on the expected limit. Limits on these operators from indirect detection experiments are also shown. The exclusion is based on the global fit to the $p_T^{miss}$ distribution in the $\geq 1$ jet phase space, and the $p_T^{miss}$, $m_{jj}$ and $\Delta\phi_{jj}$ distributions in the VBF phase space. [175]

relic density or mediator masses to the right of it correspond to DM overproduction. The shape of the exclusion limits for this simplified model is different from the EFT model due to the presence of a massive mediator. At low mediator mass and high WIMP mass, the WIMP particles are produced off-shell with reduced production cross-sections. The largest mediator masses excluded are 1.09 TeV for expected limits and 1.24 TeV for observed. Limits set using detector-level event counts from the ATLAS mono-jet search [95] are also included for comparison. The limited statistics in the denominator cause the expected limits for high mediator masses to be slightly weaker than the detector-level limits. On the other hand, the correlations of systematic uncertainties between the bins of the detector-corrected distributions cause the observed limits to be slightly stronger than the detector-level limits. The use of differential observables with associated correlations and a broader fiducial region enhance the sensitivity to large WIMP masses and low mediator masses compared to the detector-level analysis. These limits are complementary to the detector-level limits and can provide a stronger and more interpretable measurement that detector-level analyses which are better for checking for discovery. Limits are also set on the production rate of an invisibly decaying Higgs boson, the branching fraction of which is vanishingly small in the SM. The limits are set on the production rate of the Higgs boson multiplied by its branching fraction to invisibles relative to the total Higgs boson production rate predicted by the SM [220]. The limits in this model are driven by the $m_{jj}$ distribution with some additional expected sensitivity from the $\Delta\phi_{jj}$ distribution. The expected 95% CL exclusion
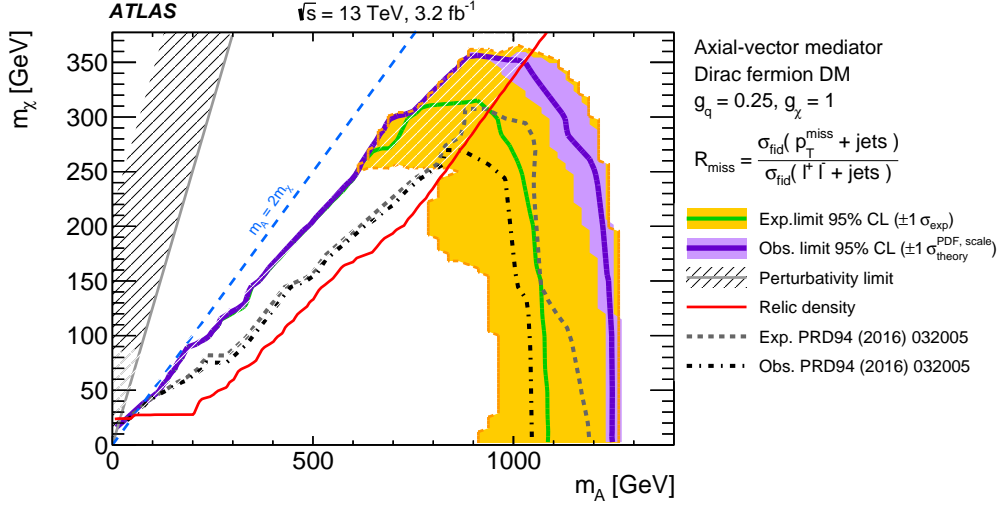
**Figure 5.33.** 95% CL exclusion contours in the WIMP–mediator mass plane for a simplified model with an axial-vector mediator and couplings $g_q = 0.25$ and $g_\chi = 1$. The median of the observed and expected limits are shown, including the effect of $\pm 1\sigma$ experimental uncertainties on the expected limit. The exclusion is based on the global fit to the $p_T^{miss}$ distribution in the $\geq 1$ jet phase space, and the $p_T^{miss}$, $m_{jj}$ and $\Delta\phi_{jj}$ distributions in the VBF phase space. [175]

limit for a Higgs boson with a mass of 125 GeV is 0.59 with a range of [0.47, 1.13] from the $\pm 1\sigma$ experimental uncertainties and the observed limit is 0.46 [175]. The correlations of the systematic uncertainties between the bins of the detector-corrected $R^{miss}$ distributions cause the observed limits to be stronger than the expected. For comparison, the observed and expected 95% CL exclusion limits using $\sqrt{s} = 8$ TeV and 20 fb$^{-1}$ with an event selection optimised for this process are 0.28 and 0.31 respectively [221].

BSM models at particle-level that produce $p_T^{miss}$ + jets or $\ell^+\ell^-$ + jets final states or combinations of those models with the SM can also be compared to the detector-corrected data. New models with final states containing one prompt lepton and $p_T^{miss}$ or two prompt leptons cannot be accurately compared to the data. Events with one prompt lepton and $p_T^{miss}$ are included in the $W^\pm$ + jets background estimation and the acceptance correction factors determined using SM MC would be incorrect in this case. Similarly, events with two prompt leptons are included in the denominator, therefore new models with this final state can only be reliably constrained by the data if the lepton kinematics are similar to the SM. The detector-corrected observed and expected ratios, the numerator and the denominator predicted by the SM, and the covariance matrix for the uncertainties are made available within the HepData [222] project and can be found in Ref. [175]. The analysis is included as a routine in the Rivet [223] analysis framework.

# Chapter 6.

# Conclusions

The ATLAS trigger system has been upgraded for the 2015 data taking and a new jet reconstruction algorithm has been developed for the updated jet trigger software. Diagnostic algorithms have been developed to test the new software and its validation has been automated using a new jet trigger validation package, which can be used to validate future developments. The new jet triggers work as expected and their performance has been evaluated using the full 2015 dataset. The HLT triggers have steeper turn-on curves than the L1 triggers due to the similarities between HLT and offline jets. Good agreement is observed between data and simulation for HLT triggers. Multi-jet triggers with different number of jets but same threshold have very similar efficiencies. Future trigger developments, such as applying jet calibration using tracking information similar to offline jets, can improve the performance.

In addition, a new analysis searching for DM in events with jets and missing transverse momentum using ratio measurements has been discussed. The numerator of the ratio is the fiducial cross-section of $p_T^{\text{miss}}$ + jets events (inclusive $Z \to \nu\bar{\nu}$ + jets) and the denominator is the fiducial cross-section of $\ell^+\ell^-$ + jets events ($\mu^+\mu^-$ + jets and $e^+e^-$ + jets). The dominant background to the numerator is due to $W^{\pm}$ + jets events and two different data-driven background estimation methods are presented giving consistent results. Cross-checks have also been performed to ensure the data-driven background estimates are accurate. The dominant background to the denominator is due to top-quark events and the denominator backgrounds are also estimated using data-driven methods. The two denominators are corrected for detector effects and averaged into one single-flavour denominator. The ratio is measured differentially with respect to four variables in two phase-spaces, one inclusive with at least one high-$p_T$ jet and one sensitive to VBF processes. The detector-corrected measured ratios are consistent with the SM particle-level predictions within their respective uncertainties and are used to place limits on DM models. Limits are placed on three BSM models, an axial-vector mediator WIMP simplified model, the production of an invisibly decaying Higgs boson, and on the production of Dirac fermion DM in a generalised

EFT where DM interacts only with EWK bosons. The limits on the simplified model are competitive with detector-level limits and provide improved sensitivity for models in which the DM mass is close to half of the mediator mass. The limits on the EFT models currently represent the most stringent constraints on such interactions.

The limited statistics on the denominator limit the sensitivity of the measurements. The statistics can be improved by using more data collected in 2016 + 2017 and also by changing the denominator. The leptonic decay of a $W^{\pm}$ boson and the $\gamma + \text{jets}$ process can also be used as the denominator providing increased statistics. The use of detector-corrected data to constraint the often huge parameter spaces of new-physics models is complementary to detector-level searches, but with tools such as Contur [224], which are being developed to utilise exactly this sort of data and allow for limits to be set on new-physics models directly, the need for computationally expensive or otherwise inaccessible detector simulation is removed. This maximises the longevity of the data and ensures that the full potential of the LHC can be exploited.

# Appendix A.

# Electron and tau lepton efficiencies

This Appendix contains the electron and tau lepton efficiencies, calculated using the Sherpa v2.2.0 $W^\pm + $ jets and Sherpa v2.1.1 EWK $W^\pm + $ jets samples after derivation cuts. No analysis cuts have been applied, only the electron and tau lepton object selection cuts, to increase the statistics in each bin. The muon efficiencies are provided by the relevant ATLAS Combined Performance working group.

The reconstuction efficiencies are calculated as a function of the particle-level lepton $p_{\mathrm{T}}$ and $\eta$ and are defined as the number of events with a prompt lepton matched to a calibrated detector-level lepton (any lepton in the container without requring any cuts), divided by the number of events with a prompt lepton.

The identification efficiencies are calculated as a function of the detector-level lepton $p_{\mathrm{T}}$ and $\eta$ and are defined as the number of events with a calibrated detector-level lepton passing all lepton object selections matched to a prompt particle-level lepton, divided by the number of events with a calibrated detector-level lepton matched to a prompt particle-level lepton.

Particle-level and detector-level leptons are matched using a $\Delta R$ cut of $< 0.1$ for electrons and $< 0.2$ for tau leptons. Only the visible $p_{\mathrm{T}}$ and $\eta$ of the prompt particle-level tau leptons is used to match them to detector-level tau leptons.

The electron reconstruction and identification (including isolation) efficiencies for the *Loose* and *Tight* likelihood working points as a function of $p_{\mathrm{T}}$ and $\eta$ are shown in Figure A.1. The calorimeter crack region is excluded from the identification efficiencies. The electron trigger efficiencies are provided by the relevant ATLAS Combined Performance working group and are not included in these plots.
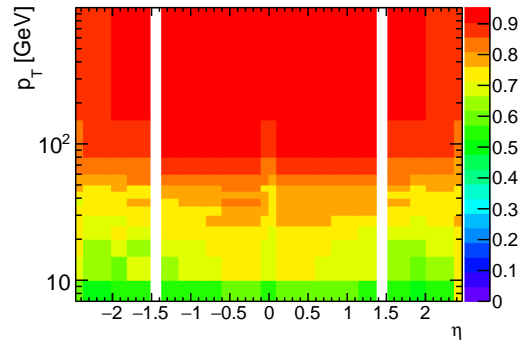
The tau lepton reconstuction and identification efficiencies for the *Loose* working point as a function of $p_{\mathrm{T}}$ and $\eta$ are shown in Figure A.2. The calorimeter crack region is excluded from the identification efficiencies.
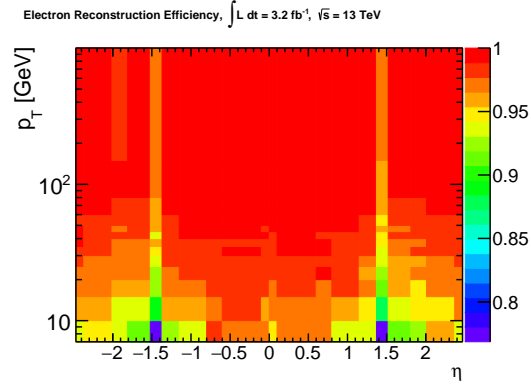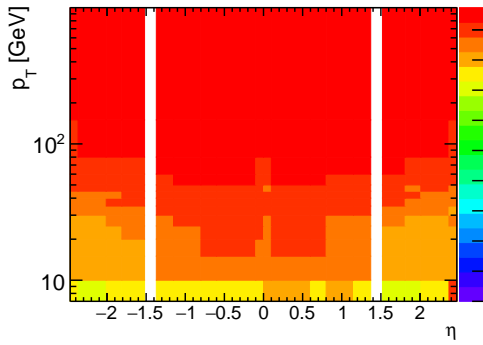
**Figure A.1.** Electron (a) reconstruction efficiency as a function of particle-level electron $p_T$ and $\eta$, (b) *Loose* and (c) *Tight* likelihood working point efficiencies as a function of detector-level electron $p_T$ and $\eta$.
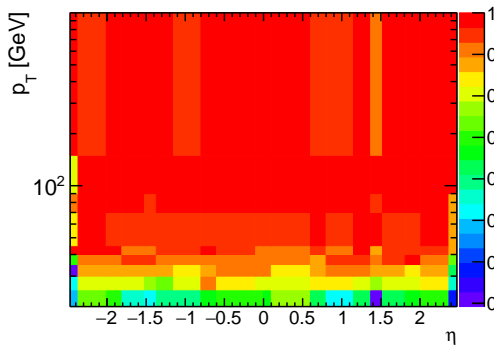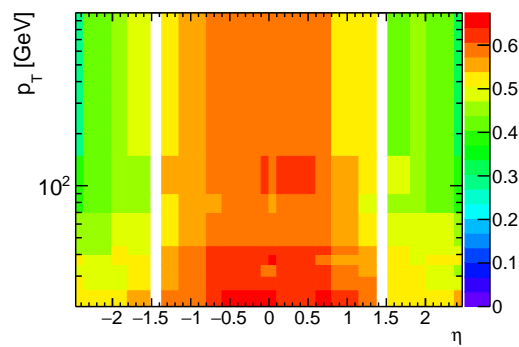


**Figure A.2.** Tau lepton (a) reconstruction efficiency as a function of particle-level visible $p_T$ and $\eta$, (b) *Loose* working point efficiency as a function of detector-level $p_T$ and $\eta$.

# Bibliography

[1] F. Zwicky, *Die Rotverschiebung von extragalaktischen Nebeln*, Helvetica Physica Acta **6** (1933) 110–127.

[2] J. H. Oort, *Some Problems Concerning the Structure and Dynamics of the Galactic System and the Elliptical Nebulae NGC 3115 and 4494*, Astrophys. J. **91** (Apr., 1940) 273.

[3] Planck Collaboration, *Planck 2013 results. I. Overview of products and scientific results*, Astron. Astrophys. **571** (2014) A1, `arXiv:1303.5062 [astro-ph.CO]`.

[4] G. Bertone, D. Hooper, and J. Silk, *Particle dark matter: Evidence, candidates and constraints*, Phys. Rept. **405** (2005) 279–390, `arXiv:hep-ph/0404175 [hep-ph]`.

[5] LUX Collaboration, *The Large Underground Xenon (LUX) Experiment*, Nucl. Instrum. Meth. **A704** (2013) 111–126, `arXiv:1211.3788 [physics.ins-det]`.

[6] AMS Collaboration, *The antimatter spectrometer (AMS-02): A particle physics detector in space*, Nucl. Instrum. Meth. **A588** (2008) 227–234.

[7] L. Evans and P. Bryant, *LHC Machine*, JINST **3** (2008) S08001.

[8] ATLAS Collaboration, *The ATLAS Experiment at the CERN Large Hadron Collider*, JINST **3** (2008) S08003.

[9] Particle Data Group Collaboration, *Review of Particle Physics*, Chin. Phys. **C40** (2016) no. 10, 100001.

[10] A. Purcell, *Go on a particle quest at the first CERN webfest. Le premier webfest du CERN se lance à la conquête des particules*, 2012. `https://cds.cern.ch/record/1473657`.

[11] ATLAS Collaboration, *Observation of a new particle in the search for the Standard Model Higgs boson with the ATLAS detector at the LHC*, Phys. Lett. **B716** (2012) 1–29, `arXiv:1207.7214 [hep-ex]`.

[12] CMS Collaboration, *Observation of a new boson at a mass of 125 GeV with the CMS*

*experiment at the LHC*, Phys. Lett. **B716** (2012) 30–61, `arXiv:1207.7235` `[hep-ex]`.

[13] A. S. Kronfeld and C. Quigg, *Resource Letter: Quantum Chromodynamics*, Am. J. Phys. **78** (2010) 1081–1116, `arXiv:1002.5032 [hep-ph]`.

[14] S. L. Glashow, *Partial Symmetries of Weak Interactions*, Nucl. Phys. **22** (1961) 579–588.

[15] A. Salam, *Weak and Electromagnetic Interactions*, Conf. Proc. **C680519** (1968) 367–377.

[16] S. Weinberg, *A Model of Leptons*, Phys. Rev. Lett. **19** (1967) 1264–1266.

[17] N. Cabibbo, *Unitary Symmetry and Leptonic Decays*, Phys. Rev. Lett. **10** (1963) 531–533.

[18] M. Kobayashi and T. Maskawa, *CP Violation in the Renormalizable Theory of Weak Interaction*, Prog. Theor. Phys. **49** (1973) 652–657.

[19] F. Englert and R. Brout, *Broken Symmetry and the Mass of Gauge Vector Mesons*, Phys. Rev. Lett. **13** (1964) 321–323.

[20] P. W. Higgs, *Broken symmetries, massless particles and gauge fields*, Phys. Lett. **12** (1964) 132–133.

[21] P. W. Higgs, *Broken Symmetries and the Masses of Gauge Bosons*, Phys. Rev. Lett. **13** (1964) 508–509.

[22] G. S. Guralnik, C. R. Hagen, and T. W. B. Kibble, *Global Conservation Laws and Massless Particles*, Phys. Rev. Lett. **13** (1964) 585–587.

[23] P. W. Higgs, *Spontaneous Symmetry Breakdown without Massless Bosons*, Phys. Rev. **145** (1966) 1156–1163.

[24] T. W. B. Kibble, *Symmetry breaking in non-Abelian gauge theories*, Phys. Rev. **155** (1967) 1554–1561.

[25] J. R. Ellis, *Limits of the standard model*, in *PSI Zuoz Summer School on Exploring the Limits of the Standard Model Zuoz, Engadin, Switzerland, August 18-24, 2002*. 2002. `arXiv:hep-ph/0211168 [hep-ph]`.

[26] Super-Kamiokande Collaboration, *Evidence for oscillation of atmospheric neutrinos*, Phys. Rev. Lett. **81** (1998) 1562–1567, `arXiv:hep-ex/9807003 [hep-ex]`.

[27] SNO Collaboration, *Measurement of the rate of $\nu_e + d \rightarrow p + p + e^-$ interactions*

*produced by* $^8B$ *solar neutrinos at the Sudbury Neutrino Observatory*, Phys. Rev. Lett. **87** (2001) 071301, `arXiv:nucl-ex/0106015 [nucl-ex]`.

[28] SNO Collaboration, *Direct evidence for neutrino flavor transformation from neutral current interactions in the Sudbury Neutrino Observatory*, Phys. Rev. Lett. **89** (2002) 011301, `arXiv:nucl-ex/0204008 [nucl-ex]`.

[29] T. D. Lee and C.-N. Yang, *Question of Parity Conservation in Weak Interactions*, Phys. Rev. **104** (1956) 254–258.

[30] C. S. Wu, E. Ambler, R. W. Hayward, D. D. Hoppes, and R. P. Hudson, *Experimental Test of Parity Conservation in Beta Decay*, Phys. Rev. **105** (1957) 1413–1414.

[31] H. Hoekstra, H. Yee, and M. Gladders, *Current status of weak gravitational lensing*, New Astron. Rev. **46** (2002) 767–781, `arXiv:astro-ph/0205205 [astro-ph]`.

[32] M. Endo and Y. Yamamoto, *Unitarity Bounds on Dark Matter Effective Interactions at LHC*, JHEP **06** (2014) 126, `arXiv:1403.6610 [hep-ph]`.

[33] R. C. Cotta, J. L. Hewett, M. P. Le, and T. G. Rizzo, *Bounds on Dark Matter Interactions with Electroweak Gauge Bosons*, Phys. Rev. **D88** (2013) 116009, `arXiv:1210.0525 [hep-ph]`.

[34] J. Brooke, M. R. Buckley, P. Dunne, B. Penning, J. Tamanas, and M. Zgubic, *Vector Boson Fusion Searches for Dark Matter at the LHC*, Phys. Rev. **D93** (2016) no. 11, 113013, `arXiv:1603.07739 [hep-ph]`.

[35] C. E. Yaguna, *Gamma ray lines: What will they tell us about SUSY?*, Phys. Rev. **D80** (2009) 115002, `arXiv:0909.4181 [hep-ph]`.

[36] J. Abdallah et al., *Simplified Models for Dark Matter Searches at the LHC*, Phys. Dark Univ. **9-10** (2015) 8–23, `arXiv:1506.03116 [hep-ph]`.

[37] D. Abercrombie et al., *Dark Matter Benchmark Models for Early LHC Run-2 Searches: Report of the ATLAS/CMS Dark Matter Forum*, `arXiv:1507.00966 [hep-ex]`.

[38] A. Albert et al., *Recommendations of the LHC Dark Matter Working Group: Comparing LHC searches for heavy mediators of dark matter production in visible and invisible decay channels*, `arXiv:1703.05703 [hep-ex]`.

[39] C. Englert, T. Plehn, D. Zerwas, and P. M. Zerwas, *Exploring the Higgs portal*, Phys. Lett. **B703** (2011) 298–305, `arXiv:1106.3097 [hep-ph]`.

[40] K. Assamagan et al., *The Higgs Portal and Cosmology*, 2016. `arXiv:1604.05324 [hep-ph]`.

[41] C. P. Burgess, M. Pospelov, and T. ter Veldhuis, *The Minimal model of nonbaryonic dark matter: A Singlet scalar*, Nucl. Phys. **B619** (2001) 709–728, `arXiv:hep-ph/0011335 [hep-ph]`.

[42] V. Barger, P. Langacker, M. McCaskey, M. J. Ramsey-Musolf, and G. Shaughnessy, *LHC Phenomenology of an Extended Standard Model with a Real Scalar Singlet*, Phys. Rev. **D77** (2008) 035005, `arXiv:0706.4311 [hep-ph]`.

[43] A. Djouadi, O. Lebedev, Y. Mambrini, and J. Quevillon, *Implications of LHC searches for Higgs–portal dark matter*, Phys. Lett. **B709** (2012) 65–69, `arXiv:1112.3299 [hep-ph]`.

[44] A. Djouadi, A. Falkowski, Y. Mambrini, and J. Quevillon, *Direct Detection of Higgs-Portal Dark Matter at the LHC*, Eur. Phys. J. **C73** (2013) no. 6, 2455, `arXiv:1205.3169 [hep-ph]`.

[45] J. M. Cline, K. Kainulainen, P. Scott, and C. Weniger, *Update on scalar singlet dark matter*, Phys. Rev. **D88** (2013) 055025, `arXiv:1306.4710 [hep-ph]`. [Erratum: Phys. Rev.D92,no.3,039906(2015)].

[46] V. V. Khoze, C. McCabe, and G. Ro, *Higgs vacuum stability from the dark matter portal*, JHEP **08** (2014) 026, `arXiv:1403.4953 [hep-ph]`.

[47] N. Craig, H. K. Lou, M. McCullough, and A. Thalapillil, *The Higgs Portal Above Threshold*, JHEP **02** (2016) 127, `arXiv:1412.0258 [hep-ph]`.

[48] Y. G. Kim, K. Y. Lee, and S. Shin, *Singlet fermionic dark matter*, JHEP **05** (2008) 100, `arXiv:0803.2932 [hep-ph]`.

[49] S. Baek, P. Ko, and W.-I. Park, *Search for the Higgs portal to a singlet fermionic dark matter at the LHC*, JHEP **02** (2012) 047, `arXiv:1112.1847 [hep-ph]`.

[50] L. Lopez-Honorez, T. Schwetz, and J. Zupan, *Higgs portal, fermionic dark matter, and a Standard Model like Higgs at 125 GeV*, Phys. Lett. **B716** (2012) 179–185, `arXiv:1203.2064 [hep-ph]`.

[51] D. Yu. Akimov et al., *WIMP-nucleon cross-section results from the second science run of ZEPLIN-III*, Phys. Lett. **B709** (2012) 14–20, `arXiv:1110.4769 [astro-ph.CO]`.

[52] XENON100 Collaboration, *XENON100 Dark Matter Results from a Combination of*

*477 Live Days*, Phys. Rev. **D94** (2016) no. 12, 122001, `arXiv:1609.06154`
`[astro-ph.CO]`.

[53] PandaX Collaboration, *First dark matter search results from the PandaX-I experiment*, Sci. China Phys. Mech. Astron. **57** (2014) 2024–2030, `arXiv:1408.5114`
`[hep-ex]`.

[54] LUX Collaboration, *Results from a search for dark matter in the complete LUX exposure*, Phys. Rev. Lett. **118** (2017) no. 2, 021303, `arXiv:1608.07648`
`[astro-ph.CO]`.

[55] DARKSIDE Collaboration, *Recent resuts from DARKSIDE*, Nuovo Cim. **C38** (2016) no. 4, 118.

[56] PICO Collaboration, *Dark matter search results from the PICO-60 CF$_3$I bubble chamber*, Phys. Rev. **D93** (2016) no. 5, 052014, `arXiv:1510.07754 [hep-ex]`.

[57] CRESST-II Collaboration, *Results on low mass WIMPs using an upgraded CRESST-II detector*, Eur. Phys. J. **C74** (2014) no. 12, 3184, `arXiv:1407.3146`
`[astro-ph.CO]`.

[58] EDELWEISS Collaboration, *Constraints on low-mass WIMPs from the EDELWEISS-III dark matter search*, JCAP **1605** (2016) no. 05, 019,
`arXiv:1603.05120 [astro-ph.CO]`.

[59] SuperCDMS Collaboration, *Search for Low-Mass Weakly Interacting Massive Particles with SuperCDMS*, Phys. Rev. Lett. **112** (2014) no. 24, 241302,
`arXiv:1402.7137 [hep-ex]`.

[60] CoGeNT Collaboration, *CoGeNT: A Search for Low-Mass Dark Matter using p-type Point Contact Germanium Detectors*, Phys. Rev. **D88** (2013) 012002,
`arXiv:1208.5737 [astro-ph.CO]`.

[61] DAMIC Collaboration, *First Direct Detection Constraints on eV-Scale Hidden Photon Dark Matter with DAMIC at SNOLAB*, Submitted to: Phys. Rev. Lett. (2016) , `arXiv:1611.03066 [astro-ph.CO]`.

[62] LUX Collaboration, *Limits on spin-dependent WIMP-nucleon cross section obtained from the complete LUX exposure*, Phys. Rev. Lett. **118** (2017) no. 25, 251302,
`arXiv:1705.03380 [astro-ph.CO]`.

[63] L. Roszkowski, E. M. Sessolo, and S. Trojanowski, *WIMP dark matter candidates and searches - current issues and future prospects*, `arXiv:1707.06277 [hep-ph]`.

[64] IceCube Collaboration, *Search for annihilating dark matter in the Sun with 3 years of IceCube data*, Eur. Phys. J. **C77** (2017) no. 3, 146, `arXiv:1612.05949` `[astro-ph.HE]`.

[65] ANTARES Collaboration, *Limits on Dark Matter Annihilation in the Sun using the ANTARES Neutrino Telescope*, Phys. Lett. **B759** (2016) 69–74, `arXiv:1603.02228` `[astro-ph.HE]`.

[66] AMS Collaboration, *AMS-02 in Space: Physics Results*, J. Phys. Conf. Ser. **650** (2015) no. 1, 012001, `arXiv:1511.05890` `[astro-ph.HE]`.

[67] DES, Fermi-LAT Collaboration, *Searching for Dark Matter Annihilation in Recently Discovered Milky Way Satellites with Fermi-LAT*, Astrophys. J. **834** (2017) no. 2, 110, `arXiv:1611.03184` `[astro-ph.HE]`.

[68] Super-Kamiokande Collaboration, *Search for neutrinos from annihilation of captured low-mass dark matter particles in the Sun by Super-Kamiokande*, Phys. Rev. Lett. **114** (2015) no. 14, 141301, `arXiv:1503.04858` `[hep-ex]`.

[69] P. Scott, *Neutrino telescope searches for dark matter in the Sun*, in *Rencontres du Vietnam: Neutrinos 2017 Quy Nhon, Vietnam, July 16-22, 2017.* 2017. `arXiv:1710.05190` `[hep-ph]`.

[70] H.-L. Lai, M. Guzzi, J. Huston, Z. Li, P. M. Nadolsky, J. Pumplin, and C. P. Yuan, *New parton distributions for collider physics*, Phys. Rev. **D82** (2010) 074024, `arXiv:1007.2241` `[hep-ph]`.

[71] A. D. Martin, W. J. Stirling, R. S. Thorne, and G. Watt, *Parton distributions for the LHC*, Eur. Phys. J. **C63** (2009) 189–285, `arXiv:0901.0002` `[hep-ph]`.

[72] R. D. Ball et al., *Parton distributions with LHC data*, Nucl. Phys. **B867** (2013) 244–289, `arXiv:1207.1303` `[hep-ph]`.

[73] J. C. Collins, D. E. Soper, and G. F. Sterman, *Factorization of Hard Processes in QCD*, Adv. Ser. Direct. High Energy Phys. **5** (1989) 1–91, `arXiv:hep-ph/0409313` `[hep-ph]`.

[74] S. J. Brodsky and L. Di Giustino, *Setting the Renormalization Scale in QCD: The Principle of Maximum Conformality*, Phys. Rev. **D86** (2012) 085026, `arXiv:1107.0338` `[hep-ph]`.

[75] G. P. Salam and G. Soyez, *A Practical Seedless Infrared-Safe Cone jet algorithm*, JHEP **05** (2007) 086, `arXiv:0704.0292` `[hep-ph]`.

[76] S. D. Ellis and D. E. Soper, *Successive combination jet algorithm for hadron collisions*, Phys. Rev. **D48** (1993) 3160–3166, `arXiv:hep-ph/9305266 [hep-ph]`.

[77] M. Wobisch and T. Wengler, *Hadronization corrections to jet cross-sections in deep inelastic scattering*, in *Monte Carlo generators for HERA physics. Proceedings, Workshop, Hamburg, Germany, 1998-1999*, pp. 270–279. 1998. `arXiv:hep-ph/9907280 [hep-ph]`.

[78] M. Cacciari, G. P. Salam, and G. Soyez, *The anti-$k_t$ jet clustering algorithm*, JHEP **04** (2008) 063, `arXiv:0802.1189 [hep-ph]`.

[79] A. Buckley et al., *General-purpose event generators for LHC physics*, Phys. Rept. **504** (2011) 145–233, `arXiv:1101.2599 [hep-ph]`.

[80] S. Catani, F. Krauss, R. Kuhn, and B. R. Webber, *QCD matrix elements + parton showers*, JHEP **11** (2001) 063, `arXiv:hep-ph/0109231 [hep-ph]`.

[81] S. Höeche, F. Krauss, S. Schumann, and F. Siegert, *QCD matrix elements and truncated showers*, JHEP **05** (2009) 053, `arXiv:0903.1219 [hep-ph]`.

[82] L. Lonnblad, *Correcting the color dipole cascade model with fixed order matrix elements*, JHEP **05** (2002) 046, `arXiv:hep-ph/0112284 [hep-ph]`.

[83] B. Andersson, G. Gustafson, G. Ingelman, and T. Sjostrand, *Parton Fragmentation and String Dynamics*, Phys. Rept. **97** (1983) 31–145.

[84] B. R. Webber, *A QCD Model for Jet Fragmentation Including Soft Gluon Interference*, Nucl. Phys. **B238** (1984) 492–528.

[85] J. Alwall et al., *The automated computation of tree-level and next-to-leading order differential cross sections, and their matching to parton shower simulations*, JHEP **2014** (2014) 158, `arXiv:1405.0301 [hep-ph]`.

[86] T. Gleisberg, S. Höche, F. Krauss, M. Schönherr, S. Schumann, et al., *Event generation with SHERPA 1.1*, JHEP **0902** (2009) 007, `arXiv:0811.4622 [hep-ph]`.

[87] P. Nason, *A New method for combining NLO QCD with shower Monte Carlo algorithms*, JHEP **11** (2004) 040, `arXiv:hep-ph/0409146 [hep-ph]`.

[88] S. Frixione, P. Nason, and C. Oleari, *Matching NLO QCD computations with Parton Shower simulations: the POWHEG method*, JHEP **11** (2007) 070, `arXiv:0709.2092 [hep-ph]`.

[89] S. Alioli, P. Nason, C. Oleari, and E. Re, *A general framework for implementing NLO calculations in shower Monte Carlo programs: the POWHEG BOX*, JHEP **06**

(2010) 043, `arXiv:1002.2581 [hep-ph]`.

[90] T. Sjöstrand, S. Mrenna, and P. Z. Skands, *PYTHIA 6.4 Physics and Manual*, JHEP **05** (2006) 026, `arXiv:hep-ph/0603175`.

[91] T. Sjöstrand, S. Mrenna, and P. Z. Skands, *A Brief Introduction to PYTHIA 8.1*, Comput. Phys. Commun. **178** (2008) 852, `arXiv:0710.3820 [hep-ph]`.

[92] T. Sjöstrand et al., *An Introduction to PYTHIA 8.2*, Comput. Phys. Commun. **191** (2015) 159–177, `arXiv:1410.3012 [hep-ph]`.

[93] G. Corcella, I. G. Knowles, G. Marchesini, S. Moretti, K. Odagiri, P. Richardson, M. H. Seymour, and B. R. Webber, *HERWIG 6: An Event generator for hadron emission reactions with interfering gluons (including supersymmetric processes)*, JHEP **01** (2001) 010, `arXiv:hep-ph/0011363 [hep-ph]`.

[94] F. Kahlhoefer, *Review of LHC Dark Matter Searches*, Int. J. Mod. Phys. **A32** (2017) 1730006, `arXiv:1702.02430 [hep-ph]`.

[95] ATLAS Collaboration, *Search for new phenomena in final states with an energetic jet and large missing transverse momentum in pp collisions at $\sqrt{s} = 13$ TeV using the ATLAS detector*, Phys. Rev. **D94** (2016) no. 3, 032005, `arXiv:1604.07773 [hep-ex]`.

[96] CMS Collaboration, *Search for dark matter produced with an energetic jet or a hadronically decaying W or Z boson at $\sqrt{s} = 13$ TeV*, `arXiv:1703.01651 [hep-ex]`.

[97] ATLAS Collaboration, *Search for new phenomena in events with a photon and missing transverse momentum in pp collisions at $\sqrt{s} = 13$ TeV with the ATLAS detector*, JHEP **06** (2016) 059, `arXiv:1604.01306 [hep-ex]`.

[98] CMS Collaboration, *Search for dark matter and graviton produced in association with a photon in pp collisions at $\sqrt{s} = 13$ TeV with an integrated luminosity of $12.9$ fb$^{-1}$*, Tech. Rep. CMS-PAS-EXO-16-039, CERN, Geneva, 2016. `https://cds.cern.ch/record/2205148`.

[99] ATLAS Collaboration, *Search for new phenomena in the $Z(\to \ell\ell) + E_{\mathrm{T}}^{\mathrm{miss}}$ final state at $\sqrt{s} = 13$ TeV with the ATLAS detector*, Tech. Rep. ATLAS-CONF-2016-056, CERN, Geneva, Aug, 2016. `http://cds.cern.ch/record/2206138`.

[100] CMS Collaboration, *Search for dark matter and unparticles in events with a Z boson and missing transverse momentum in proton-proton collisions at $\sqrt{s} = 13$ TeV*, JHEP **03** (2017) 061, `arXiv:1701.02042 [hep-ex]`.

[101] ATLAS Collaboration, *Search for dark matter produced in association with a hadronically decaying vector boson in pp collisions at $\sqrt{s}$ = 13 TeV with the ATLAS detector*, Phys. Lett. **B763** (2016) 251–268, `arXiv:1608.02372 [hep-ex]`.

[102] ATLAS Collaboration, *Search for new particles in events with one lepton and missing transverse momentum in pp collisions at $\sqrt{s}$ = 8 TeV with the ATLAS detector*, JHEP **09** (2014) 037, `arXiv:1407.7494 [hep-ex]`.

[103] CMS Collaboration, *Search for physics beyond the standard model in final states with a lepton and missing transverse energy in proton-proton collisions at sqrt(s) = 8 TeV*, Phys. Rev. **D91** (2015) no. 9, 092005, `arXiv:1408.2745 [hep-ex]`.

[104] ATLAS Collaboration, *Search for Dark Matter in Events with Missing Transverse Momentum and a Higgs Boson Decaying to Two Photons in pp Collisions at $\sqrt{s} = 8$ TeV with the ATLAS Detector*, Phys. Rev. Lett. **115** (2015) no. 13, 131801, `arXiv:1506.01081 [hep-ex]`.

[105] ATLAS Collaboration, *Search for dark matter in association with a Higgs boson decaying to b-quarks in pp collisions at $\sqrt{s} = 13$ TeV with the ATLAS detector*, Phys. Lett. **B765** (2017) 11–31, `arXiv:1609.04572 [hep-ex]`.

[106] CMS Collaboration, *Search for associated production of dark matter with a Higgs boson decaying to $b\bar{b}$ or $\gamma\gamma$ at $\sqrt{s}$ = 13 TeV*, `arXiv:1703.05236 [hep-ex]`.

[107] ATLAS Collaboration, *Search for dark matter in events with heavy quarks and missing transverse momentum in pp collisions with the ATLAS detector*, Eur. Phys. J. **C75** (2015) no. 2, 92, `arXiv:1410.4031 [hep-ex]`.

[108] CMS Collaboration, *Search for dark matter in association with a top quark pair at $\sqrt{s}$=13 TeV*, Tech. Rep. CMS-PAS-EXO-16-005, CERN, Geneva, 2016. `https://cds.cern.ch/record/2204933`.

[109] ATLAS Collaboration, *Search for invisible particles produced in association with single-top-quarks in proton-proton collisions at $\sqrt{s}$ = 8 TeV with the ATLAS detector*, Eur. Phys. J. **C75** (2015) no. 2, 79, `arXiv:1410.5404 [hep-ex]`.

[110] ATLAS Collaboration, *Constraints on new phenomena via Higgs boson couplings and invisible decays with the ATLAS detector*, JHEP **11** (2015) 206, `arXiv:1509.00672 [hep-ex]`.

[111] CMS Collaboration, *Searches for invisible decays of the Higgs boson in pp collisions at $\sqrt{s}$ = 7, 8, and 13 TeV*, JHEP **02** (2017) 135, `arXiv:1610.09218 [hep-ex]`.

[112] ATLAS Collaboration, *Search for new phenomena in dijet mass and angular*

*distributions from pp collisions at* $\sqrt{s} = 13$ *TeV with the ATLAS detector*, Phys. Lett. **B754** (2016) 302–322, `arXiv:1512.01530 [hep-ex]`.

[113] ATLAS Collaboration, *Search for new light resonances decaying to jet pairs and produced in association with a photon in proton-proton collisions at* $\sqrt{s} = 13$ *TeV with the ATLAS detector*, Tech. Rep. ATLAS-CONF-2016-029, CERN, Geneva, Jun, 2016. `http://cds.cern.ch/record/2161134`.

[114] ATLAS Collaboration, *Search for light dijet resonances with the ATLAS detector using a Trigger-Level Analysis in LHC pp collisions at* $\sqrt{s} = 13$ *TeV*, Tech. Rep. ATLAS-CONF-2016-030, CERN, Geneva, Jun, 2016. `http://cds.cern.ch/record/2161135`.

[115] CMS Collaboration, *Search for dijet resonances in proton-proton collisions at* $\sqrt{s} = 13$ *TeV and constraints on dark matter and other models*, Phys. Lett. B (2016) , `arXiv:1611.03568 [hep-ex]`.

[116] CMS Collaboration, *The CMS Experiment at the CERN LHC*, JINST **3** (2008) S08004.

[117] *Summary plots from the ATLAS Exotic physics group*, `https://atlas.web.cern.ch/Atlas/GROUPS/PHYSICS/CombinedSummaryPlots/EXOTICS/index.html`. [Accessed 4 September 2017].

[118] *Summary plots from the CMS Exotic physics group*, `https://twiki.cern.ch/twiki/bin/view/CMSPublic/PhysicsResultsEXO`. [Accessed 4 September 2017].

[119] LHCb Collaboration, *The LHCb Detector at the LHC*, JINST **3** (2008) S08005.

[120] ALICE Collaboration, *The ALICE experiment at the CERN LHC*, JINST **3** (2008) S08002.

[121] C. De Melis, *The CERN accelerator complex*, . `https://cds.cern.ch/record/2197559`.

[122] ATLAS Collaboration, *Improved luminosity determination in pp collisions at sqrt(s) = 7 TeV using the ATLAS detector at the LHC*, Eur. Phys. J. **C73** (2013) no. 8, 2518, `arXiv:1302.4393 [hep-ex]`.

[123] ATLAS Collaboration, *Luminosity determination in pp collisions at* $\sqrt{s} = 8$ *TeV using the ATLAS detector at the LHC*, Eur. Phys. J. **C76** (2016) no. 12, 653, `arXiv:1608.03953 [hep-ex]`.

[124] *ATLAS Luminosity summary plots for 2015 pp data taking*, `https:`
`//twiki.cern.ch/twiki/bin/view/AtlasPublic/LuminosityPublicResultsRun2`.
[Accessed 4 September 2017].

[125] ATLAS Collaboration, *ATLAS Insertable B-Layer Technical Design Report*,
Atlas-tdr-19, 2010. `http://cds.cern.ch/record/1291633`.

[126] ATLAS Collaboration, *IBL Efficiency and Single Point Resolution in Collision
Events*, Tech. Rep. ATL-INDET-PUB-2016-001, CERN, Geneva, Aug, 2016.
`https://cds.cern.ch/record/2203893`.

[127] J. Pequenao, *Event Cross Section in a computer generated image of the ATLAS
detector.*, Mar, 2008.

[128] ATLAS Collaboration, *Performance of the ATLAS Trigger System in 2015*, Eur.
Phys. J. **C77** (2017) no. 5, 317, `arXiv:1611.09661 [hep-ex]`.

[129] T. Cornelissen, M. Elsing, S. Fleischmann, W. Liebig, E. Moyse, and A. Salzburger,
*Concepts, Design and Implementation of the ATLAS New Tracking (NEWT)*, Tech.
Rep. ATL-SOFT-PUB-2007-007. ATL-COM-SOFT-2007-002, CERN, Geneva, Mar,
2007. `https://cds.cern.ch/record/1020106`.

[130] ATLAS Collaboration, *Performance of the ATLAS Inner Detector Track and Vertex
Reconstruction in the High Pile-Up LHC Environment*, Tech. Rep.
ATLAS-CONF-2012-042, CERN, Geneva, Mar, 2012.
`http://cds.cern.ch/record/1435196`.

[131] ATLAS Collaboration, *Track Reconstruction Performance of the ATLAS Inner
Detector at $\sqrt{s} = 13$ TeV*, Tech. Rep. ATL-PHYS-PUB-2015-018, CERN, Geneva,
Jul, 2015. `https://cds.cern.ch/record/2037683`.

[132] ATLAS Collaboration, *Topological cell clustering in the ATLAS calorimeters and its
performance in LHC Run 1*, `arXiv:1603.02934 [hep-ex]`.

[133] M. Aharrouche et al., *Measurement of the response of the ATLAS liquid argon barrel
calorimeter to electrons at the 2004 combined test-beam*, Nucl. Instrum. Meth. **A614**
(2010) 400–432.

[134] M. Aharrouche et al., *Response uniformity of the ATLAS liquid argon
electromagnetic calorimeter*, Nuclear Instruments and Methods in Physics Research
A **582** (Nov., 2007) 429–455, `arXiv:0709.1094 [physics.ins-det]`.

[135] M. Aharrouche et al., *Energy linearity and resolution of the ATLAS electromagnetic
barrel calorimeter in an electron test-beam*, Nuclear Instruments and Methods in

Physics Research A **568** (Dec., 2006) 601–623, `arXiv:physics/0608012`.

[136] C. Issever, K. Borras, and D. Wegener, *An improved weighting algorithm to achieve software compensation in a fine grained LAr calorimeter*, Nuclear Instruments and Methods in Physics Research A **545** (June, 2005) 803–812, `arXiv:physics/0408129`.

[137] ATLAS Collaboration, *Monte Carlo Calibration and Combination of In-situ Measurements of Jet Energy Scale, Jet Energy Resolution and Jet Mass in ATLAS*, Tech. Rep. ATLAS-CONF-2015-037, CERN, Geneva, Aug, 2015. `https://cds.cern.ch/record/2044941`.

[138] M. Cacciari and G. P. Salam, *Pileup subtraction using jet areas*, Physics Letters B **659** (2008) no. 12, 119 – 126.

[139] ATLAS Collaboration, *Pile-up subtraction and suppression for jets in ATLAS*, Tech. Rep. ATLAS-CONF-2013-083, CERN, Geneva, Aug, 2013. `https://cds.cern.ch/record/1570994`.

[140] ATLAS Collaboration, *Jet energy measurement with the ATLAS detector in proton-proton collisions at $\sqrt{s} = 7\ TeV$*, Eur. Phys. J. **C73** (2013) no. 3, 2304, `arXiv:1112.6426 [hep-ex]`.

[141] ATLAS Collaboration, *Jet global sequential corrections with the ATLAS detector in proton-proton collisions at sqrt(s) = 8 TeV*, Tech. Rep. ATLAS-CONF-2015-002, CERN, Geneva, Mar, 2015. `https://cds.cern.ch/record/2001682`.

[142] ATLAS Collaboration, *Data-driven determination of the energy scale and resolution of jets reconstructed in the ATLAS calorimeters using dijet and multijet events at $\sqrt{s} = 8\ TeV$*, Tech. Rep. ATLAS-CONF-2015-017, CERN, Geneva, Apr, 2015. `https://cds.cern.ch/record/2008678`.

[143] ATLAS Collaboration, *Jet energy scale measurements and their systematic uncertainties in proton-proton collisions at $\sqrt{s} = 13\ TeV$ with the ATLAS detector*, `arXiv:1703.09665 [hep-ex]`.

[144] ATLAS Collaboration, *Selection of jets produced in 13TeV proton-proton collisions with the ATLAS detector*, Tech. Rep. ATLAS-CONF-2015-029, CERN, Geneva, Jul, 2015. `https://cds.cern.ch/record/2037702`.

[145] ATLAS Collaboration, *Tagging and suppression of pileup jets with the ATLAS detector*, Tech. Rep. ATLAS-CONF-2014-018, CERN, Geneva, May, 2014. `https://cds.cern.ch/record/1700870`.

[146] W. Lampl et al., *Calorimeter clustering algorithms: Description and performance*, .

`http://cds.cern.ch/record/1099735`.

[147] ATLAS Collaboration, *Electron and photon energy calibration with the ATLAS detector using data collected in 2015 at $\sqrt{s}$ =13 TeV*, Tech. Rep. ATL-PHYS-PUB-2016-015, CERN, Geneva, Aug, 2016. `http://cds.cern.ch/record/2203514`.

[148] ATLAS Collaboration, *Electron efficiency measurements with the ATLAS detector using the 2015 LHC proton-proton collision data*, Tech. Rep. ATLAS-CONF-2016-024, CERN, Geneva, Jun, 2016. `https://cds.cern.ch/record/2157687`.

[149] ATLAS Collaboration Collaboration, *Photon identification in 2015 ATLAS data*, Tech. Rep. ATL-PHYS-PUB-2016-014, CERN, Geneva, Aug, 2016. `http://cds.cern.ch/record/2203125`.

[150] ATLAS Collaboration, *Reconstruction, Energy Calibration, and Identification of Hadronically Decaying Tau Leptons in the ATLAS Experiment for Run-2 of the LHC*, Tech. Rep. ATL-PHYS-PUB-2015-045, CERN, Geneva, Nov, 2015. `https://cds.cern.ch/record/2064383`.

[151] ATLAS Collaboration, *Muon reconstruction performance of the ATLAS detector in protonproton collision data at $\sqrt{s}$ =13 TeV*, Eur. Phys. J. **C76** (2016) no. 5, 292, `arXiv:1603.05598 [hep-ex]`.

[152] ATLAS Collaboration, *Performance of missing transverse momentum reconstruction for the ATLAS detector in the first proton-proton collisions at at $\sqrt{s}$= 13 TeV*, Tech. Rep. ATL-PHYS-PUB-2015-027, CERN, Geneva, Jul, 2015. `https://cds.cern.ch/record/2037904`.

[153] ATLAS Collaboration, *Measurement of the inclusive jet cross section in pp collisions at sqrt(s)=2.76 TeV and comparison to the inclusive jet cross section at sqrt(s)=7 TeV using the ATLAS detector*, Eur. Phys. J. **C73** (2013) no. 8, 2509, `arXiv:1304.4739 [hep-ex]`.

[154] ATLAS Collaboration, *Measurement of dijet cross sections in pp collisions at 7 TeV centre-of-mass energy using the ATLAS detector*, JHEP **05** (2014) 059, `arXiv:1312.3524 [hep-ex]`.

[155] ATLAS Collaboration, *Measurement of four-jet differential cross sections in $\sqrt{s} = 8$ TeV proton-proton collisions using the ATLAS detector*, JHEP **12** (2015) 105, `arXiv:1509.07335 [hep-ex]`.

[156] ATLAS Collaboration, *A search for pair produced resonances in four jets final states in proton-proton collisions at $\sqrt{s}$=13 TeV with the ATLAS experiment*, Tech. Rep. ATLAS-CONF-2016-084, CERN, Geneva, Aug, 2016. `https://cds.cern.ch/record/2206277`.

[157] ATLAS Collaboration, *Search for new phenomena in final states with large jet multiplicities and missing transverse momentum with ATLAS using proton-proton collisions*, Physics Letters B **757** (2016) 334 – 355.

[158] R. Achenbach et al., *The ATLAS Level-1 Calorimeter Trigger*, Journal of Instrumentation **3** (2008) no. 03, P03001. `http://stacks.iop.org/1748-0221/3/i=03/a=P03001`.

[159] ATLAS Collaboration, *The performance of the jet trigger for the ATLAS detector during 2011 data taking*, Eur. Phys. J. **C76** (2016) no. 10, 526, `arXiv:1606.07759 [hep-ex]`.

[160] P. Calafiura et al., *The StoreGate: A Data model for the Atlas software architecture*, eConf **C0303241** (2003) MOJT008, `arXiv:cs/0306089 [cs-se]`.

[161] M. Cacciari, G. P. Salam, and G. Soyez, *FastJet User Manual*, Eur. Phys. J. C **72** (2012) 1896, `arXiv:1111.6097 [hep-ph]`.

[162] B. Nachman et al., *Jets from Jets: Re-clustering as a tool for large radius jet reconstruction and grooming at the LHC*, JHEP **02** (2015) 075, `arXiv:1407.2922 [hep-ph]`.

[163] ATLAS Collaboration, A. Tavares Delgado, *Design and performance of the ATLAS jet trigger system*, Tech. Rep. ATL-DAQ-PROC-2015-019, CERN, Geneva, May, 2015. `https://cds.cern.ch/record/2018453`.

[164] ATLAS Collaboration, *The ATLAS Jet Trigger for Initial LHC Run II*, Tech. Rep. ATL-DAQ-INT-2015-001, CERN, Geneva, Dec, 2015. `https://cds.cern.ch/record/2116336`.

[165] ATLAS Collaboration, *Readiness of the ATLAS Liquid Argon Calorimeter for LHC Collisions*, Eur.Phys.J. **C70** (2010) 723–753, `arXiv:0912.2642 [physics.ins-det]`.

[166] B. Simmons, P. Sherwood, K. Ciba, and A. Richards, *The ATLAS RunTimeTester software*, Journal of Physics: Conference Series **219** (2010) no. 4, 042023. `http://stacks.iop.org/1742-6596/219/i=4/a=042023`.

[167] M. Hodgkinson, R. Seuster, B. Simmons, D. Rousseau, and P. Sherwood, *Software*

*Validation in ATLAS*, Journal of Physics: Conference Series **396** (2012) no. 5, 052040. `http://stacks.iop.org/1742-6596/396/i=5/a=052040`.

[168] *ATLAS RTT results pages*, `https://atlas-rtt.cern.ch`. [Accessed 4 September 2017].

[169] ATLAS Collaboration, *ATLAS Run 1 Pythia8 tunes*, Tech. Rep. ATL-PHYS-PUB-2014-021, CERN, Geneva, Nov, 2014. `https://cds.cern.ch/record/1966419`.

[170] GEANT4 Collaboration, S. Agostinelli et al., *GEANT4: A simulation toolkit*, Nucl. Instrum. Meth. A **506** (2003) 250.

[171] J. Allison et al., *Geant4 developments and applications*, IEEE Trans. Nucl. Sci. **53** (2006) 270.

[172] ATLAS Collaboration, *The ATLAS Simulation Infrastructure*, Eur. Phys. J. **C70** (2010) 823–874, `arXiv:1005.4568 [physics.ins-det]`.

[173] ATLAS Collaboration, *Summary of ATLAS Pythia 8 tunes*, Tech. Rep. ATL-PHYS-PUB-2012-003, CERN, Geneva, Aug, 2012. `https://cds.cern.ch/record/1474107`.

[174] A. D. Martin, W. J. Stirling, R. S. Thorne, and G. Watt, *Parton distributions for the LHC*, Eur. Phys. J. **C63** (2009) 189–285, `arXiv:0901.0002 [hep-ph]`.

[175] ATLAS Collaboration, *Measurement of detector-corrected observables sensitive to the anomalous production of events with jets and large missing transverse momentum in pp collisions at $\sqrt{s} = 13$ TeV using the ATLAS detector*, Eur. Phys. J. **C77** (2017) no. 11, 765, `arXiv:1707.03263 [hep-ex]`.

[176] ATLAS Collaboration, *Monte Carlo Generators for the Production of a W or $Z/\gamma^*$ Boson in Association with Jets at ATLAS in Run 2*, Tech. Rep. ATL-PHYS-PUB-2016-003, CERN, Geneva, Jan, 2016. `https://cds.cern.ch/record/2120133`.

[177] T. Gleisberg and S. Höche, *Comix, a new matrix element generator*, JHEP **0812** (2008) 039, `arXiv:0808.3674 [hep-ph]`.

[178] F. Cascioli, P. Maierhofer, and S. Pozzorini, *Scattering Amplitudes with Open Loops*, Phys. Rev. Lett. **108** (2012) 111601, `arXiv:1111.5206 [hep-ph]`.

[179] S. Höche, F. Krauss, M. Schönherr, and F. Siegert, *QCD matrix elements + parton showers: The NLO case*, JHEP **04** (2013) 027, `arXiv:1207.5030 [hep-ph]`.

[180] NNPDF Collaboration, R. D. Ball et al., *Parton distributions for the LHC Run II*, JHEP **04** (2015) 040, `arXiv:1410.8849 [hep-ph]`.

[181] C. Anastasiou, L. J. Dixon, K. Melnikov, and F. Petriello, *High precision QCD at hadron colliders: Electroweak gauge boson rapidity distributions at NNLO*, Phys. Rev. **D69** (2004) 094008, `arXiv:hep-ph/0312266 [hep-ph]`.

[182] ATLAS Collaboration, *Multi-Boson Simulation for 13 TeV ATLAS Analyses*, Tech. Rep. ATL-PHYS-PUB-2016-002, CERN, Geneva, Jan, 2016. `https://cds.cern.ch/record/2119986`.

[183] Particle Data Group Collaboration, *Review of Particle Physics*, Chin. Phys. **C38** (2014) 090001.

[184] S. Alioli, S.-O. Moch, and P. Uwer, *Hadronic top-quark pair-production with one jet and parton showering*, JHEP **01** (2012) 137, `arXiv:1110.5251 [hep-ph]`.

[185] E. Re, *Single-top Wt-channel production matched with parton showers using the POWHEG method*, Eur. Phys. J. **C71** (2011) 1547, `arXiv:1009.2450 [hep-ph]`.

[186] S. Alioli, P. Nason, C. Oleari, and E. Re, *NLO single-top production matched with shower in POWHEG: s- and t-channel contributions*, JHEP **09** (2009) 111, `arXiv:0907.4076 [hep-ph]`. [Erratum: JHEP02,011(2010)].

[187] R. Frederix, E. Re, and P. Torrielli, *Single-top t-channel hadroproduction in the four-flavour scheme with POWHEG and aMC@NLO*, JHEP **09** (2012) 130, `arXiv:1207.5391 [hep-ph]`.

[188] ATLAS Collaboration, *Simulation of top quark production for the ATLAS experiment at sqrt(s) = 13 TeV*, Tech. Rep. ATL-PHYS-PUB-2016-004, CERN, Geneva, Jan, 2016. `https://cds.cern.ch/record/2120417`.

[189] P. Artoisenet, R. Frederix, O. Mattelaer, and R. Rietkerk, *Automatic spin-entangled decays of heavy resonances in Monte Carlo simulations*, JHEP **1303** (2013) 015, `arXiv:1212.3460 [hep-ph]`.

[190] J. Pumplin, D. R. Stump, J. Huston, H. L. Lai, P. M. Nadolsky, and W. K. Tung, *New generation of parton distributions with uncertainties from global QCD analysis*, JHEP **07** (2002) 012, `arXiv:hep-ph/0201195 [hep-ph]`.

[191] P. Z. Skands, *Tuning Monte Carlo Generators: The Perugia Tunes*, Phys. Rev. **D82** (2010) 074018, `arXiv:1005.3457 [hep-ph]`.

[192] M. Czakon and A. Mitov, *Top++: A Program for the Calculation of the Top-Pair*

*Cross-Section at Hadron Colliders*, Comput. Phys. Commun. **185** (2014) 2930, `arXiv:1112.5675 [hep-ph]`.

[193] N. Kidonakis, *Two-loop soft anomalous dimensions for single top quark associated production with a W- or H-*, Phys. Rev. **D82** (2010) 054018, `arXiv:1005.4451 [hep-ph]`.

[194] N. Kidonakis, *NNLL resummation for s-channel single top quark production*, Phys. Rev. D **81** (2010) 054028, `arXiv:1001.5034 [hep-ph]`.

[195] N. Kidonakis, *Next-to-next-to-leading-order collinear and soft gluon corrections for t-channel single top quark production*, Phys. Rev. D **83** (2011) 091503, `arXiv:1103.2792 [hep-ph]`.

[196] D. J. Lange, *The EvtGen particle decay simulation package*, Nucl. Instrum. Meth. **A462** (2001) 152.

[197] U. Haisch, F. Kahlhoefer, and E. Re, *QCD effects in mono-jet searches for dark matter*, JHEP **12** (2013) 007, `arXiv:1310.4491 [hep-ph]`.

[198] S. Alioli, P. Nason, C. Oleari, and E. Re, *NLO Higgs boson production via gluon fusion matched with shower in POWHEG*, JHEP **04** (2009) 002, `arXiv:0812.0578 [hep-ph]`.

[199] P. Nason and C. Oleari, *NLO Higgs boson production via vector-boson fusion matched with shower in POWHEG*, JHEP **02** (2010) 037, `arXiv:0911.5299 [hep-ph]`.

[200] E. Bagnaschi, G. Degrassi, P. Slavich, and A. Vicini, *Higgs production via gluon fusion in the POWHEG approach in the SM and in the MSSM*, JHEP **02** (2012) 088, `arXiv:1111.2854 [hep-ph]`.

[201] LHC Higgs Cross Section Working Group Collaboration, J. R. Andersen et al., *Handbook of LHC Higgs Cross Sections: 3. Higgs Properties*, `arXiv:1307.1347 [hep-ph]`.

[202] ATLAS Collaboration, *Proposal for truth particle observable definitions in physics measurements*, Tech. Rep. ATL-PHYS-PUB-2015-013, CERN, Geneva, Jun, 2015. `https://cds.cern.ch/record/2022743`.

[203] ATLAS Collaboration, *Recommendations of the Physics Objects and Analysis Harmonisation Study Groups 2014*, Tech. Rep. ATL-COM-PHYS-2014-451, CERN, Geneva, May, 2014. `https://cds.cern.ch/record/1700874`.

[204] ATLAS Collaboration, *Search for squarks and gluinos with the ATLAS detector in*

*final states with jets and missing transverse momentum using 4.7 fb$^{-1}$ of $\sqrt{s} = 7$ TeV proton-proton collision data*, Phys. Rev. **D87** (2013) no. 1, 012008, `arXiv:1208.0949 [hep-ex]`.

[205] K. G. Hayes, M. L. Perl, and B. Efron, *Application of the Bootstrap Statistical Method to the Tau Decay Mode Problem*, Phys. Rev. **D39** (1989) 274.

[206] ATLAS Collaboration, *Measurement of the inclusive isolated prompt photon cross section in pp collisions at $\sqrt{s} = 7$ TeV with the ATLAS detector*, Phys. Rev. **D83** (2011) 052005, `arXiv:1012.4389 [hep-ex]`.

[207] ATLAS Collaboration, *Measurement of the Production Cross Sections of a Z Boson in Association with Jets in pp collisions at $\sqrt{s} = 13$ TeV with the ATLAS Detector*, Tech. Rep. ATLAS-CONF-2015-041, CERN, Geneva, Aug, 2015. `https://cds.cern.ch/record/2048104`.

[208] ATLAS Collaboration, *Expected performance of the ATLAS b-tagging algorithms in Run-2*, Tech. Rep. ATL-PHYS-PUB-2015-022, CERN, Geneva, Jul, 2015. `https://cds.cern.ch/record/2037697`.

[209] L. A. Harland-Lang, A. D. Martin, P. Motylinski, and R. S. Thorne, *Parton distributions in the LHC era: MMHT 2014 PDFs*, Eur. Phys. J. **C75** (2015) no. 5, 204, `arXiv:1412.3989 [hep-ph]`.

[210] S. Dulat et al., *New parton distribution functions from a global analysis of quantum chromodynamics*, Phys. Rev. **D93** (2016) no. 3, 033006, `arXiv:1506.07443 [hep-ph]`.

[211] J. Butterworth et al., *PDF4LHC recommendations for LHC Run II*, J. Phys. **G43** (2016) 023001, `arXiv:1510.03865 [hep-ph]`.

[212] R. Nisius, *On the combination of correlated estimates of a physics observable*, Eur. Phys. J. **C74** (2014) no. 8, 3004, `arXiv:1402.4016 [physics.data-an]`.

[213] A. L. Read, *Presentation of search results: The CL(s) technique*, J. Phys. **G28** (2002) 2693–2704. [,11(2002)].

[214] T. Junk, *Confidence level computation for combining searches with small statistics*, Nucl. Instrum. Meth. **A434** (1999) 435–443, `arXiv:hep-ex/9902006 [hep-ex]`.

[215] G. Cowan, K. Cranmer, E. Gross, and O. Vitells, *Asymptotic formulae for likelihood-based tests of new physics*, Eur. Phys. J. **C71** (2011) 1554, `arXiv:1007.1727 [physics.data-an]`. [Erratum: Eur. Phys. J.C73,2501(2013)].

[216] Fermi-LAT Collaboration, *Constraining Dark Matter Models from a Combined Analysis of Milky Way Satellites with the Fermi Large Area Telescope*, Phys. Rev. Lett. **107** (2011) 241302, `arXiv:1108.3546 [astro-ph.HE]`.

[217] VERITAS Collaboration, *VERITAS Deep Observations of the Dwarf Spheroidal Galaxy Segue 1*, Phys. Rev. **D85** (2012) 062001, `arXiv:1202.2144 [astro-ph.HE]`. [Erratum: Phys. Rev.D91,no.12,129903(2015)].

[218] Planck Collaboration, *Planck 2015 results. I. Overview of products and scientific results*, Astron. Astrophys. **594** (2016) A1, `arXiv:1502.01582 [astro-ph.CO]`.

[219] WMAP Collaboration, *Nine-Year Wilkinson Microwave Anisotropy Probe (WMAP) Observations: Cosmological Parameter Results*, Astrophys. J. Suppl. **208** (2013) 19, `arXiv:1212.5226 [astro-ph.CO]`.

[220] LHC Higgs Cross Section Working Group Collaboration, *Handbook of LHC Higgs Cross Sections: 4. Deciphering the Nature of the Higgs Sector*, `arXiv:1610.07922 [hep-ph]`.

[221] ATLAS Collaboration, *Search for invisible decays of a Higgs boson using vector-boson fusion in pp collisions at $\sqrt{s} = 8$ TeV with the ATLAS detector*, JHEP **01** (2016) 172, `arXiv:1508.07869 [hep-ex]`.

[222] A. Buckley and M. Whalley, *HepData reloaded: Reinventing the HEP data archive*, PoS **ACAT2010** (2010) 067, `arXiv:1006.0517 [hep-ex]`.

[223] A. Buckley et al., *Rivet user manual*, Comput. Phys. Commun. **184** (2013) 2803–2819, `arXiv:1003.0694 [hep-ph]`.

[224] J. M. Butterworth et al., *Constraining new physics with collider measurements of Standard Model signatures*, JHEP **03** (2017) 078, `arXiv:1606.05296 [hep-ph]`.